The Role of Ensembles in Metal Phosphide Electrocatalysis for Modulating Nitrate Electroreduction Behavior

Emily Nishiwaki

A dissertation
submitted in partial fulfillment of the
requirements for the degree of

Doctor of Philosophy

University of Washington

2025

Reading Committee:

Brandi Cossairt, Chair

Bo Zhang

Alexandra Velian

David Beck

Program Authorized to Offer Degree:
Chemistry

University of Washington

Abstract

The Role of Ensembles in Metal Phosphide
Electrocatalysis for Modulating
Nitrate Electroreduction Behavior

Emily Nishiwaki

Chair of the Supervisory Committee:
Brandi Cossairt
Chemistry

Transition metal phosphides (TMPs) are an exciting class of electrocatalytic materials due to their active site ensembles, i.e., the surface charge distribution and variety of adsorption sites. While the importance of surface ensembles has been thoroughly investigated for HER and CO_2 electroreduction, the mechanism and performance of Ni_2P for the electroreduction of NO_3^- to NH_3 remains understudied. In this work, we prepared 5 nm Ni_2P nanocrystals using a heat-up colloidal synthesis and demonstrate a 100% Faradaic efficiency for NO_3^- reduction over HER at -0.4 V vs. RHE in neutral, buffered conditions. NH_3 selectivity is maximized ($> 80\%$ FE) at -0.2 V vs. RHE, where phosphate is the hydrogen source for the hydrogenation of NO_x* intermediates. Our rate order analysis and DFT calculations support a sequential deoxygenation-hydrogenation pathway of NO_3^- to NH_3 that involves competitive co-adsorption of H* and NO_x* intermediates. Encouraged by the positive impact of active site ensembles on Ni_2P nanocrystals for NO_3^- electroreduction behavior, we explored methods to modify the ensembles via nanocrystal doping. To that end, we prepared a series of $Ni_{2-x}M_xP$ nanocrystals (M = Cu, Co) using a two step, post-synthetic cation exchange method and evaluated them as NO_3^- electroreduction catalysts. We observed that cobalt-doped Ni_2P nanocrystals are able to suppress HER to less than 10% Faradaic Efficiency in favor of NH_3 production ($> 80\%$ FE). In contrast, copper-doped Ni_2P nanocrystals favor HER and NO_2^-; H_2 Faradaic efficiency increases from 0 to 60% and correspondingly, NH_3 selectivity decreases by 60% at -0.4 V vs. RHE. We rationalize the selectivity trends based on the relative H-binding

strengths of these dopants, where copper introduces more weakly-bound hydrogens on the surface and inhibits NH_3 formation. Conversely, cobalt introduces strongly-bound hydrogens on the surface that enables hydrogenation of reaction intermediates to form NH_3. These works demonstrate the importance of active site ensembles in the development of earth-abundant, selective catalysts for NO_3^- electroreduction to NH_3 and beyond with other electrosynthetic reactions.

TABLE OF CONTENTS

LIST OF FIGURES

LIST OF TABLES

ACKNOWLEDGMENTS

First, I would like to thank my advisor, Brandi Cossairt for her guidance and mentorship during my graduate studies.

I would also like to thank the Cossairt Lab members who have made my PhD more than just a degree, but also a journey with amazing friends that I will look back on and cherish.

Additionally, I would like to thank the members of the Suntivich Lab, who were there during my formative years as a scientist and have shaped me into the researcher I am today.

Lastly, I thank my family, particularly my parents and sister, and my incredible friends, near and far, for their unwavering support.

Chapter 1

INTRODUCTION TO METAL PHOSPHIDE ELECTROCATALYSIS

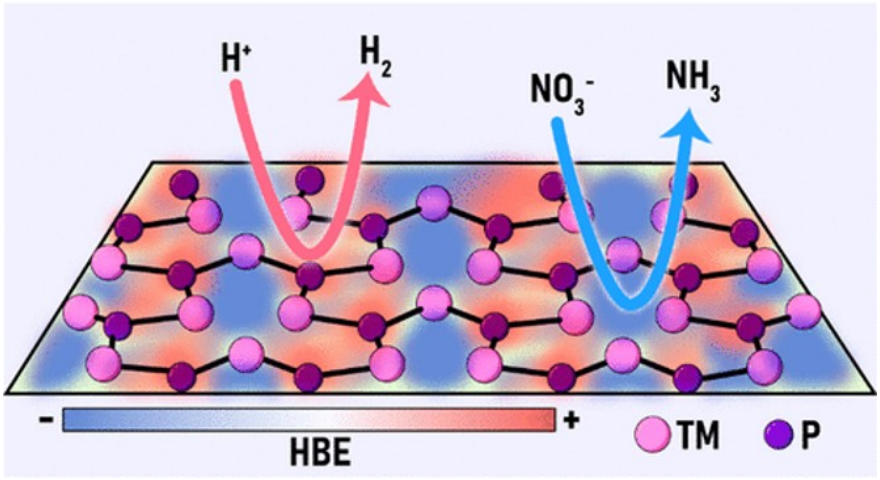

Figure 1.1: A transition metal phosphide surface, which has distribution of e^- density and affinity for hydrogen, can be leveraged to control reaction selectivity.

Portions of this chapter are adapted with permission from: Kuo, D.-Y., Nishiwaki, E., Cossairt, B. M., et al. ACS Catalysis, **2023**, 13, 1, 287-295. [2]

1.1 What is Electrocatalysis?

Electrocatalysis is the use of electricity to make and break chemical bonds (Fig. 1.2). It is the foundation of renewable clean energy conversion and storage technologies, such as fuel cells and batteries, that are being development as alternatives to fossil fuel combustion. In these devices, chemical energy stored in the bonds of molecules (e.g, H_2, H_2O, and O_2) is converted to electrical energy (or vice versa), via oxidation and reduction reactions. [3]

Electrocatalytic chemical transformations can also be utilized to synthesize commodity chemicals. This idea is not new; the idea of electrosynthesis of ammonia dates back to the 1980s. [4]

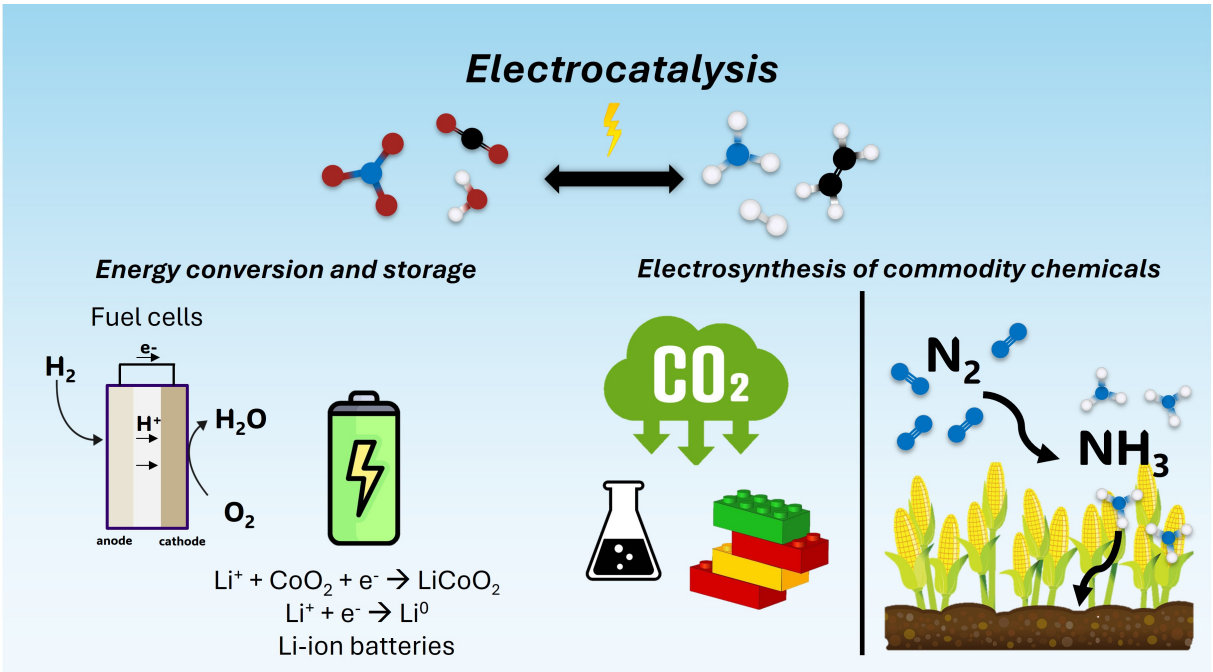

Figure 1.2: An overview of a few key applications of electrocatalysis.

Traditionally, commodity chemicals (e.g. ethylene, methanol, ammonia) are synthesized with high temperatures or pressures via heterogeneous catalysis. [5] However, with the chemical industry accounting for ∼30% of industrial energy consumption, depleting finite natural resources to generate heat, and ultimately contributing to ∼20% of global greenhouse gas emissions, it is becoming more critical than ever to find alternative methods of chemical production. [6] In contrast to thermal catalysis, electrocatalysis uses electricity, rather than heat, to tune the potential of the catalyst surface to selectively synthesize compounds under mild reaction conditions, which mitigates the emission of large amounts of CO_2 and makes it a cleaner alternative for chemical synthesis. [7, 8]

1.2 Introduction to a heterogeneous catalyst

Endergonic electrochemical transformations generally require catalysts to facilitate more facile reaction kinetics. Heterogeneous electrocatalysts are solid materials that adsorb various reaction intermediates onto active sites, which can react with each other to form the final chemical product.

The activity of these sites, or the thermodynamics of the surface, can be influenced by the tuning of chemical composition, the geometry of the catalyst, and more. [3,9] Effectively designing a selective catalyst surface for a certain reaction is a difficult art of tailoring a surface's coverage of reaction intermediates. Paul Sabatier and Linus Pauling's seminal works from more than 70 years ago still govern modern-day ideology of catalyst design: [10, 11]

1) The adsorbent should neither be adsorbed too strongly nor too weakly.

2) The catalyst must bind the transition state more tightly than the substrate.

These principles will be discussed in the context of transition metal phosphide (TMP) electrocatalysts. To effectively design TMP electrocatalysts, we can draw inspiration from both thermal and electrocatalytic TMP literature, due to the similarities in reaction mechanism and binding modes of intermediates. [12–14]

Nanomaterials are of interest as heterogeneous (electro)catalysts because of their enhanced activity compared to bulk materials and overall economic viability due to their high surface area to volume ratio. Furthermore, by modifying the synthetic reaction conditions, the nanomaterial size, which controls the number of low-coordinated sites, and shape, which influences the faceting of the surface, can be tuned. [15–17] The systematic tuning of nanoparticle morphology can access more favorable surface binding for a reaction and enhance catalytic activity. [18] Beyond the particle itself, the surfaces of a nanomaterial can be passivated with ligands, which can be leveraged to alter reactant binding energetics as well. [19]

The synthesis of TMP nanocrystals has been well studied and their efficacy as (electro)catalysts is evident. [1, 20–23] In this chapter, we will thoroughly discuss the origin of TMP nanocrystal catalytic activity and the implications for the future of TMP electrocatalyst design.

1.3 Metal phosphides: a complex catalyst surface

Transition metal phosphides such as nickel phosphide, cobalt phosphide, and molybdenum phosphide, have been historically used as hydroprocessing catalysts in the petroleum industry, enabling critical hydrodenitrogenation (HDN) and hydrodesulfurization (HDS) reactions. [24–28] Over the

past two decades, TMPs have been attracting extensive attention for applications in energy conversion, [29,30] due to their exceptional activity for the hydrogen evolution reaction (HER). [31–34]

The origin of Ni_2P's exceptional HER activity is its structural complexity of TMP surfaces, which introduces several H adsorption sites with varying hydrogen binding energies (ΔG_{H^*}). [35] The various stoichiometries and structures of TMPs range from metal-rich (e.g., Ni_3P), [36] equal amounts of metal and phosphorus (e.g., CoP), to P-rich (e.g., NiP_3), [37] which are made possible by the highly covalent nature of metal–P bonds. [20] In addition, the crystal structures themselves vary significantly, often with multiple distinct metal and/or P sites within a unit cell [38]. These complex structures make analysis of TMP materials difficult and result in a large range of potential surfaces with a distribution of adsorption sites for substrates in catalysis. Figure 1.3 demonstrates the diversity of compositions, surfaces, and adsorption sites in the Ni–P system. Here, we see that at least three different binding motifs are available on a single surface of Ni_2P, which is also only one stoichiometry of Ni–P among a variety of different structures. This contrasts with transition metals whose structures have a tendency to be either body-centered cubic (BCC), hexagonal close-packed (HCP), or face-centered cubic (FCC) with predominantly low-index surfaces that are much simpler than those found on TMPs. These simpler surfaces typically have single adsorption sites that dominate activity, allowing for structure–activity relationships to be readily drawn.

The aforementioned structural complexity is an obvious, key difference between metals and TMPs: i.e., the relative heterogeneity of the individual surface sites. Li et al. showed that a metal surface such as Pt(111) only has a few types of adsorption sites that have similar computed ΔG_{H^*}s. [39] This finding suggests that a single value of ΔG_{H^*} can represent (or approximate) the formation energy of all adsorbed hydrogen (H*), including the active intermediates in catalysis. In contrast, TMP surfaces have a more diverse array of H adsorption sites (metal–metal bridge sites, metal hollow sites, P atoms, etc.). [35,36,39–41] Therefore, unlike on metal surfaces, HER on TMPs usually involves two H*s with different ΔG_{H^*}s. For example, Liu et al. demonstrated that hydrogen is first adsorbed at the Ni_3-hollow site ($\Delta G_{H^*} = -0.54\,\mathrm{eV}$) and then is adsorbed at the Ni–P bridge site ($\Delta G_{H^*} = 0.09\,\mathrm{eV}$). Their computational result suggested that the incorporation of P weakens the adsorption energy of a second hydrogen and favors the desorption of an H_2 molecule on $Ni_2P(0001)$. [35] Similarly, Hansen et al. found that the favorable pathway of HER on multiple facets of Ni_2P involves a second H* with a weaker ΔG_{H^*}. [41] Different stoichiometries of TMPs

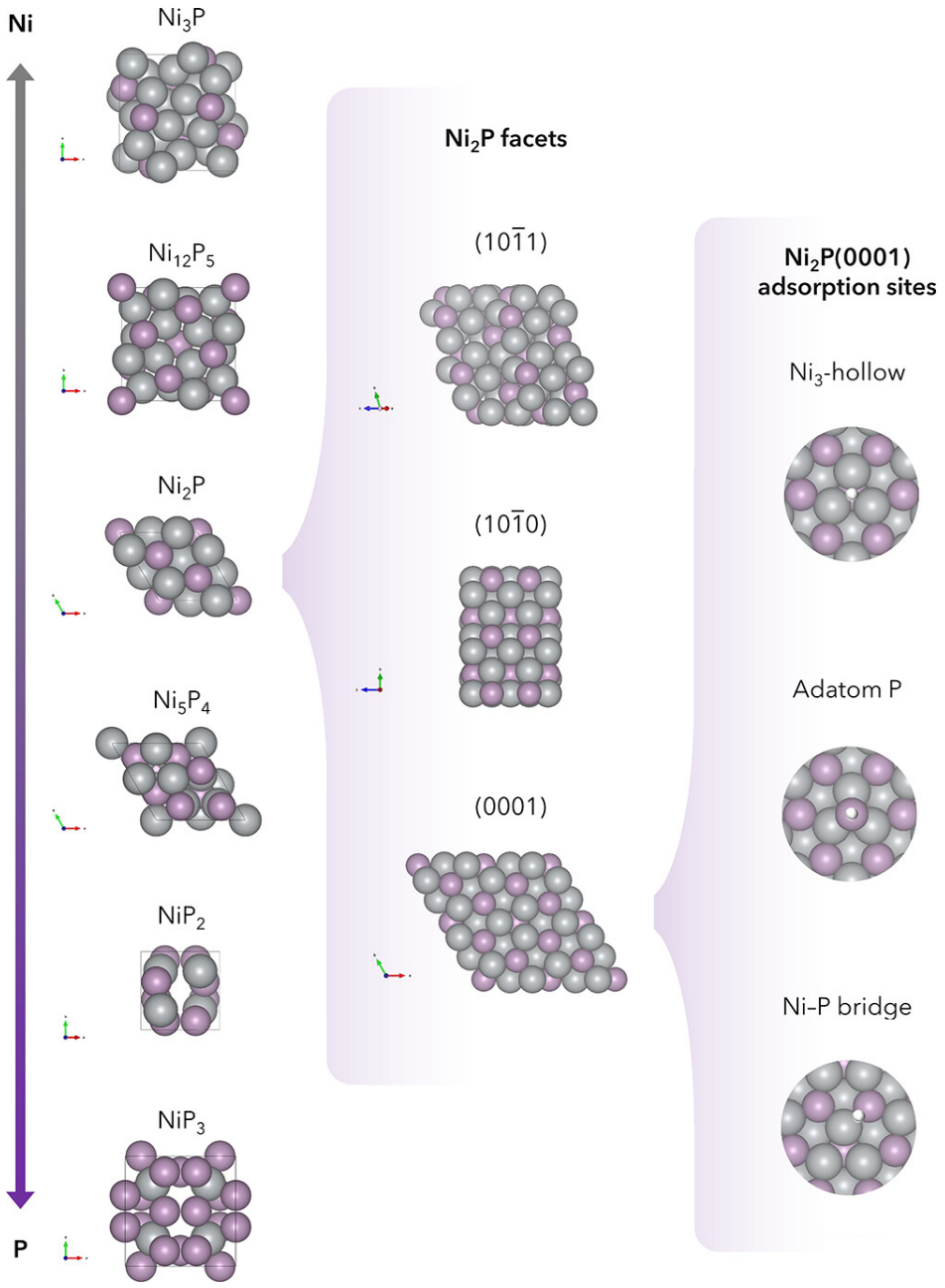

Figure 1.3: Complex structure of TMPs: the case of nickel phosphide. (Left panel) Structures of nickel phosphides with various Ni/P stoichiometries. (Middle panel) Representative low-index facets of Ni_2P. (Right panel) Representative H adsorption sites on the 0001 facet of Ni_2P.

also have differing dominant H adsorption sites; e.g., Ni_3P mainly adsorbs H via P-sites while Ni_2P adsorbs H mainly on Ni_3-hollow sites. This demonstrates that determining the active site(s) for HER for a specific TMP is nontrivial and, overall, suggests that the energetics of HER on TMP surfaces cannot be described by a single value of ΔG_{H^*}, in contrast to metal surfaces. [35, 37]

We note that transition-metal catalysts used in applications such as fuel cells usually are nanoparticles with multiple facets, various step edges, and defects. These features increase the adsorption site diversity that affects the ΔG_{H^*} on transition-metal surfaces. [42, 43] In addition, the presence of adsorbates may induce surface reconstruction and affect the ΔG_{H^*} due to adsorbate interactions. [44] This complexity associated with catalyst morphology and surface adsorbate interactions suggests that caution needs to be exercised in applying ΔG_{H^*} to rationalize activity trends for HER on transition-metal nanoparticles as well.

1.4 Challenges in TMP Catalyst Design

Electrocatalyst design is often based on the Sabatier principle, which states that the key reaction intermediate should not be bound too strongly nor too weakly. [9] Despite the diversity in H adsorption sites, a single value of ΔG_{H^*} has been frequently used to rationalize the HER activity trend on TMPs. [31] To measure ΔG_{H^*}, there are several theoretical and experimental methods are employed, which are discussed below.

1.4.1 Theoretical ΔG_{H^*} Calculations

First-principles calculation has been the primary method to estimate the ΔG_{H^*} and energetics of intermediates in the HER. [45,46] Briefly, the ΔG_{H^*} at a specific adsorption site on a given surface (often the most stable facet) is calculated and the value is used to represent the energy of the H_{ads} intermediate on the catalyst. However, it is not straightforward to access a single ΔG_{H^*} on TMP surfaces that is representative for catalysis due to the structural complexity. For example, the dominant facet of Ni_2P nanoparticles is size-dependent. Papawassiliou et al. found that (0001) surfaces dominate on Ni_2P ultrasmall nanoparticles (4 nm in diameter), but (1010) surfaces dominate with larger nanoparticles (12 nm in diameter). [47] Even on the same facet (i.e., $Ni_2P(0001)$), there are multiple possible surface terminations (e.g., Ni_3P_2 and Ni_3P terminations). [47, 48] In Figure 2, we summarize the computed ΔG_{H^*} on $Ni_2P(0001)$ [20, 31, 35, 41, 48–51] and CoP(101) [31, 52–54]

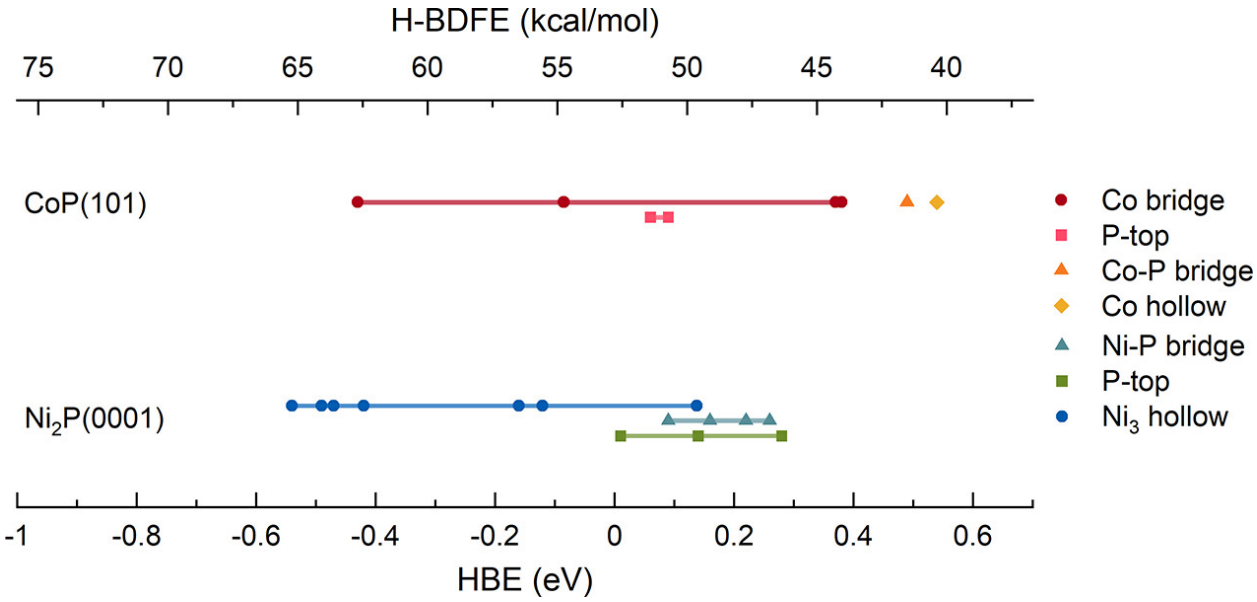

Figure 1.4: Hydrogen binding energy on $Ni_2P(0001)$ and CoP(101) from DFT calculations.

surfaces from reported values in the literature. The calculated ΔG_{H^*} at the Ni_3 hollow site on the $Ni_2P(0001)$ surface ranges from 0.137 eV to -0.543 eV. The calculated ΔG_{H^*} at the Co-bridge site ranges from 0.38 eV to -0.43 eV. This huge range may be due to the choice of functional, the slab structure, and the surface coverage used in the computation. Because of the large spread of the ΔG_{H^*}, justification of the choice of computation slab structure and validation from experimental results are recommended. In addition, the variety of different adsorption sites on TMP surfaces can further complicate the determination of ΔG_{H^*}. Figure 1.4 shows that Ni–P bridge sites and P top sites both show some distribution in ΔG_{H^*} such that there is overlap among these different adsorption sites. Consequently, an approach embracing the often overlooked complexity of TMP surfaces and the diversity of surface adsorption sites can help us to better understand key active sites and energies for the adsorption of H. Such approaches would be comparable to those used for high-entropy alloys where a distribution of adsorption energy at various sites are commonly used to understand the surface active sites. [55]

1.4.2 Experimental ΔG_{H^*} Calculation Methods

Here, we summarize three existing methods to measure (or estimate) the ΔG_{H^*} experimentally and their limitations to accessing ΔG_{H^*} on TMP surfaces.

H_2 Temperature-Programmed Desorption (H_2-TPD).

H_2-TPD has been used to monitor hydrogen desorption processes at the gas/solid interface. [56–59] The activation energy of desorption is governed by the Polanyi–Wigner equation. Trends derived from TPD measurements have been used to describe trends in ΔG_{H^*}. [60] Besides metal surfaces, H_2-TPD has been used to investigate the influence of P coverage on Ni(100) surfaces, where the incorporation of P reduces the ΔG_{H^*} of Ni. [59] H_2-TPD has also been used to study the interaction between H species and TMPs (i.e., Ni_2P, CoP) supported on silica, [61, 62] where HDS and HDN activities were attributed to the presence of strongly bound H. [56, 63] However, deconvolution of the H_2-TPD spectrum requires consideration of the delicate interplay of processes and a solid fundamental understanding based on well-defined surfaces.

Cyclic Voltammetry (CV).

CV has been a common technique for accessing ΔG_{H^*} on precious metals. [64, 65] It measures the free energy of electrochemical H formation on the surfaces, also known as underpotential H deposition. It is a surface-limited process, and the catalyst–H interaction needs to be stronger than the bond dissociation free energy of gas-phase H_2. This approach has been used to measure the ΔG_{H^*} and explain the pH dependency of HER/HOR activity on noble metal surfaces. [66, 67] Underpotential deposition of H has been observed on Rh_2P using CV as well. [30] However, to the best of our knowledge, no direct H adsorption process has been observed on Earth-abundant TMPs using CV. While underpotential deposition of Cu has been observed and used to estimate the active surface area for HER on cobalt phosphide, [68] the reason why there has been no observation of H underpotential deposition on TMPs remains unclear. The low coverage of H on these surfaces may be a factor.

Chemical Reactivity with Hydrogen Atom Transfer (HAT) Reagents.

The ΔG_{H^*} can also be estimated by studying the reactivity of a catalyst with a library of HAT reagents. [69] Delley et al. used this method to determine the hydrogen bond dissociation free energy (H-BDFE), which is equivalent to ΔG_{H^*}, on CoP nanocrystal surfaces. They found that the ΔG_{H^*} on CoP ranges from 51 kcal/mol (-0.078 eV) to 66 kcal/mol (0.574 eV). The ΔG_{H^*} on a catalyst surface is determined by comparison to the H-BDFE of the HAT reagents, which are well-documented. [70] If the ΔG_{H^*} on the catalyst surface is stronger than the H-BDFE of the HAT reagent, the H in the HAT reagent will be transferred to the catalyst surface, whereas no H atom transfer occurs if the ΔG_{H^*} is weaker. The ΔG_{H^*} in units of eV can be obtained by subtracting the H-BDFE of H_2 per H atom (52.8 kcal/mol in H_2O) [70] from H-BDFE in units of kcal/mol and dividing it by 23. Chemical reactivity with HAT reagents seems to be a viable method to show the range of ΔG_{H^*} on TMP nanoparticle surfaces. However, this method reveals the average ΔG_{H^*} across adsorption sites rather than the ΔG_{H^*} for the active intermediate of interest.

To accurately access and interpret the ΔG_{H^*} experimentally requires materials with well-defined surfaces, which is rare for TMPs, because their nanoparticles are typically multifaceted and spherical. [71,72] This makes fundamental experimental studies and comparison to computational studies difficult. We believe that measurements on nanoparticles with well-defined facets will be a path forward to reveal the range of ΔG_{H^*} on a given TMP surface and bridge computational and experimental results. This will require new synthetic methods to access monodisperse nanoparticles with well-defined facets, which, in turn, requires a detailed understanding of precursor and surface chemistry.

Given the difficulties in using theoretical calculations to simulate actual catalyst surfaces and experimental methods requiring well-defined surfaces to extract site-specific ΔG_{H^*}s, we want to emphasize the limitations these methods as guiding principles for HER catalyst design. We believe that measurements on TMP nanomaterials with well-defined facets will be a path forward to reveal the range of ΔG_{H^*} on a given TMP surface and bridge computational and experimental results. This will require new synthetic methods to access monodisperse nanoparticles with well-defined facets, which, in turn, requires a detailed understanding of precursor and surface chemistry.

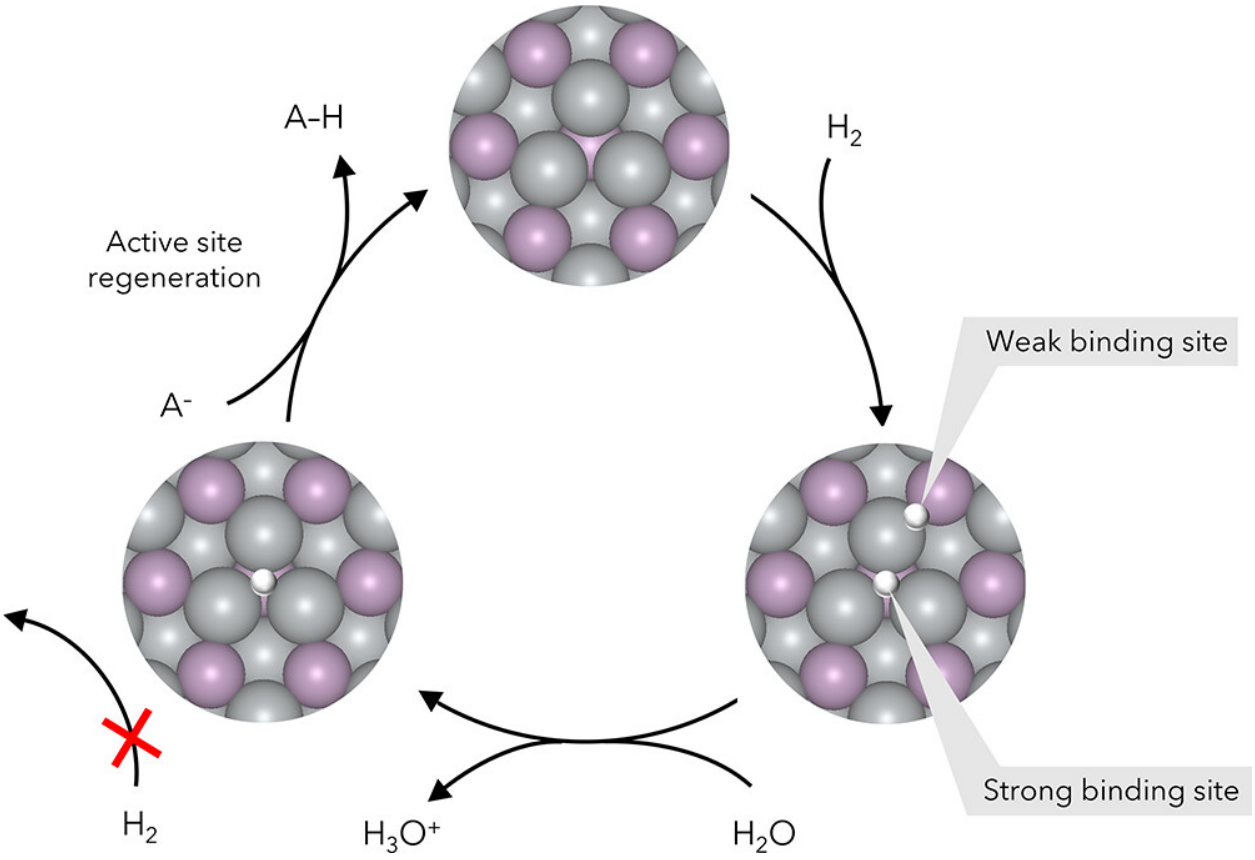

Figure 1.5: Schematic that shows the role of strongly bound H in hydrogenation reactions vs HOR. Gray, purple, and white spheres represent Ni, P, and H atoms, respectively. A^- is a strong H acceptor.

However, the challenges in using ΔG_{H^*} as a descriptor for TMP HER catalyst design raise ideas about the origin of a TMP material's inconsistent ability to catalyze HOR. Despite their remarkable HER activity, Parra-Puerto et al. showed that Earth-abundant TMPs supported on Vulcan carbon are inactive for HOR using a rotating disk electrode (RDE) setup. [73] This finding contrasts with the observation of correlation between HER and HOR on noble metal surfaces. [**?**, 74, 75] We attribute the poor HOR activity on TMP surfaces to HER and HOR not sharing the same key intermediate. In other words, the H* in the rate-limiting step is adsorbed at different sites in the two reactions. Previous computational studies suggested that the presence of H with a weaker ΔG_{H^*} on TMP surfaces (usually adsorbed at the metal-P bridge site) is the key for their HER activity. [35, 41, 48] However, the rate of HOR is more likely limited by desorption of the strongly bound H (usually adsorbed at the metal site), and its ΔG_{H^*} is often overlooked. Because the key intermediate binds to different adsorption sites, we believe that a single value of ΔG_{H^*} is not sufficient to explain HER and HOR activity trends.

We can take this idea further and apply it to rationalize TMP activity for hydrogenation reactions. Although the strongly bound H inactivates a TMP surface for the HOR, it can still serve as a source of H in hydrogenation reactions. One key example of this is with the thermal hydrogenation of NO_3^- to NH_3. Wei et al. observed that Ni_2P can facilitate the hydrogenation of nitrate to ammonia under mild temperature conditions. Interestingly, they also found that Ni_2P annealed under H_2 can still hydrogenate nitrate in an inert atmosphere, implying the presence of H* on the surface of Ni_2P after annealing. [76] This empirical evidence suggests that H_2 can dissociate and form H* on the Ni_2P surface, and the H-BDFE of ceNi2P is stronger than the H-BDFE of a H_2 molecule (52.8 kcal/mol). [70] We believe that this H is absorbed at a stronger binding site (e.g., the Ni_3 hollow site). This hydrogen can be transferred to a substrate with a higher H-BDFE such as nitrate. The redox potential of nitrate to ammonia at pH 0 is 0.88 V vs. SHE, which suggests a strong tendency to accept H* from Ni_2P. The regenerated empty site can participate in H_2 dissociation, turning over the catalytic reaction. In contrast, without the H acceptor (e.g., nitrate), the stronger binding site will be "poisoned" by H* and the reaction will not turn over. This could be the reason why TMPs are active for hydrogenation reactions but inactive for HOR. There are several examples of TMP-catalyzed hydrogenation reactions, which will be discussed in the next section.

1.5 The role of adsorption site diversity in reactions beyond HER

Metal phosphides have been extensively demonstrated as (electro)catalysts for more complex, multi-electron (electro)catalytic reactions. Based on our survey of the literature, we postulate that the presence of a diversity of surface sites is key in catalyzing these chemical transformations. These surfaces can create local active site motifs that allow groups of adsorbed intermediates to readily react with each other. Understanding the impacts of these motifs is crucial for more complex chemical reactions whose mechanisms cannot solely be described by the binding of H. Specifically, we believe that the diversity in adsorption sites on TMPs is advantageous for complex thermal (e.g., CO_2 transformations, [77–82] transfer hydrogenation, [83–85] nitrate hydrogenation, [76] and HDS [86]), electrochemical (e.g., CO_2 reduction [87–90] and NO_3^- reduction [91, 92]), and photochemical reactions. [93–95] Below we discuss 3 examples of thermal and electrocatalytic reactions that experimentally demonstrate the key role of adsorption site diversity on TMP catalysts.

1.5.1 Thermal hydrodesulfurization

HDS of thiophenes has been demonstrated with MoP/SiO_2,which is almost four times more active than Mo/SiO_2. [96] Ni_2P on various SiO_2 supports has demonstrated higher activity,compared to a commercial Ni-based catalyst for HDS. [28] Theoretical work postulated that phosphorus plays a key role in TMP-catalyzed HDS. A DFT study by Liu et al. has claimed that the combination of Ni and P sites avoids surface deactivation by strongly bound sulfur. For example, incorporation of phosphorus creates a Ni–P bridge site, where H_2S desorption becomes more favorable by 0.7 eV, compared to when S is bound to a Ni_3–hollow site. [86] More recent work on Ni_2P-catalyzed HDS has proposed that a phosphosulfide phase on the (1010)–Ni_2P-terminated surfaces may be responsible for the high activity of Ni_2P for HDS. This facet has reduced S-poisoning due to surface phosphorus and sulfur substitution and optimized Ni_3–site geometry that alter binding energetics. [26]

1.5.2 Reverse water gas shift reaction

DFT studies on the Ni_2P- and MoP-catalyzed reverse water gas shift (RWGS) reaction have attributed the ability of these catalysts to favorable dissociation of H_2 on these surfaces. [97] Similar to HDS, we believe it is necessary to think about the role of phosphorus and how it impacts the ad-

sorption of other intermediates (i.e., CO_2). Cui et. al. used TPD to measure the affinity of H_2 and CO_2 for catalyst surfaces. They attributed Ni_2P's weaker affinity for CO_2 and stronger affinity for H_2,compared to that of Ni, as the source of higher selectivity for CO over methane. [78] Zhang et al. showed that Ni_2P/SiO_2 can achieve 90% CO selectivity from 300–750 °C, [98] corroborating the results seen by Cui et al. These studies demonstrate the advantage of a diversity in adsorption sites for catalyzing more complex thermal reactions that require the adsorption of intermediates with different binding strengths.

1.5.3 Electrochemical CO_2 reduction

Considering intermediates other than H* is important in electrochemical CO_2 reduction as well, where a common theory is that a binary surface creates local hydride sources for facile CO_2 hydrogenation. [99] This concept has been used to rationalize electrochemical CO_2 reduction on nickel and iron phosphides, where experimental studies have shown that the application of low overpotentials can mitigate HER and direct selectivity toward multicarbon and oxygenated products. [87,90] DFT studies on Ni_2P have claimed that,compared to bare metal surfaces, the binary surface of a TMP can facilitate CO_2 hydrogenation by promoting migration of H* to Ni sites with weaker ΔG_{H^*}s. Additionally, the presence ofa multitude of H adsorption sites results in exergonic C-C coupling via $\cdot H_2CO$ self-condensation, which drives selectivity toward multicarbon and oxygenated products instead of H_2. [99] The complexity of TMP surfaces is a tuning knob for CO_2 reduction reaction selectivity that distinguishes them from monometallic materials. We note that other factors, such as Ni:P ratio and the identity of the catalyst support can also playa role in reaction kinetics, mainly by modulating surface energetics. [93, 98] However, we believe that the role of local active site motifs present on TMP surfaces is crucial when considering their (electro)catalytic behavior.

1.6 Motivating the study of NO_3^- electroreduction

We chose to study NO_3^- electroreduction catalyzed by Ni_2P nanocrystals due to literature precedent that demonstrated that Ni_2P can thermally catalyze NO_3^- hydrogenation fo NH_3. [76] We propose that analogous to previous studies on nickel phosphide-catalyzed CO_2 electroreduction, the mechanism of NO_3^- electroreduction will rely on the local co-adsorption of a nitrogenous species (NO_x) and H* to generate ammonia (Fig. 1.6).

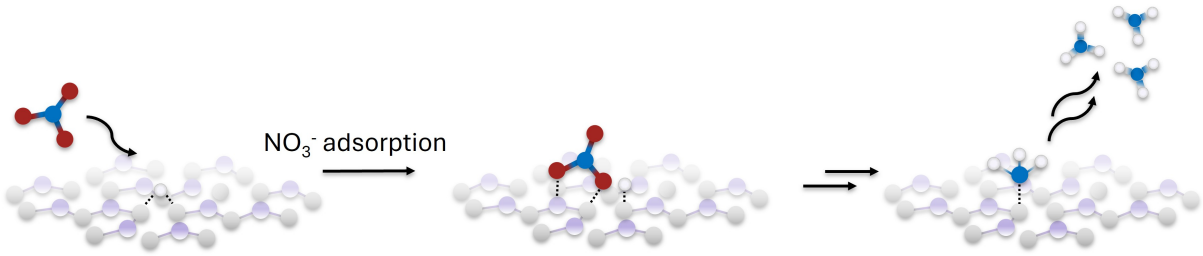

Figure 1.6: A proposed mechanism of NO_3^- electroreduction on a Ni_2P surface that demonstrates the critical role of co-adsorption.

Practically, ammonia is an essential fertilizer that supports global food demands and is industrially produced via the Haber-Bosch process ($N_2 + 3H_2 \rightarrow 2NH_3$), which combines gaseous nitrogen and hydrogen at high temperatures and pressures with an iron-based heterogeneous catalyst. [100] However, the enormous scale of ammonia production and deployment has disrupted the nitrogen cycle. Imbalances of NO_3^- in wastewater and extraneous nitrous oxides emitted into the atmosphere from burning fossil fuels for H_2 production have resulted in ecosystem destruction and climate change. [101, 102] Anthropogenic disturbances to the nitrogen cycle motivate alternative ammonia generation methods that do not exacerbate these imbalances. One alternative is the the electroreduction of NO_3^-, which can upcycle NO_3^- to NH_3 and assist in restoring balance to the N_2 cycle. [103]

Interestingly, a cost analysis using a Ru-based catalyst estimates that NO_3^- electroreduction to NH_3 would only be \$200 more expensive than the Haber-Bosch process, demonstrating the viability of this reaction on an industrial scale. However, there are numerous practical challenges of NO_3^- electroreduction, such as the acquisition of sufficiently concentrated NO_3^--contaminated wastewater, the separation of NH_3 from water streams, and the large amounts of H_2 produced as a side product and reducing the overall efficiency of the process. While these challenges have yet to be resolved, the potential for sustainable ammonia synthesis without the use of fossil fuels is enticing. Furthermore, this method opens up the potential for smaller scale, decentralized ammonia synthesis, which can provide easier access to ammonia-based fertilizers in developing countries. [103, 104]

Beyond the engineering challenges in commercializing this process, there is a lack of cost-effective, earth-abundant catalysts that can compete with the industrial Haber-Bosch process. Therefore, we aptly chose to investigate whether TMP nanomaterials are potential catalysts for NO_3^- electroreduction. By doing so, we sought to bridge knowledge from thermal and electrocatalysis literature to 1) evaluate the role of active site ensembles in this reaction and 2) demonstrate the catalytic abilities of TMPs for this reaction.

1.7 Conclusions

We have discussed the influence of adsorption site diversity and inherent in the structural complexity of TMPs on catalysis. The array of adsorption sites with a wide range in ΔG_{H^*} creates a more energetically favorable pathway for HER on TMP surfaces; however, it challenges whether a single value of ΔG_{H^*} can describe an activity trend. We argue that a single value of ΔG_{H^*} is not sufficient to rationalize HER and HOR activity trends, because hydrogen may adsorb at different sites. The diversity of adsorption sites also introduces challenges in bridging computational and experimental results, because of large discrepancies in calculated TMP ΔG_{H^*} values and difficulties in characterizing the surface of a catalyst. Most importantly, the diversity of sites present on TMP surfaces is crucial in understanding mechanisms of more complex reactions involving hydrogen, such as CO_2 or NO_3^- reduction. The number of literature reports that attribute catalytic activity to phosphorus creating local active site motifs that simultaneously adsorb different intermediates indicates the applicability of these concepts across a wide variety of TMP catalysts. Experimentally, we posit that controlled synthetic design of TMP-based materials with desirable active site motifs can move us closer to designing and understanding the origin of activity for various electrocatalytic reactions. We believe that such efforts to develop a systematic understanding of the role that a diversity of sites plays in complex reactions is critical to advancing catalyst design.

Chapter 2

AN IN-DEPTH STUDY ON Ni_2P'S ELECTROCATALYSTS FOR NO_3^- ELECTROREDUCTION

This chapter is adapted from: Nishiwaki, E., Cossairt, B. M., et al. Ni_2P Active Site Ensembles Tune Electrocatalytic Nitrate Reduction Selectivity. Chemical Communications, **2024**, 60, 6941-6944. [105]

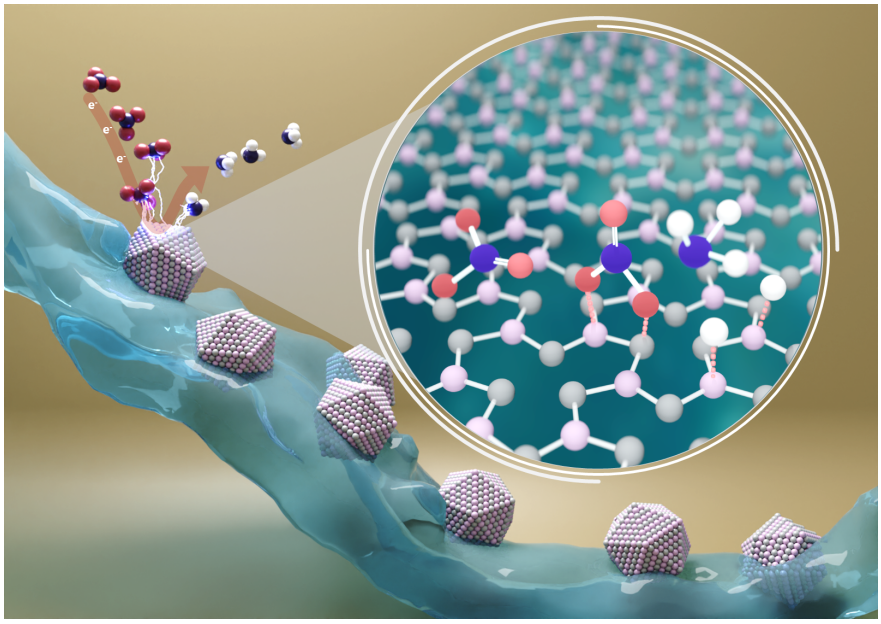

Figure 2.1: Ni_2P nanocrystals are electrocatalysts for aqueous NO_3^- electroreduction. The reaction mechanism involves the co-adsorption of intermediates and leverages Ni_2P active site ensembles.

2.1 Introduction

As discussed thoroughly in Chapter 1, metal phosphides are known to have active site ensembles of adjacent strongly and weakly H-binding sites. [106] On these surfaces, strongly bound H can

hydrogenate NO_x*, which can bind on a vacated site that only weakly adsorbs hydrogen. [2] Density functional theory (DFT) calculations have suggested that active site ensembles of strongly and weakly binding hydrogen sites are responsible for Ni_2P's HER activity. [32, 35, 107, 108] The importance of these ensembles has also been realized in more complex electrocatalytic reactions such as CO_2 electroreduction, where several metal phosphides have demonstrated the ability to form oxygenated hydrocarbons. [87, 90, 99, 109, 110] The binary surfaces of metal phosphides result in an increased number of unique surface sites and a distribution of adsorbate-binding energetics, which enhance their ability to co-adsorb different species.

We sought to extend these principles and investigate Ni_2P's as an electrocatalyst for NO_3^- electroreduction. State-of-the-art catalysts for this reaction include noble metals, [111–115] while current electrocatalyst design research focuses on using earth-abundant metals to achieve similar current densities. [116–118] Several studies have proposed a NO_3^- electroreduction mechanism that involves the co-adsorption of hydrogen (H*) and nitrogenous species (NO_x*) and the sequential deoxygenation-hydrogenation to convert NO_3^- to NH_3 on transition metal surfaces. [119–121] TMP-catalyed NO_3^- electroreduction has been demonstrated with numerous types of nanomaterials, which justifies the need for a more thorough mechanistic investigation with these materials. [92, 122–129]

Thermal NO_3^- hydrogenation studies with Ni_2P and Ni nanocrystals showed Ni_2P's near unity selectivity toward NH_3 under mild conditions, while Ni nanocrystals had almost no conversion of NO_3^-. [76] This confirms the importance of a multi-elemental catalyst and motivates the investigation of nickel phosphide materials as electrocatalysts for NO_3^- electroreduction. Although previous theoretical work on Ni_2P electrocatalysts for NO_3^- electroreduction has highlighted the critical role of Ni_2P's ability to co-adsorb NO_3^- and H, [125, 128] corroborating experimental data has not yet been reported.

In this study, we investigate the nitrate electroreduction behavior of Ni_2P nanocrystals as a case study to elucidate the role of metal phosphide active site ensembles on NO_3^- electroreduction behavior. Our rate order analysis suggests a mechanism with competitive adsorption, which we use to understand the selectivity of Ni_2P for nitrate electroreduction over a range of reductive potentials.

2.2 Catalyst preparation

2.2.1 Synthesis and characterization of Ni_2P nanocrystals

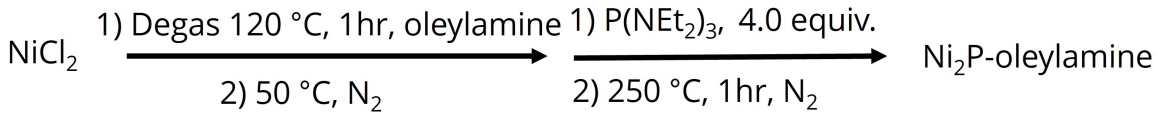

Figure 2.2: Reaction scheme for the synthesis of oleylamine-capped Ni_2P nanocrystals. $P(NEt_2)_3$ = tris(diethylamino)phosphine.

$NiCl_2$ and tris(diethylamino)phosphine were used as received. Oleylamine (70%, technical grade) was purified via vacuum distillation. All reagents were dried and kept under inert conditions. Ni_2P nanocrystals were synthesized with a Schlenk line under inert conditions according to previous methods developed in our lab. [1,20] 5.46 mmol of $NiCl_2$ (1 eq.) and 109.5 mmol of oleylamine (21 eq.) were degassed at 120 °C for 60 minutes. The temperature was lowered to 50 °C and 21.6 mmol of tris(diethylamino)phosphine (4 eq.) was injected. The temperature was ramped to 250 °C and was held for 60 minutes. The nanoparticles were purified via centrifugation in the glove box with a pentane/IPA mixture (4x, 7830 rpm, 10 minutes each spin) and toluene/acetonitrile mixture (1x, 7830 rpm, 10 minutes).

X-ray diffraction (XRD) and transmission electron microscopy (TEM) measurements show monodisperse, 5.4 ± 0.8 nm nanocrystals.

2.3 Catalyst ink preparation

$$samplemass = \frac{mass_{VC} * 0.3}{massfrac} \tag{2.1}$$

Ni_2P nanocrystals were deposited onto Vulcan carbon (Ni_2P/C) to prevent aggregation during annealing. Previously reported methods were used with modifications. [130] 30 wt% of Ni2P (excluding ligand mass) was deposited onto Vulcan carbon. For the deposition, 100 mg of Vulcan carbon was dried in a 100 mL Schlenk flask at 100 °C overnight. Vulcan carbon was transferred into

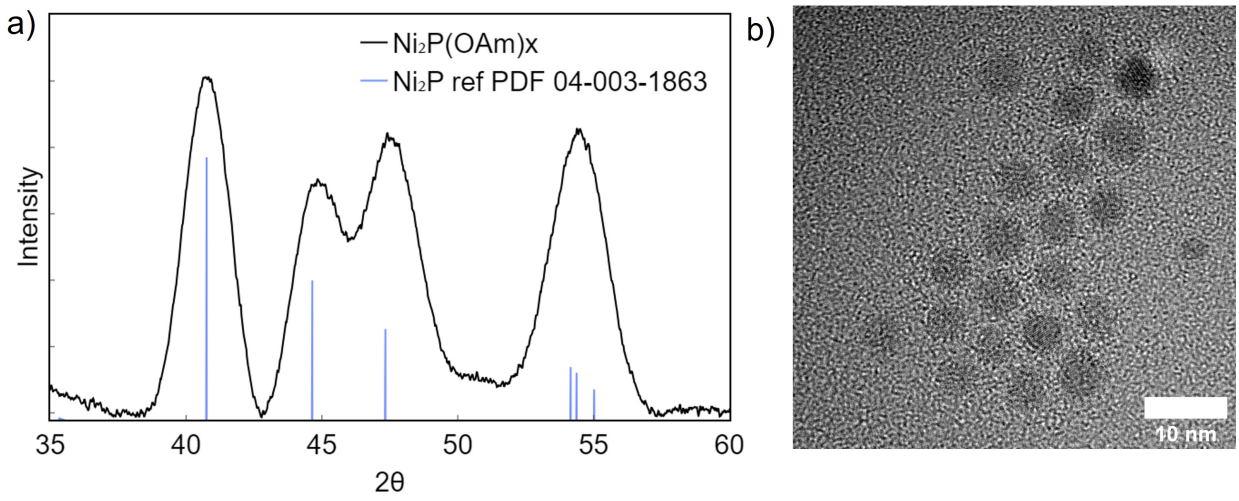

Figure 2.3: a) XRD and b) TEM images of Ni_2P nanocrystals (5.4 ± 0.8 nm) capped by oleylamine ligands. The reported size is the diameter of the particles. The diameter of 200+ particles were measured in two orthogonal directions for each particle (400+ total measurements). The measurements were averaged and the "±" indicates the standard deviation.

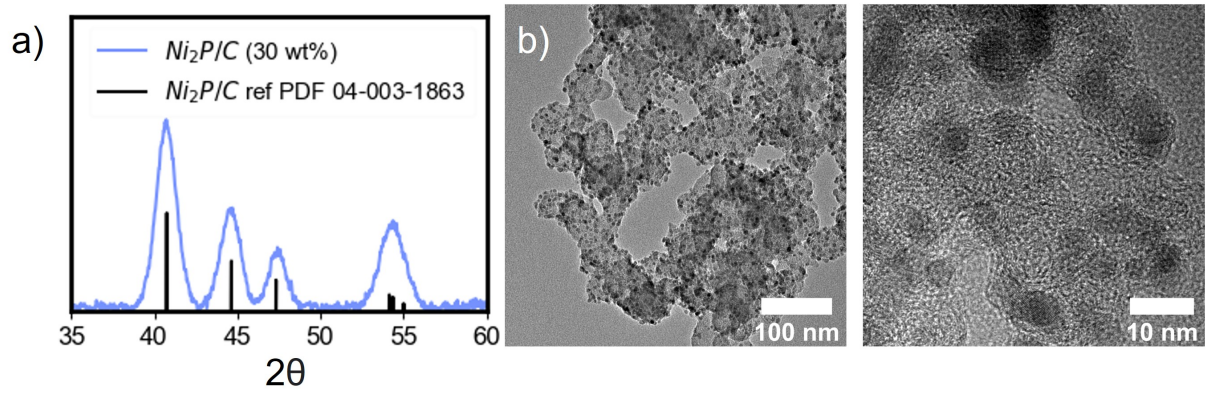

Figure 2.4: a) XRD and b) TEM images of Ni_2P nanocrystals deposited on Vulcan carbon and annealed (Ni_2P/C).

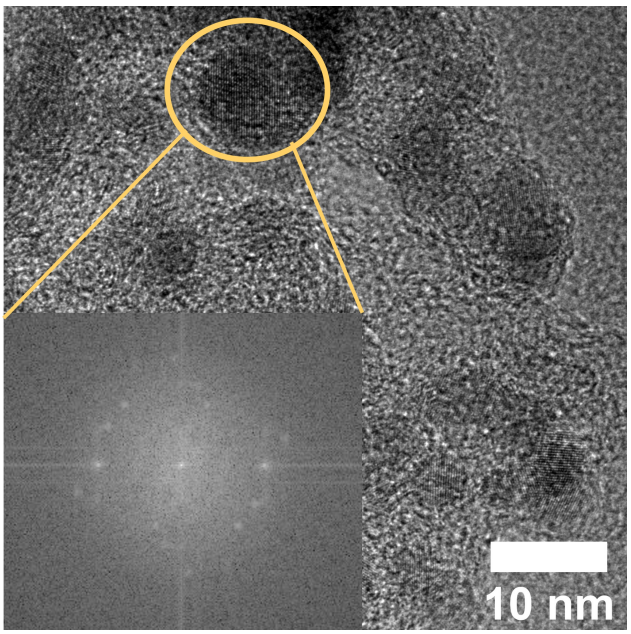

Figure 2.5: A sample FFT image of a Ni_2P nanocrystal. Measurements of a sample of nanocrystals showed a predominant lattice spacing of 0.22 nm, indicating the majority of particles are (111)-faceted.

a glovebox and dispersed in 20 mL pentane then sonicated for 5 minutes. The carbon dispersion was stirred at 1500 rpm and the desired amount of a 5 mg/mL Ni_2P stock solution in chloroform was added dropwise. The exact amount of stock solution used was determined via back-calculation from the mass% of the nanocrystals, as determined by TGA (2.D.1, 2.1). The mixture was then sonicated for 5 minutes and transferred back to a glovebox stirring at 1500 rpm overnight. The next day, 15 mL of acetonitrile was added slowly while the suspension was stirred at 800 rpm. The mixture was centrifuged at 7830 rpm for 10 minutes and the clear supernatant was decanted. The precipitate (Ni_2P/C) was re-dispersed in 10 mL isopropanol. The Ni_2P/C was annealed at 450 °C for 2 hours under 95:5 N_2:H_2 gas. All sample handling was performed under inert conditions to preserve the Ni_2P nanocrystals.

XRD and TEM measurements of Ni_2P/C demonstrate the retention of the Ni_2P crystal structure post-annealing with mild ripening to 5.8 ± 1.5 nm (Fig. 2.4). Fourier transform analysis of the particle lattice fringes reveals predominantly (111)-faceted nanocrystals after the annealing treatment (2.5).

2.4 Electrochemical methods

All measurements were performed in a H-cell, where a Nafion membrane separated the cathodic and anodic compartments (Fig. 2.A.1). 0.1 M phosphate buffer (pH 6.9) was prepared via a 1:1 ratio of KH_2PO_4:K_2HPO_4. All measurements were conducted with an Ag/AgCl reference electrode and Pt counter electrode. Carbon paper working electrodes (FuelCell Store, AvCarb MGL190) with Ni_2P nanocrystals were prepared by sonicating and then immediately drop-casting 30 μL of a 10 mg/mL solution of Ni_2P/C onto a 1 cm x 1 cm carbon paper electrode (90 μg of Ni_2P on each electrode). Carbon paper electrodes were 0.88 cm^2 ± 0.1 cm^2. Ni/C electrodes were prepared with identical methods.

2.5 Identifying the non-innocent role of electrolyte

We performed cyclic voltammetry using Ni_2P/C with varying concentrations of KNO_3 to demonstrate Ni_2P/C's activity for NO_3^- electroreduction (Fig. 2.4a). We attribute the two features to the catalytic activity being mediated by two different sources: $H_2PO_4^-$ and H_2O. With 0 mM KNO_3, we can isolate the catalytic activity to HER. Under these conditions, HER activity first exhibits a

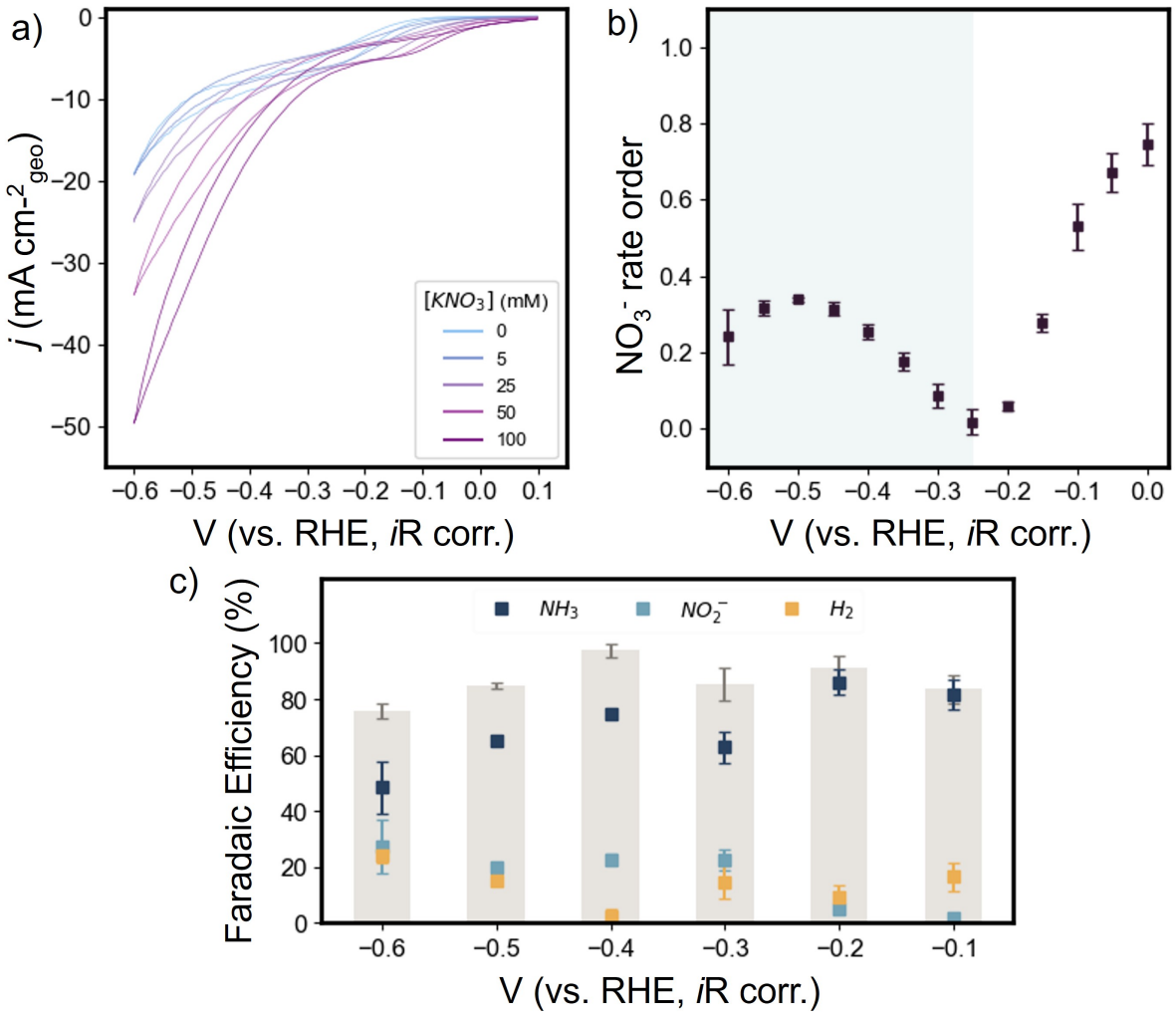

Figure 2.6: a) Cyclic voltammograms of Ni_2P/C in 0.1 M KH_2PO_4/K_2HPO_4 buffer at a series of KNO_3 concentrations. b) Potential-dependent NO_3^- rate order. The region highlighted in blue (−0.25 V) indicates a competitive Langmuir-Hinshelwood mechanism. c) Potential-dependent selectivity with 100 mM of KNO_3

diffusion-limited response near −0.3 V due to the H-source being $H_2PO_4^-$ ($pKa_{H_2PO_4^-}$<pKa_{H_2O}). As the potential increases and the water dissociation potential is reached, the HER current resembles the expected catalytic wave, indicating that the H-source is H_2O. [131] As we increase the concentration of KNO_3, we observe diffusion-limited NO_3^- electroreduction at low cathodic potentials in the phosphate-mediated region. In both regions, there is a decrease in onset potential and an increase in current density associated with an increased concentration of KNO_3, demonstrating Ni_2P/C's activity for NO_3^- electroreduction.

2.6 Microkinetic analysis of NO_3^- electroreduction mechanism on Ni_2P nanocrystals

The series of cyclic voltammagrams can also be utilized to probe the mechanism of NO_3^- electroreduction via microkinetic modeling. This method breaks down a complex reaction into several elementary steps to elucidate kinetics on a catalyst surfaces rather than substrates freely colliding in space or in a liquid. [132] Previous literature has developed a microkinetic model for NO_3^- electroreduction, which work will be summarized briefly here in the context of this chapter. [131]

2.6.1 Explanation of the microkinetic model

Carvalho and coworkers postulated that a rate limiting step involves the reduction of NO_3* to NO_2* and derived a rate expression based on this assumption (Eq. 2.2, 2.3):

$$NO_3^* + 2H^* \leftrightarrow NO_2^* + H_2O + 2^* \tag{2.2}$$

$$rate = nFk_f^0\theta_H^2\theta_{NO3} \tag{2.3}$$

By defining a rate-limiting step, they solved for the coverage terms (θ_H, θ_{NO3}) using the other elementary steps of the overall reaction (2.4 and 2.5):

$$\theta_H = \frac{K_H a_H(1-\theta_{NO_3})}{\exp(f\eta)(K_H a_{H^+})} \tag{2.4}$$

$$\theta_{NO3} = \frac{K_{NO3}a_{NO3}(1-\theta_H)}{(1+K_{NO3}a_{NO3})} \tag{2.5}$$

From these expressions, we can see that coverage of H* and NO_3* are dependent on numerous factors: concentration, the relative equilibrium binding constants of the substrates, and therefore the relative binding strengths of two. There is also a potential dependence on H* coverage, which indirectly causes θ_{NO3} to be potential dependent as well. By using microkinetic modeling it is clearly demonstrated how coverage of reaction intermediates is difficult to control and clearly dependent on the relative binding strengths of the intermediates. In the context of metal phosphide materials, our goal was to understand whether active site ensembles are playing an active role in mechanism of NO_3^- electroreduction, i.e., that there is co-adsorption occurring.

Previous literature has demonstrated that in a competitive adsorption, or Langmuir-Hinshelwood mechanism, a plot of the rate order as a function of potential will result in a peak-like shape. [131, 133] We generated this plot by extracting the data from the cyclic voltammagrams in Fig. 2.6 Specifically, the NO_3^- rate orders were extracted from the logarithmic relationship between the current at a given potential and the concentration of KNO_3 (Fig. 2.B.1, Eqs. 2.6, 2.7).

$$rate = k[NO_3^-]^x \tag{2.6}$$

$$log(i) = xlog([NO_3^-]) + log(k) \tag{2.7}$$

2.6.2 Application to Ni_2P nanocrystals

By varying the concentration of KNO_3 and determining the nitrate rate order over a range of potentials, we gained insight into the adsorbate dynamics on the catalyst surface. In the H_2O-mediated region (> -0.25 V, highlighted in blue in Fig. 2.6b), we observe an inverted-parabolic shape, which suggests that NO_3^- electroreduction is proceeding via a Langmuir-Hinshelwood mechanism, where adsorbed hydrogen (H*) and nitrogenous species (NO_x*) are co-adsorbed intermediates, and the coverage ratio between the two dictates selectivity between NO_3^- electroreduction and HER. This conclusion assumes that the rate-limiting step is the reduction of NO_3* to NO_2*, which has been proposed in previous studies. [119, 134] The potential of maximum rate order (> -0.5 V) occurs when the H*:NO_x* coverage ratio is optimized for selective NO_3^- reduction.This potential is more negative for Ni_2P than previously measured for copper and nickel foils, [131] suggesting that Ni_2P

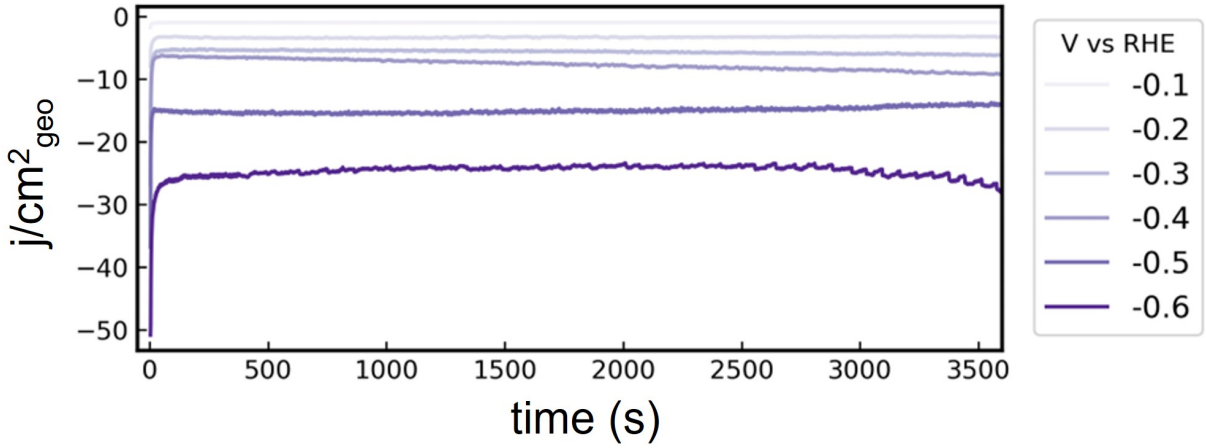

Figure 2.7: Chronoamperometry of Ni_2P/C from -0.1 V to -0.6 V vs. RHE.

can suppress HER over a wider potential window. We propose that Ni_2P's active site ensembles enable more optimal relative binding of H* and NO_x*, which is reflected by the shift in the potential of maximum rate order to more cathodic potentials.

We also observe a decreasing NO_3^- rate order in the phosphate-mediated region (> -0.25 V) as we move to more negative potentials. We attribute this decrease to the rate being limited by $H_2PO_4^-$ ($[H^+]$ or coverage of H*) instead of NO_3^-, which is supported by the presence of the $H_2PO_4^-$ deprotonation peak in Fig. 2.6a. This rate order analysis assumes that the rate of NO_3^- electroreduction and HER are independent; however, assuming they are dependent results in identical conclusions (2.B.1).

Excitingly, this rate order analysis supports our hypothesis that Ni_2P/C can simultaneously co-adsorb multiple intermediates required to reduce NO_3^- to NH_3. We use this as a foundation to understand the selectivity of Ni_2P over a range of potentials, which is discussed in the next section.

2.7 Investigating the selectivity of Ni_2P/C

We conducted chronoamperometry with the Ni_2P nanocrystals and quantified the reaction products (2.6c, 2.7). NH_3 and NO_2^- were quantified with previously reported UV-visible colorimetric

methods (Fig. 2.A.2, 2.A.3 see SI). After considering three possible reaction pathways for NO_3^- electroreduction to NH_3, [120, 135] DFT calculations suggest that NH_3 is formed by an 8 e^- sequential deoxygenation and hydrogenation pathway with a NO_2^- intermediate (Fig. 2.9). *In situ* mass spectrometry measurements confirmed that the sole gaseous product is H_2 at $-0.6\,V$ from the competing HER (Fig. 2.A.4). We believe H_2 is the sole gaseous product over the entire range of potentials due to the lack of N_2 and N_2O (which should have more sluggish kinetics than the other thermodynamically accessible products) at the most cathodic potential in the series.

Bulk electrolysis results reveal that Ni_2P/C has $> 60\%$ Faradaic efficiency (FE) toward NO_3^- electroreduction at all tested potentials and nearly 100% FE at $-0.4\,V$. As potential decreases, NH_3 selectivity decreases and the production of H_2 and NO_2^- increases. We propose that the reaction selectivity is dictated by the ratio of H* and NO_x* on the surface, which is tuned by the applied potential. At low cathodic potentials ($\geq -0.2\,V$) where NO_3^- reduction is mediated by $H_2PO_4^-$, we observe ¿80% NH_3 FE and 15–20% H_2 FE, with minimal NO_2^- production. We propose that the diffusion-limited nature of $H_2PO_4^-$ allows NO_x* to saturate the surface and decreases the ratio of H*:NO_x*. This coverage ratio favors the hydrogenation of NO_x* species to NH_3 over the formation of NO_2^- and H_2. [136, 137]

In the H_2O-mediated region ($\leq -0.3\,V$), we observe near 100% FE toward NO_3^- electroreduction at $-0.4\,V$, which suggests a surface coverage that almost completely inhibits HER activity, i.e., an ideal ratio of H*:NO_x* for selectively performing NO_3^- electroreduction. Deviation from the ideal H*:NO_x* ratio results in lower NO_3^- electroreduction selectivity. At $-0.3\,V$, we observe a rise in NO_2^- selectivity relative to $-0.2\,V$ due to H*:NO_x* being too low. Conversely, as potentials become more cathodic of $-0.4\,V$, the H*:NO_x* ratio increases and favors H_2 formation by promoting H-H coupling over NO_x* hydrogenation, decreasing overall NO_3^- reduction selectivity.

2.8 Supporting DFT Calculations

Complementary to the experiments, we also performed DFT calculations on a Ni_2P surface to disentangle the influence of NO_x* and H* co-adsorption on their respective energetics and reaction selectivity. Systematic exploration of various nitrogenous species reveals that co-adsorption of nitrogenous species and H* modulates ΔG_{H^*}, the key binding mode of nitrogenous species, and the overall free energy profile of the reaction (2.8, 2.9), which is consistent with previous work. [138]

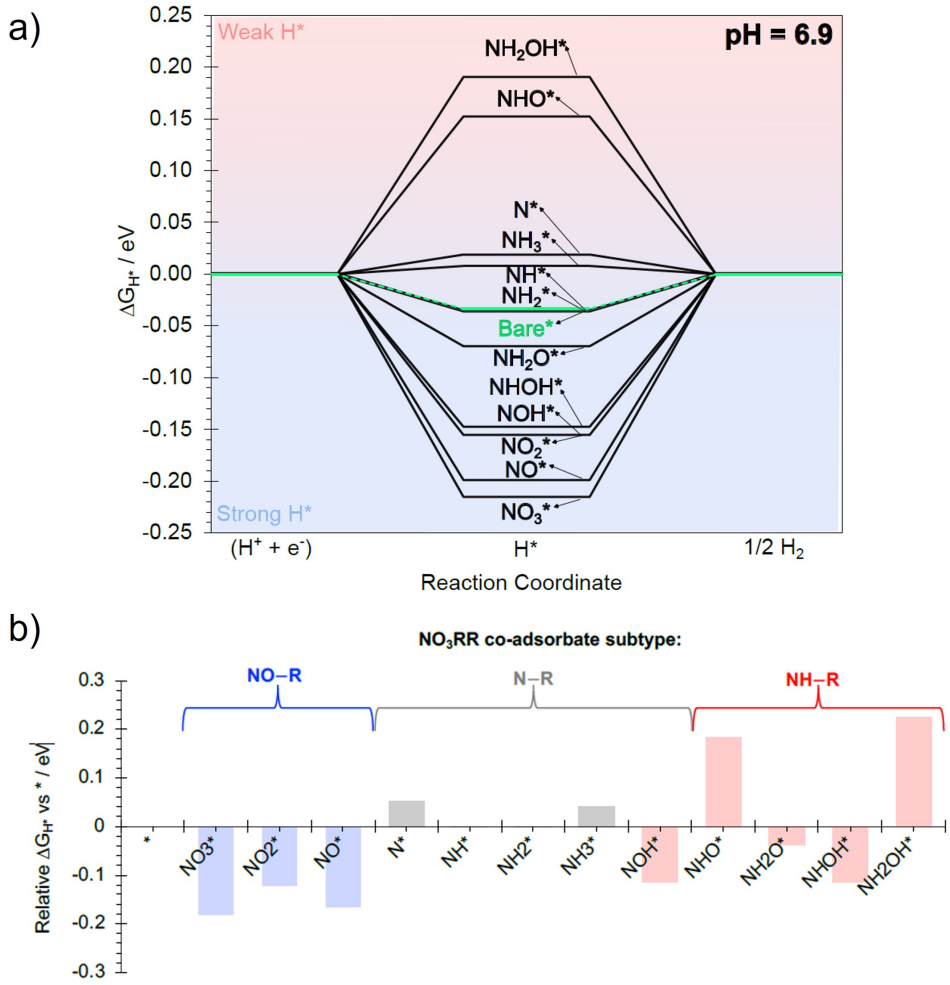

Figure 2.8: a) Calculated free energy profile at 0.00 V vs. RHE, pH = 6.9, and 300 K for the adsorption of H* onto the Ni_3 hollow site of the Ni_3P_2 terminated surface, with and without surface functional groups. b) Plot showing the relative hydrogen adsorption free energy as a function of co-adsorbed species relative to ΔG_{H^*} on the bare Ni_2P surface (*), at pH = 6.9 and T = 300 K. The colors correspond to the co-adsorbate subtypes consisting of NO-R (blue), N-R (grey) and NH-R (red) containing species.

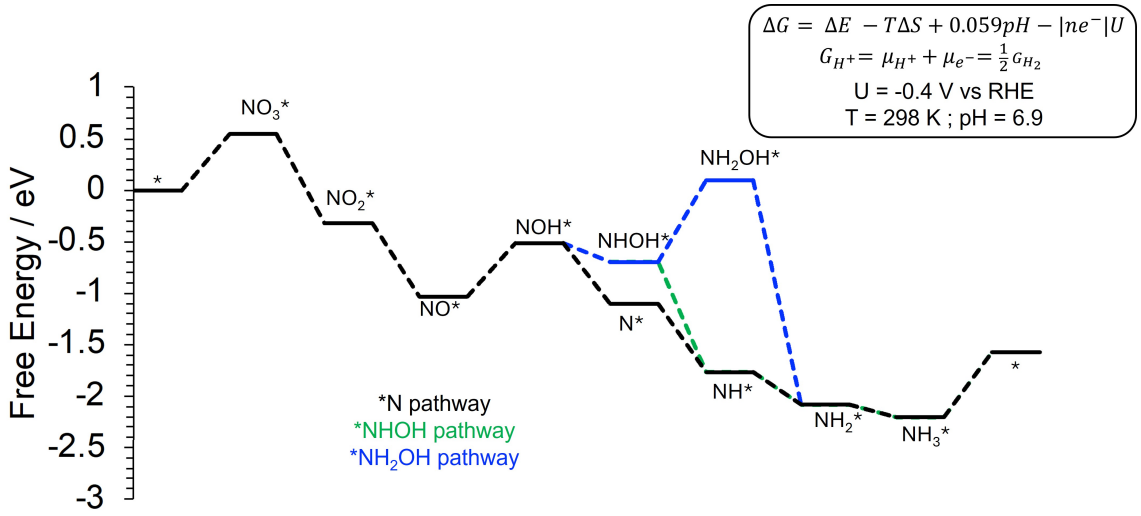

Figure 2.9: Various reaction pathway for NO_3^- electroreduction on Ni_2P at -0.4 V vs. RHE.

ΔG_{H^*} can be modulated by as much as 0.40 eV, where oxygenated, unhydrogenated nitrogenous species (i.e., NO_3*, NO_2*) strengthen ΔG_{H^*}.

We hypothesize that stronger values of ΔG_{H^*} may direct Ni_2P/C's selectivity toward NH_3 even at negative reductive potentials (i.e., -0.6 V). At these potentials, despite a strong driving force toward HER, NO_x* intermediates could be strengthening the adsorption of H*, which inhibits the Tafel step of HER and promotes the hydrogenation of NO_x*. [137, 138] In general, the observed difference in ΔG_{H^*} due to co-adsorbed H* can be rationalized in terms of the electron-donating/withdrawing propensity and steric effects of the co-adsorbates, where in our system, the H* on a NNi_3-hollow site exhibits electrostatic repulsion effect on species such as NO_3^- and NO_2^-. [20, 139, 140] The impacts of H* and NO_x* on each other's surface energetics imply that the rates of NO_3^- electroreduction and HER are inherently dependent, corroborating our conclusions from the rate-order analysis that NO_x* and H* are co-adsorbing on Ni_2P/C's active site ensembles during NO_3^- electroreduction.

2.9 Comparison study with Ni nanocrystals

We hypothesize that monometallic nanocrystals are less able to co-adsorb different substrates due to the lack of active site ensembles and therefore, should be less selective toward producing NH_3 and prefer products such as NO_2^- and H_2. To that end, we compared the NO_3^- reduction behavior of Ni_2P and Ni nanocrystals.

2.9.1 Synthesis and preparation of catalyst

We prepared the Ni nanocrystals by combining $Ni(acac)_2$ (1 mmol) and oleic acid (1 mmol) and degassing in oleylamine (45.6 mmol) at 110 °C for 1 hour, reducing the temperature to 90 °C and injecting borane tertbutylamine (2.8 mmol) and subsequent heating for 1 hour. [141] The nanocrystals were deposited them on Vulcan Carbon (Ni/C) and tested them in identical conditions to our Ni_2P/C measurements (Fig. 2.10). Many Ni nanocrystal syntheses use trioctylphosphine (TOP) as a capping ligand to achieve small, monodisperse nanocrystals; however, we found that annealing TOP-capped Ni nanocrystals at high temperatures produced Ni_2P and had remarkably similar catalytic selectivity for NO_3^- electroreduction. (Fig. 2.C.4). [142, 143, 143] Therefore, we took care to choose a phosphorus-free synthesis to ensure no convoluting effects from trace phosphorus contamination (Fig. 2.11).

2.9.2 Selectivity and Outlook

Chronoamperometry reveals that although Ni/C is initially relatively inactive for NO_3^- electroreduction, the current increases dramatically overtime (Fig. 2.12a) as compared to the stable Ni_2P/C catalyst. This behavior is unique to nanoscale Ni; identical experiments with Ni foil yielded stable current over 1 hour (Fig. 2.C.3). Based on these results, we believe the increase in current is due to the transformation of the Ni nanocrystal surface to a more active species, such as a phosphate-containing Ni surface, that imitates Ni_2P/C. Post-catalysis P XPS of Ni/C electrodes shows that no phosphide formation (Fig. 2.D.4); however, we believe that a phosphate-species could be made *in situ* and cannot be distinguished from the phosphate-containing electrolyte signal. Previous reports have shown that phosphodized Ni electrocatalysts can be made by applying reductive potentials in aqueous solutions containing phosphate salts on timescales similar to our experiments, which

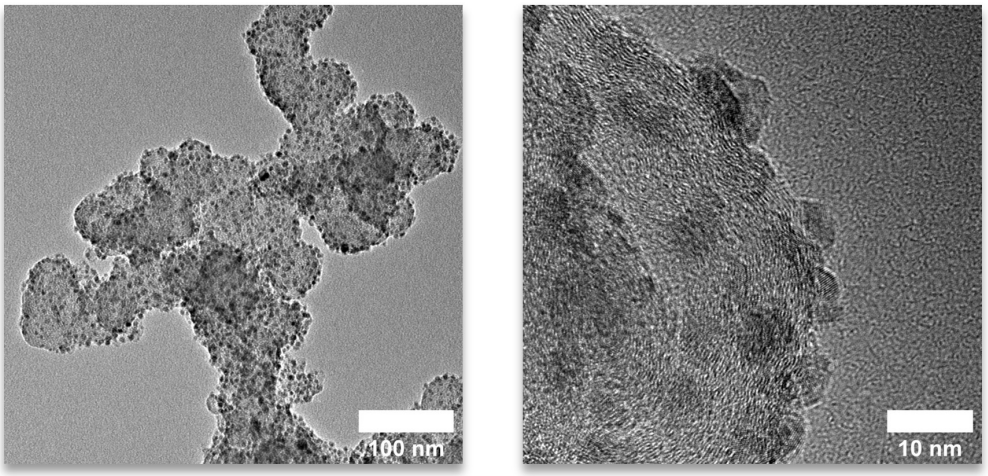

Figure 2.10: TEM of Ni/C showing Ni nanocrystals with 4.4 ± 0.9 nm diameter deposited on Vulcan carbon.

supports our hypothesis that phosphate may be interacting with the Ni nanocrystals. [144,145] Furthermore, Ni/C has a NH_3 Faradaic efficiency of $\sim$80% at -0.3 V vs. RHE (Fig. 2.12b), which is comparable to that of Ni_2P/C and contrary to previous reports of Ni's poor activity and selectivity for NO_3^- electroreduction. [125,128,131,146] We propose that this is more corroborating empirical evidence that a phosphorous-containing species being generated on the surface during the reaction.

While we were unable to verify our active site ensemble hypothesis by comparing Ni_2P/C and Ni/C, these results reinforce the importance considering the morphology of the material; most reports of Ni being a poor catalyst are on the micro- to macro-scale in size. Furthermore, phosphodized-Ni nanoscale catalysts may be of interest for future nitrate reduction studies in neutral conditions.

2.10 Conclusion

This work demonstrates Ni_2P/C's activity and selectivity for NO_3^- electroreduction at a range of potentials, where NO_3^- electroreduction FE ranges from 60% to nearly 100%, with selectivity for NH_3 maximized in the $H_2PO_4^-$-mediated region (> 0.25 V). DFT calculations and rate order analysis demonstrate Ni_2P/C's ability to co-adsorb nitrogenous and hydrogen intermediates and

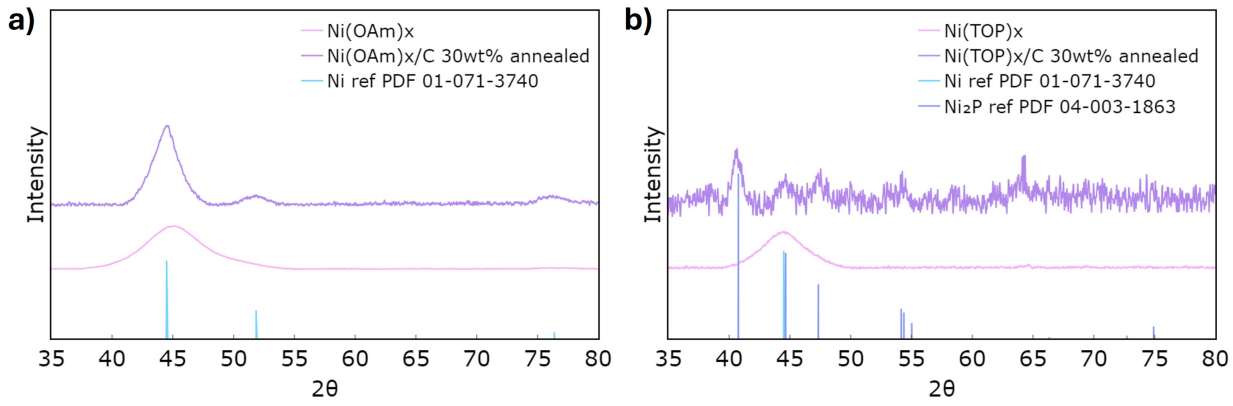

Figure 2.11: XRD spectra of a) Oleylamine-capped Ni nanocrystals (Ni(OAm)x) as synthesized and after annealing on the Vulcan carbon support and b) TOP-capped Ni nanocrystals (Ni(TOP)x) as synthesized and after annealing on the Vulcan carbon support.

selectively produce NH_3 over the range of potentials. We rationalize the potential-dependent selectivity of Ni_2P/C by changes in the surface coverage of adsorbates, where the ratio of H*:NO_x* at $-0.4\,V$ is ideal for performing NO_3^- electroreduction over HER. This work is a case study of the importance of active site ensembles on metal phosphide surfaces that drive nitrate reduction selectivity toward NH_3. This motivates future work in the electrocatalyst design of metal phosphides by tuning stoichiometry, doping, and morphology to dictate catalytic selectivity. We pursue this in Chapter 3.

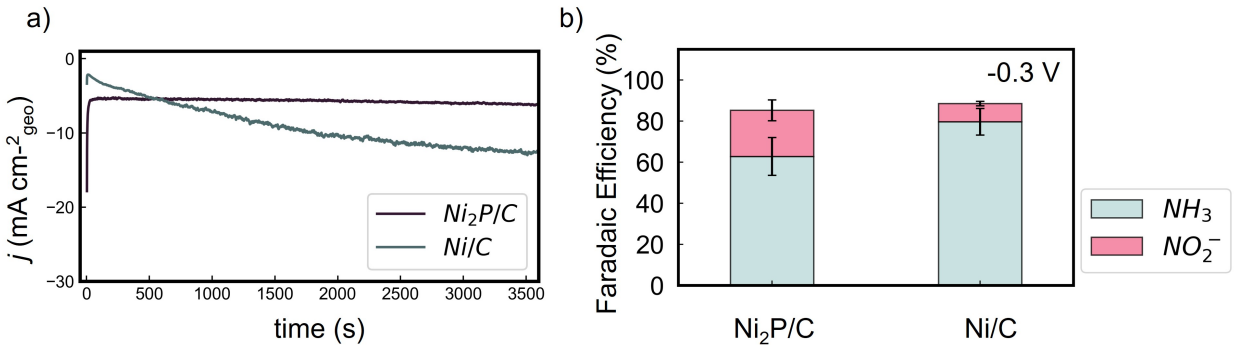

Figure 2.12: Comparison of a) chronoamperometry traces and b) selectivity of Ni_2P/C and Ni/C at $-0.3\,V$ vs. RHE

CHAPTER 2 APPENDIX

2.A Product quantification methods and data

All electrochemical measurements were performed in a separated H-cell from Pine Instruments, with a Nafion membrane separating the anodic and cathodic compartments (Fig. 2.A.1).

Faradaic efficiency is the ratio of charge passed for a certain product to the total charge passed for the reaction 2.8. c_{NH_3} is charge passed for NH_3] production, i is current, and t is the time. The total charge (c_{total}) is the integration of the chronoamperometry trace.

$$\text{FE } (\%) = \frac{c_{NH_3}}{c_{total}} = \frac{n \times [NH_3] \times V \times F}{i \times t} \times 100 \tag{2.8}$$

where V is the volume of electrolyte in the of the cathodic compartment, and n is the number of electrons required for the reaction (n = 2 for NO_2^-, n = 8 for NH_3).

2.A.1 Product quantification

Calibration curve and quantification of NH_3. NH_3 was quantified via the indophenol blue method using salicylic acid instead of phenol. [147] 100 mM $(NH_4)_2SO_4$ solution was prepared with 0.1 M phosphate buffer solution and $(NH_4)_2SO_4$. 5 mM $(NH_4)_2SO_4$ solution was prepared by mixing 0.5 mL of 100 mM $(NH_4)_2SO_4$ solution with 9.5 mL of 0.1 M phosphate buffer. 2500, 1250, 625, 312.5, 156.25 μM of $(NH_4)_2SO_4$ solutions were prepared by sequential dilution with 0.1 M phosphate buffer. A 0 μM of $(NH_4)_2SO_4$ solution was also prepared (100 μL). The reference solutions were diluted 10 times with Millipore water by taking 100 μL of original solution and adding 900 μL of Millipore water. After dilution, the concentration of reference solutions were as followed: 250, 125, 62.5, 31.25, 15.625 μM of $(NH_4)_2SO_4$ with 20 μM of potassium phosphate. The actual concentration of NH_3 should be doubled: 500, 250, 125, 62.5, 31.25, 0 μM.

To each tube, 1000 μL 1 M NaOH solution was added (1000 μL reference solution: 1000 μL 1 M NaOH. The tubes were shaken vigorously. 500 μL of coloring agent, 50 μL of 0.034 M sodium nitroprusside dihydrate (Sigma-Aldrich, $\geq$ 99%), and 50 μL of NaClO solution (4.00-4.99% chlorine,

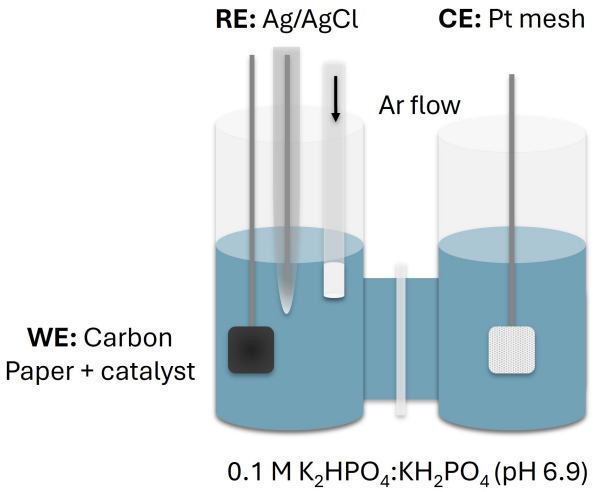

Figure 2.A.1: H-cell set up.

Sigma-Aldrich, reagent grade) were swirled to ensure a homogeneous mixture, and then added to the 15 mL centrifugation tube sequentially. The coloring agent was prepared by dissolving 3.6 mmol of salicylic acid (Sigma-Aldrich, $\geq$ 99.0%) and 1.8 mmol of potassium sodium tartrate tetrahydrate (Sigma Aldrich, 99%) in 3.6 mL of 1 M NaOH solution and diluted it to 10 mL with Millipore water. For product quantification, the electrolyte was diluted to an appropriate concentration within the calibration curve range with 0.1 M phosphate buffer. To that, the same amounts of NaOH, coloring agent, sodium nitroprusside, and NaClO were added. UV-visible spectrometry was used to measure the absorption of the colored complex at 660 nm to construct the calibration curve and calculate the concentration of NH_3 in an electrolyte.

Calibration curve and quantification of NO_2^-. NO_2^- was quantified via the Griess method, as reported by previous studies. [148] 0.2% N-(1-naphthyl)ethylenediamine dihydrochloride solution was prepared by dissolving 0.1 g of N-(1-naphthyl)ethylenediamine dihydrochloride (Merck, ACS grade) in 50 mL of Millipore water. The 2% sulfanilamide solution was prepared by dissolving 1 g of sulfonamide (Sigma-Aldrich, 98%) and 2.94 g of H3PO4 in 50 mL of Millipore water.

1 mmol of KNO_2 (85.1 mg) was dissolved in 10 mL of 100 mM phosphate buffer solution. 1 mM KNO_2 solution was prepared by mixing 0.1 mL of 100 mM KNO_2 solution with 9.9 mL of 0.1 M phosphate buffer. 500, 250, 125, 62.5, 31.25, 0 μM of KNO_2 solutions were prepared by sequential

dilution with 0.1 M phosphate buffer. 500 μL reference solution and 500 μL Millipore water were added to a 15 mL centrifugation tube. The tube was shaken vigorously. 1 mL of 2% sulfanilamide solution was added, and the tube was incubated for 5 min at RT, protected from light. Then 1 mL of 0.2% N-(1-naphthyl)ethylenediamine dihydrochloride solution was added, and the tube was further incubated for 10 min at RT, protected from light. The final concentrations are 500, 250, 125, 62.5, 31.25, 0 μM before any dilution by water.

For product quantification, the electrolyte was diluted to an appropriate concentration within the calibration curve range with 0.1 M phosphate buffer. To that, the same amounts of sulfanilamide solution and N-(1-naphthyl)ethylenediamine dihydrochloride solution were added. UV-visible spectroscopy was used to measure the absorption of the colored complex at 540 nm to construct the calibration curve and calculate the concentration of NO_2^- in an electrolyte.

2.A.2 Data

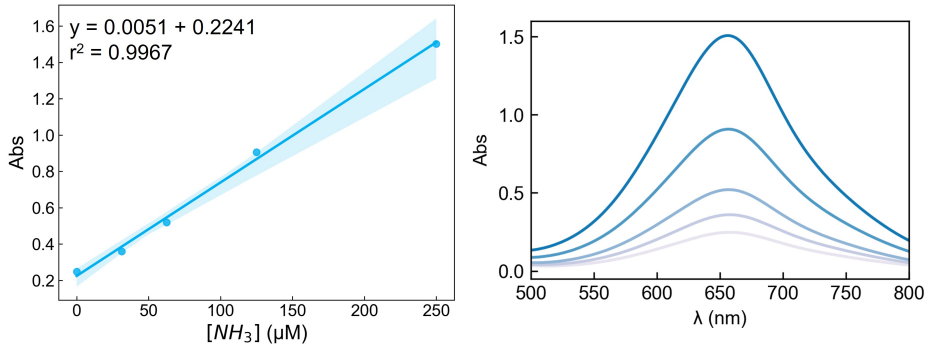

Figure 2.A.2: NH_3 calibration curve and corresponding UV-visible absorption spectra.

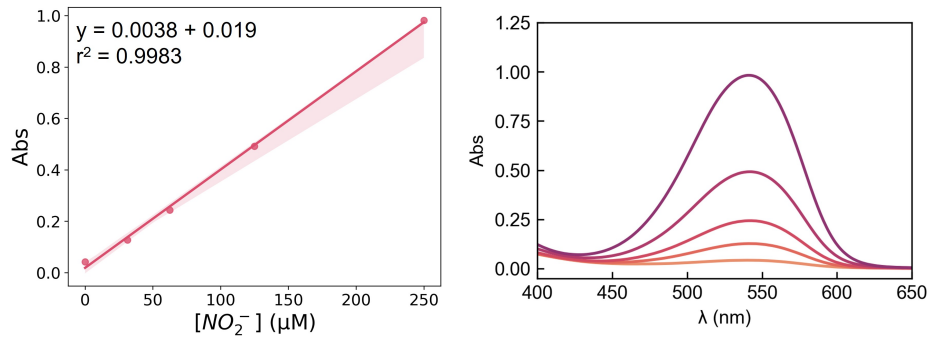

Figure 2.A.3: NO_2^- calibration curve and corresponding UV-visible absorption spectra.

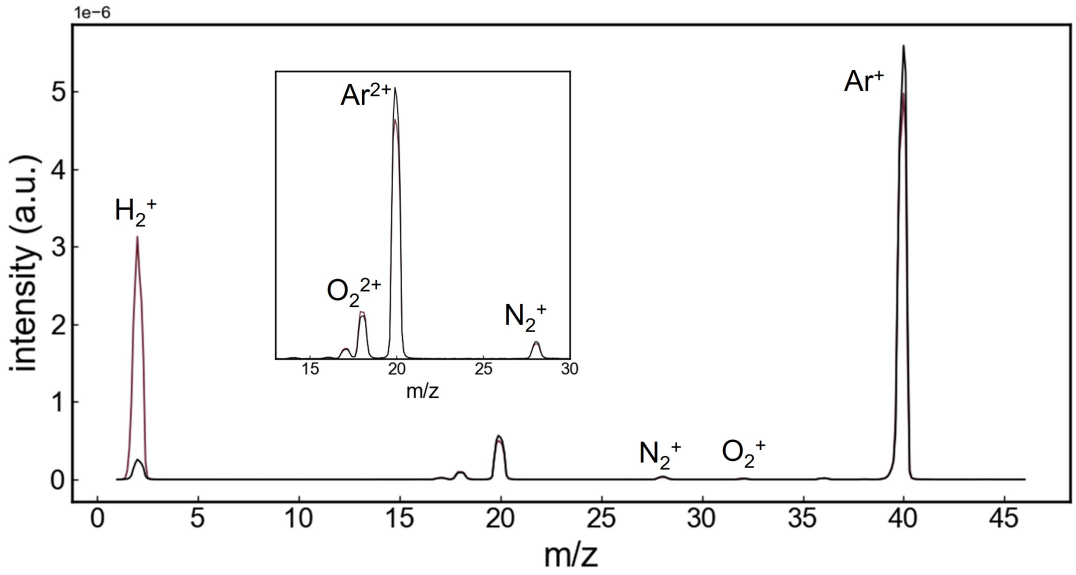

Figure 2.A.4: Mass spectrometry measurements taken after 1 hour of bulk electrolysis at −0.6 V vs. RHE (purple trace). Significant increase in the H_2 signal and no change in the N_2 signal from the background indicates H_2 production and negligible N_2 production. The increase in O_2 signal is due to OER at the counter electrode.

2.B Rate order discussion

Fig. 2.6b is a plot of the rate order vs. potential (i.e., the slopes of the log(i) vs log([KNO3] plots at a range of potentials) under the assumption that 100% of the current is toward NO_3^-

electroreduction. We acknowledge that is not the case and that HER is a competing side reaction. Therefore, we correct for this to the best of our ability and demonstrate a similar quantitative trend in 2.B.1b to the one observed in 2.6. The datapoints in 2.B.1b are the slopes of log(i) vs log([KNO3] plots (such as the ones in Fig. 2.B.1a), where the current at 100 mM KNO_3 (labeled in orange) is multiplied by the total FE of the NO_3^- electroreduction products measured at that potential (Fig. 2.6c). For example, at -0.1 V vs. RHE, the total FE toward NH_3 and NO_2^- is 83.6%. The i measured at this potential is multiplied by a factor of 0.836 to isolate $i_{NO_3^- \, reduction}$ and the NO_3^- rate order. This analysis was propagated at all the potentials where products were quantified (-0.1 V to -0.6 V vs. RHE).

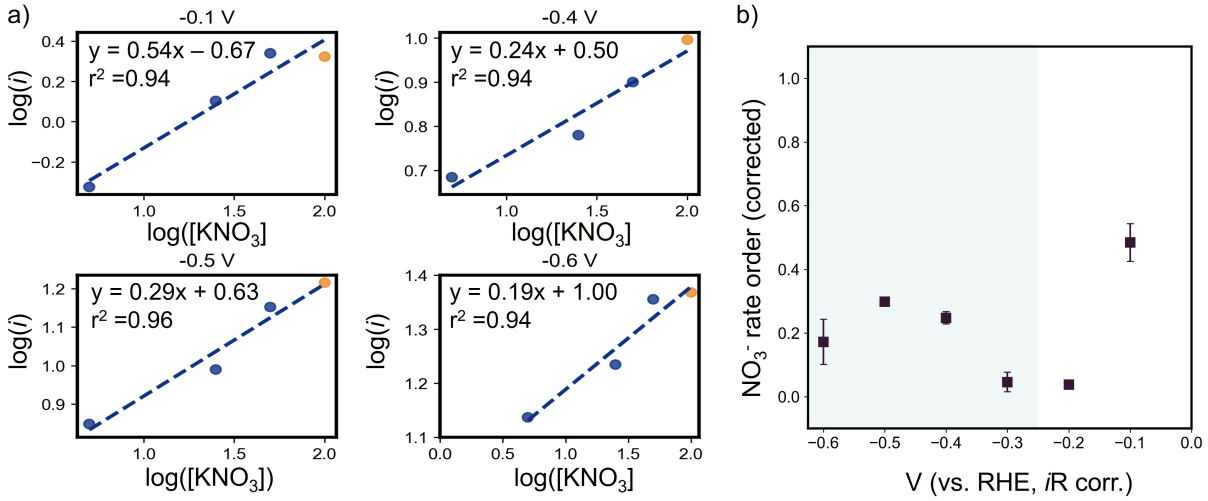

Figure 2.B.1: a) Sample log(i) vs. log([KNO_3] plots at a range of potentials. The 100 mM datapoint is corrected to only account for $i_{NO_3^- \, reduction}$ (orange), which was identified by product quantification from bulk electrolysis experiments b) Corresponding rate order plot only with voltages where $i_{NO_3^- \, reduction}$ is corrected.

2.C Electrocatalysis data

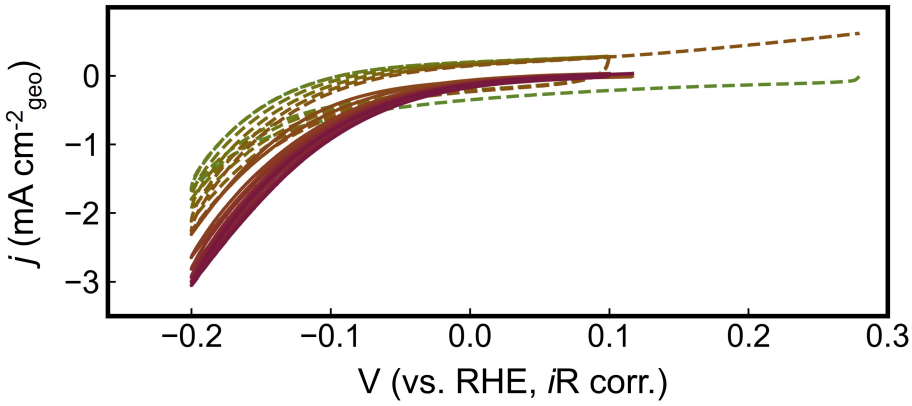

Figure 2.C.1: Activation of Ni_2P/C prior to chronoamperometry by taking CV from −0.1 V to −0.2 V vs. RHE at 50 mV/s (6x) and 5 mV/s (6x). Dashed lines indicate scans at 50 mV/s, solid lines indicate scans at 5 mV/s. Activation was performed for every electrode until the CV trace stabilized.

Material	**Total charge passed (c)**
Carbon Fiber (CF)	-0.05
Carbon Fiber (CF) + Vulcan carbon (VC)	-0.38
Ni_3P/C	-21.1

Table 2.C.1: Charge passed at −0.3 V vs. RHE. Negligible product formation without catalyst observed at this potential.

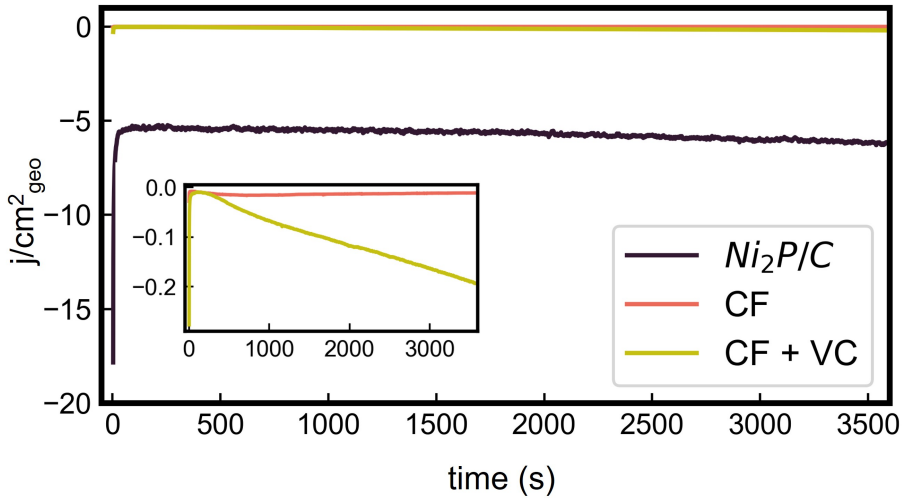

Figure 2.C.2: Chronoamperometry at −0.3 V vs. RHE with Ni_2P/C, a carbon fiber electrode with no catalyst, and a carbon fiber electrode with vulcan carbon but no catalyst.

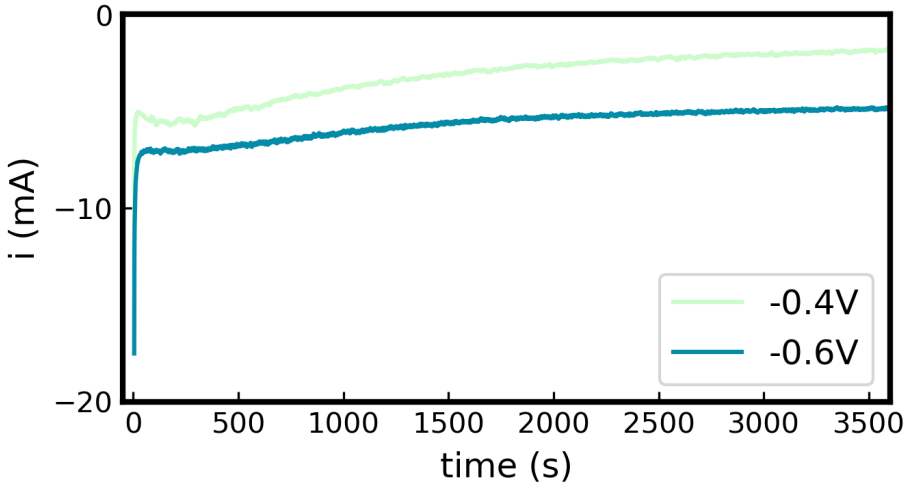

Figure 2.C.3: Chronoamperometry at −0.4 V and −0.6 V vs. RHE with nickel foil as a working electrode.

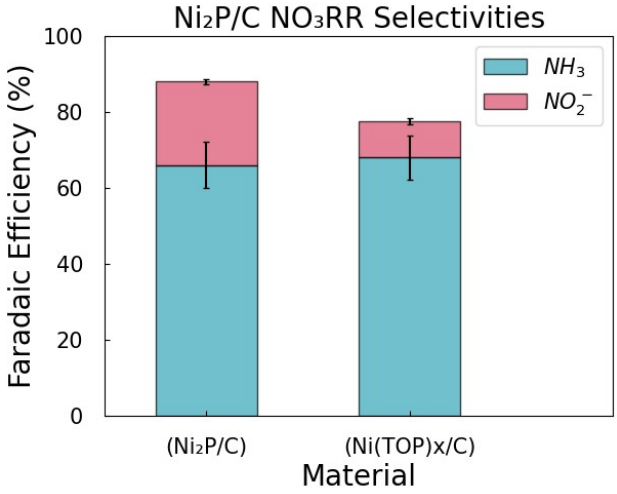

Figure 2.C.4: Selectivity comparison at $-0.3\,\mathrm{V}$ vs. RHE between Ni_2P made bottom up (Ni_2P/C) and via annealing TOP-capped Ni nanoparticles ($Ni(TOP)_x$/C).

2.D Catalyst characterization

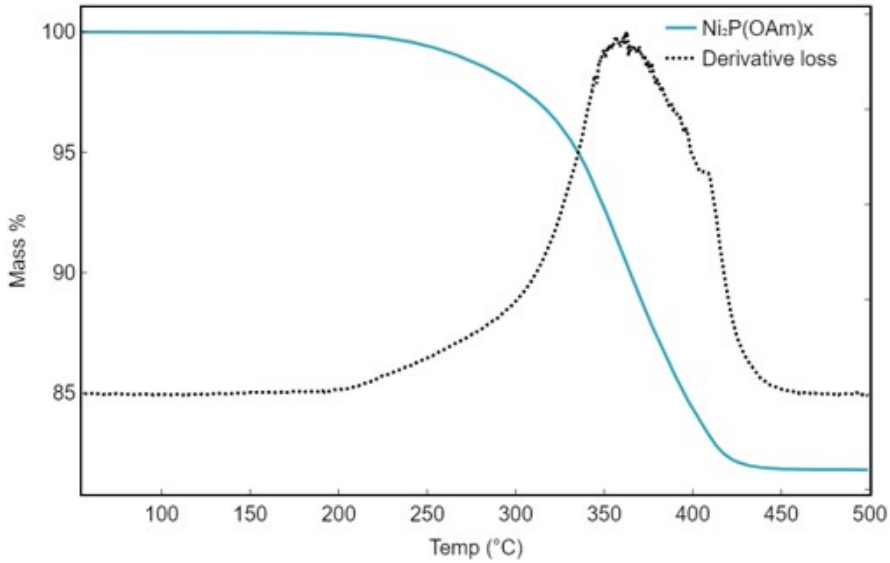

Figure 2.D.1: TGA data of Ni_2P nanocrystals, showing 81% wt. % Ni_2P after ligand loss

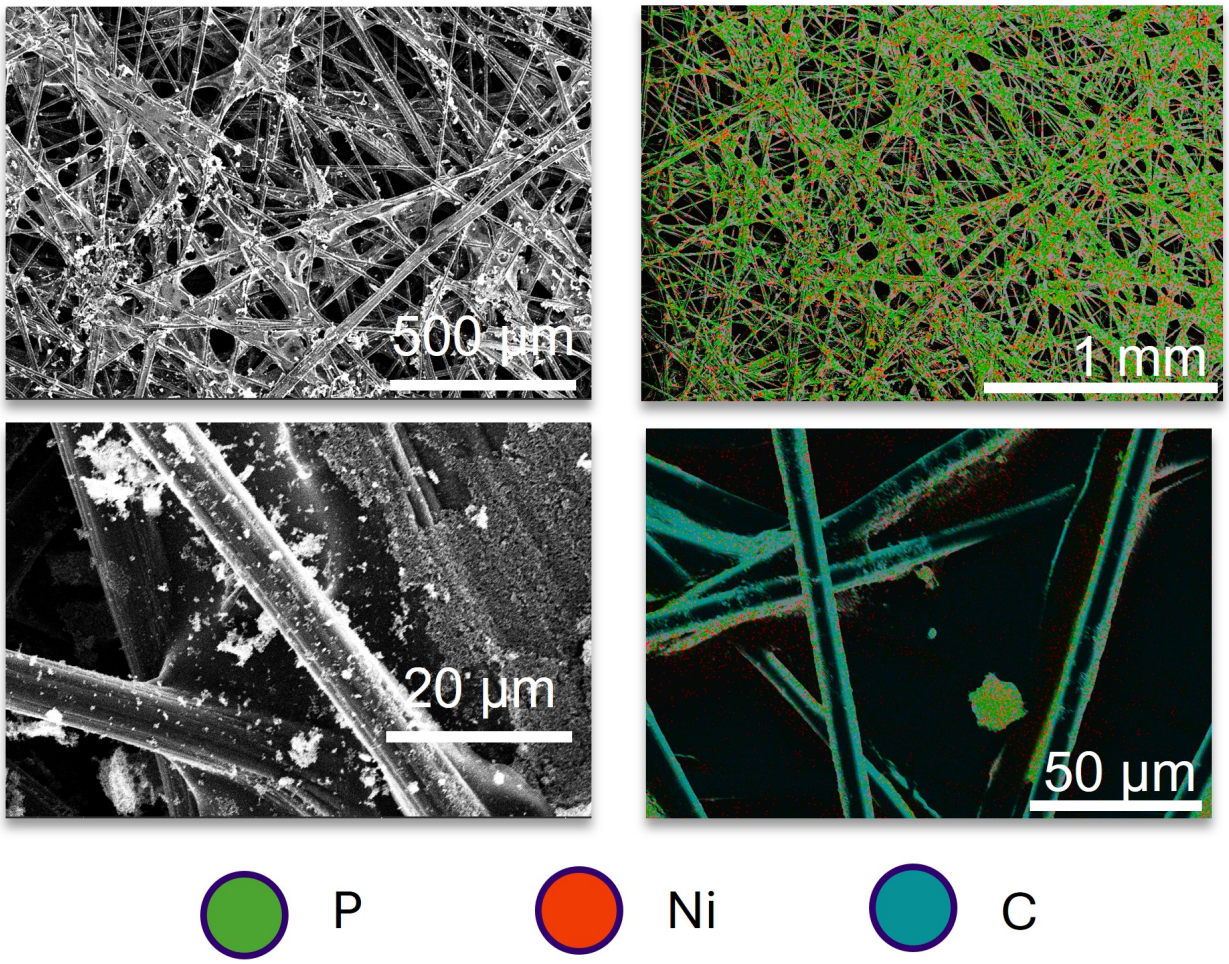

Figure 2.D.2: SEM/EDS of Ni_2P electrode. Green indicates phosphorus, red indicates Ni. The long, web-like structure is the carbon paper electrode and the dispersed white powder-like features is Vulcan carbon with deposited Ni_2P nanocrystals.

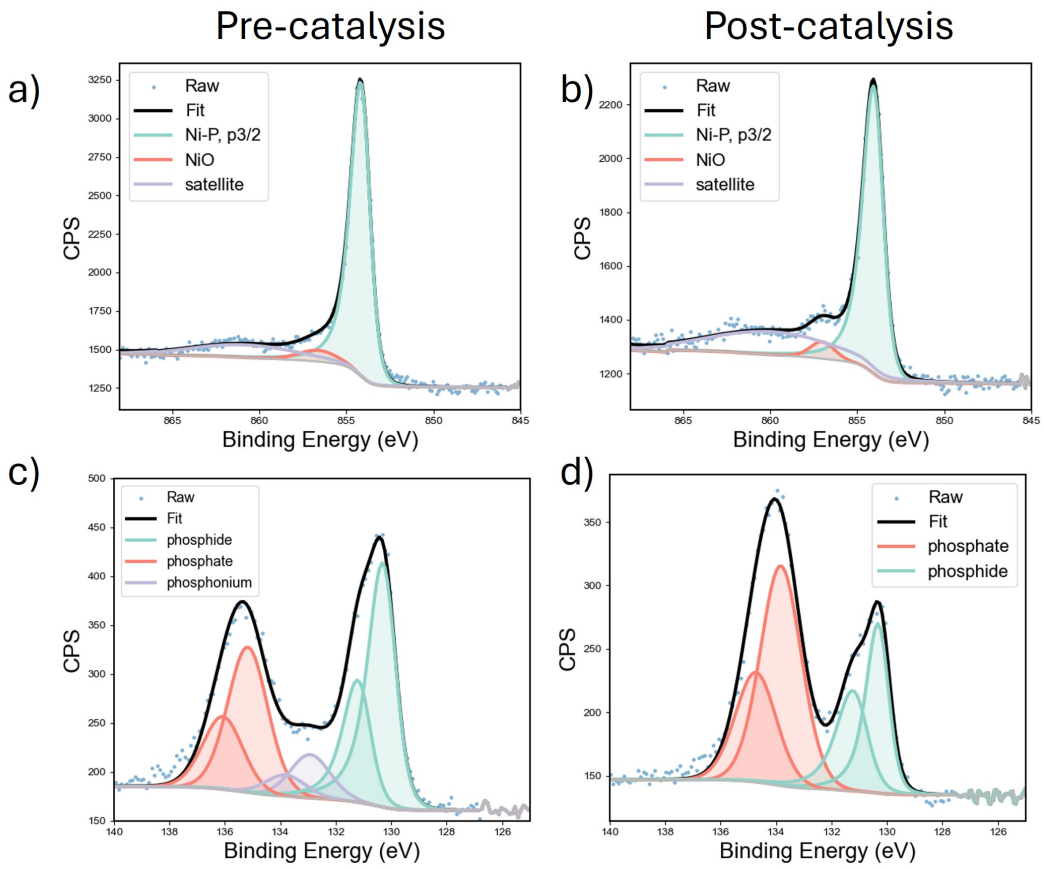

Figure 2.D.3: Ni $2p_{3/2}$ (a, b) and P 2p (c, d) XPS spectra of Ni_2P/C on carbon fiber, pre and post catalysis. Phosphonium signal is present from the original synthesis, which is a known by-product in the procedure. [1] The change in the phosphate and phosphide peak ratio is attributed mainly to leftover electrolyte (KH_2PO_4/K_2HPO_4) on the electrode that could not be washed off easily.

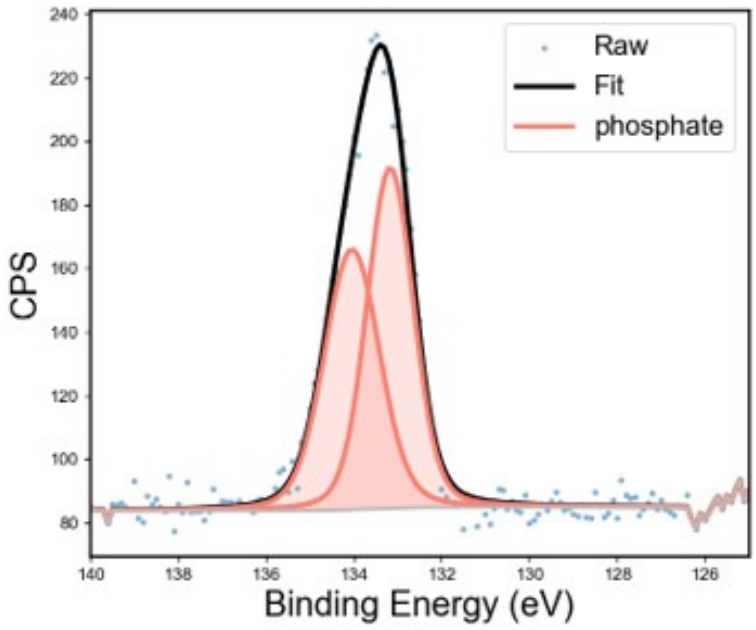

Figure 2.D.4: XPS spectra showing the P 2p signal of Ni/C electrodes post NO_3^- electroreduction.

Chapter 3

SYNTHESIS OF DOPED Ni_2P NANOCRYSTALS TO MODULATE NO_3^- ELECTROREDUCTION SELECTIVITY

This chapter is being prepared for publication, with contributions from Emily Nishiwaki, Emily Miura-Stempel, Quinn Brouhle, Reed Worland, and Brandi Cossairt.

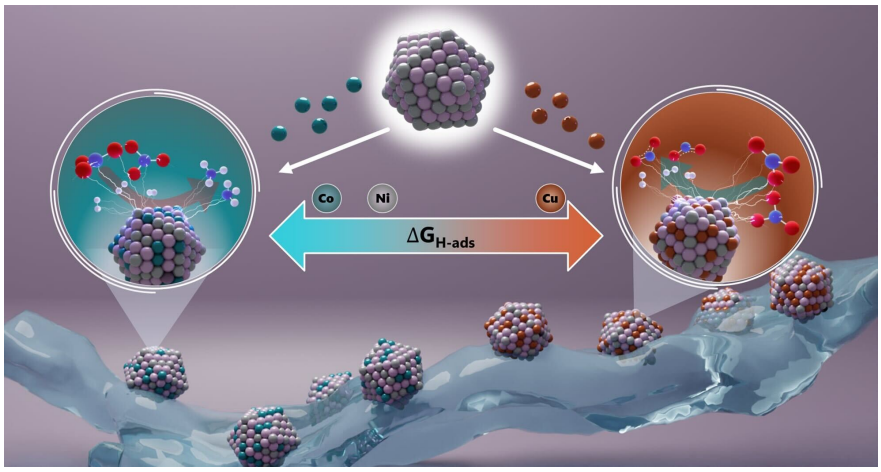

Figure 3.1: Post-synthetic doping of Ni_2P nanocrystals can be utilized to systematically modulate NO_3^- electroreduction behavior

3.1 Introduction: Continuing the metal phosphide journey

As discussed in the previous chapter, Ni_2P catalyzes NO_3^- electroreduction across a series of potentials with high ammonia selectivity due to its surface active site ensembles. This study is in agreement with the extensive literature of Ni_2P's active catalytic ability for a variety of reactions such as HER, [71] CO_2 electroreduction, [87, 99] and high NH_3 selectivity over NO_2^- and H_2 at low cathodic potentials. [105, 125]

As synthetic chemists, this made us consider how we could use synthetic levers to augment

Ni_2P's eletrocatalytic abilities. This led us to study how we can synthetically modify Ni_2P's active site ensembles through transition metal doping to tune electrocatalytic behavior by altering surface energetics, adsorbate coverage, and ultimately reactivity and selectivity. [149] Doping metal phosphide electrocatalysts to achieve desired selectivity and enhanced activity has been demonstrated extensively for the hydrogen and oxygen evolution reactions [150–152], as well as for NO_3^- electroreduction. [153, 154]

3.2 d-band theory

To fundamentally understand how doping impacts a catalyst surface, we must consider the electronic structure, or more precisely, the density of states of the catalyst upon the adsorption of a substrate. d-band theory was proposed by Hammer and Nørskov two decades ago, but it is still used heavily to explain activity trends in heterogeneous electro(catalytic) reactions. Here, we explain briefly the concepts of d-band theory and how it informs catalyst design. [155]

Prior to bonding, a transition metal's d band is a narrow distribution around the Fermi level. However, once a substrate chemisorbs to a transition metal surface, the d band splits into bonding and antibonding states. The relative energies of the destabilized, antibonding states with respect to the Fermi level will dictate the strength of the adsorbate bond. Hammer and Nørskov calculated the chemisorption energy trends of several transition metals (Cu, Ag, Au, Ni, Pd, Pt, and Ru) prior to and post chemisorption to oxygen. They determined that there are periodic trends in the bond strengths of O to a transition metal surface and that the bands themselves can be characterized by the center of the band, ϵ_d. As we move left in the periodic table toward transition metals such as nickel, palladium (and cobalt), the antibonding adsorbate-metal d states reside above the Fermi level and are therefore empty. The opposite is true for the noble metals (Cu, Ag, Au), whose antibonding states are below the Fermi level and filled, which explains the strong adsorption of nickel and cobalt and the weak adsorption capabilities of copper. ϵ_d trends linearly with O chemisorption energy and is expected to be applicable to all simple atomic adsorbates (H, C, N, etc.). Ultimately, their work demonstrates how the electronic structure directly correlates with adsorbate binding energy.

Hammer and Nørskov's seminal work has been pivotal in the strategic design of catalysts in the 21st century. Today, there is work that builds upon their model with complex materials, reaction

conditions, and even extends their model with machine learning to predict the d-band center of bimetallic compounds. [156–160] In this study, we use d-band theory to inform our choice of dopant into Ni_2P: copper, which binds H weakly, and cobalt, which binds H strongly. Previous work by Downes et al. doped Ni_2P with various different transition metals, including copper and cobalt, and found that HER activity followed a volcanic relation and was tuned by the dopant cation's ΔG_{H^*}. [108] Cobalt and copper resided at opposite ends of their volcano, which motivated the use of these transition metals in our study to see the most overt modulations in reaction selectivity due to differences in ΔG_{H^*}.

3.3 Post-synthetic cation exchange

To synthsize doped Ni_2P nanocrystals, we used a post-synthetic cation exchange method, which replaces cations in a host nanocrystal while preserving the anion sublattice. In bulk solids, cation exchange reactions typically have high activation energies and unfavorable thermodynamics. In contrast, cation exchange with nanomaterials operates with more facile, molecule-like reaction kinetics. Furthermore, due to their low-coordinated, defect-rich, and strained surfaces that have high-energy sites for ion exchange reactions, nanomaterials are ideal platforms to test the boundaries of this method to synthesize target materials. However, the process is not as simple as it sounds; there are many factors at play, such as the thermodynamics of the bonds in the nanocrystal lattice and the kinetics barriers of cation incorporation. [161–163]

More specifically, cation exchange has been thoroughly studied with colloidal quantum dot systems to achieve desired morphologies and crystal structures that are not accessible via conventional synthetic methods, [164–166]. Cation exchange has also been used for the rational design of electrocatalysts and is a method to achieve a desired electronic structure for a certain electrocatalyst. [161] There are a few examples of syntheses of doped TMPs that use a two-step synthesis to perform cation exchange. In these methods, a dopant metal precursor is added to a pre-formed, amorphous metal phosphide nanocrystal and subsequently heated to a higher temperature ($> 300\ ^\circ C$). Aghabozorgi, Brock, and coworkers synthesized managnese-doped nickel, cobalt, and iron phosphides as electrocatalysts for the oxygen evolution reaction with this method and achieved up to 75% manganese incorporation with nickel phosphide while maintaining the morphology of the original host Ni_2P nanocrystals. [152] Downes et al. doped Ni_2P with Co, Cu, Rh, Ru, Pd, and

Mo and found that HER selectivity could be systematically tuned based on the secondary cation present. [108]

Generally, post-synthetic cation exchange with nanocrystals is a topotactic transformation, where the overall morphology of the nanocrystal can be retained and only the cationic composition is modified. With this knowledge and the proven challenges of synthesizing doped metal phosphide nanocrystals bottom-up, [167] we decided to utilize cation exchange with the same Ni_2P nanocrystals as our host material from our previous work, which were already in the "amorphous" state as reported by the two-step syntheses discussed above. Furthermore, this allows us to make direct comparisons with the mechanism and reaction selectivity observed with that system.

In this study, we synthesized $Ni_{2-x}M_xP$ (M = Cu, Co) nanocrystals, where copper and cobalt were chosen as dopants that would significantly impact the ΔG_{H^*} based on previous literature calculations and d-band theory. [155, 160] We then conducted NO_3^- electroreduction with the doped Ni_2P nanocrystals and observed enhanced NH_3 selectivity with higher cobalt concentrations and conversely, lower NH_3 and higher H_2 selectivity at with higher copper concentrations, which is in agreement with what we would expect based on d-band theory.

3.4 Nanocrystal synthesis

Further information about synthetic procedures can be found in the Supplemental Information. Ni_2P nanocrystals were synthesized according to previous methods in our group using a one pot heat-up synthesis. [1, 20] Briefly, $NiCl_2$ (1 equiv.) and oleylamine (21 equiv.) were degassed at 120 °C and subsequently the reaction mixture was lowered to 50 °C. Tris(diethylamino)phosphine was injected (4 equiv.), and the temperature was raised to 250 °C for 1 hour. The resulting nanocrystals were purified in a glove box using centrifugation: the crude reaction mixture with isopropyl alcohol (1x), the reaction mixture dissolved in minimal amounts of pentane with isopropyl alcohol (3x), and then a final spin with the reaction mixture dissolved in minimal amounts of toluene with acetonitrile (1x). Powder X-ray diffraction (XRD) and Transmission electron microscopy (TEM) images reveal phase-pure Ni_2P nanocrystals with an average size of 4.3 ± 0.6 nm.

Previous work in our group and others has demonstrated Ni_2P nanocrystal formation at 250 °C, with crystallinity increasing at temperatures above 300 °C. [168] Doped Ni_2P can be synthesized

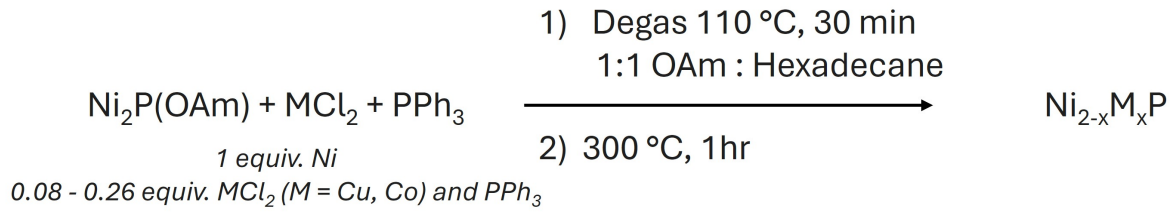

Figure 3.2: Synthesis of doped Ni_2P nanocrystals (OAm = oleylamine). More detailed information about molar ratios can be found in the Supplementary Information.

bottom up via a metal co-reduction at temperatures <250 °C and subsequent phosphidation at temperatures above 300 °C. [152, 167, 169] With this knowledge, we synthesized our nanocrystals with a two-step, cation exchange procedure with minor modifications from literature (Scheme 3.2). [108] We took our purified, oleylamine-capped Ni_2P nanocrystals (Ni_2P(OAm)), MCl_2 (M = Cu, Co), and triphenylphosphine and redispersed them in a 1:1 mixture of oleylamine and hexadecane (see Tables 3.A.1 and 3.A.2 for molar quantities). After degassing at 110 °C, the temperature was ramped rapidly to 300 °C and held for 1 hour. The particles were purified via centrifugaion in a glove box by splitting the crude reaction mixture between two falcon tubes and adding $\sim$30 mL of isopropyl alcohol to each and centrifuging them for 10 minutes at 7830 rpm. The sample was then dissolved in a minimal amount of pentane and 30 mL of ethyl acetate (1x) and then again with pentane/isopropyl alcohol (2x), each spin being for 10 minutes at 7830 rpm.

3.5 Nanocrystal characterization

Elemental analysis was carried out with ICP-OES, which demonstrated the successful incorporation of copper (8% and 15%) and cobalt (16% and 26%) into the Ni_2P nanocrystals (Tables 3.A.2. 3.A.1). XRD data for cobalt-doped-Ni_2P shows the formation of the known Ni_xCo_yP hexagonal material, while copper-doped Ni_2P XRD data demonstrate retention of the Ni_2P hexagonal lattice (Fig. 3.3a, 3.3b).

By Scherrer analysis and TEM images, while there are minimal changes to the cobalt-doped

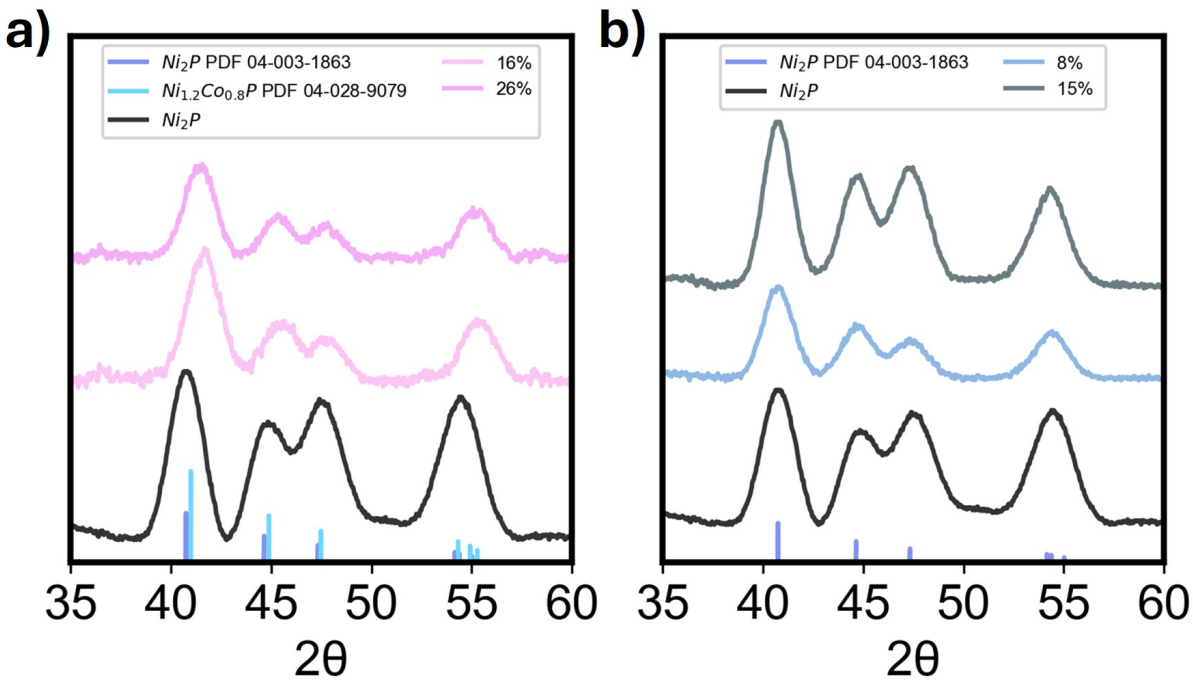

Figure 3.3: XRD data of a) cobalt-doped and b) copper-doped Ni_2P nanocrystals.

particle morpology post-cation exchange, copper-doped incorporation, particularly at higher concentrations, results in rod-like structures (Fig. 3.4, Fig. 3.5. This was unexpected; previous doping experiments with copper and Ni_2P nanocrystals showed little change in particle size and morphology (Fig. 3.C.2, 3.C.1).

We hypothesize that the quality of the starting Ni_2P nanocrystal batch is important. The cobalt-doped Ni_2P nanocrystals shown in Fig. 3.4 and previous copper-doping experiments shown in Fig. 3.C.2 were synthesized from the same batch of Ni_2P nanocrystals. However, the copper-doped Ni_2P nanocrystals shown in Fig. 3.5 were synthesized from a different batch of Ni_2P nanocrystals, which may have had poorer crystallinity or more polydisperse and caused a change in morphology. While we do not have direct evidence of the differences between the two starting Ni_2P nanocrystal batches, we recall that the purification process was much more difficult in more recent synthetic batches and hypothesize that this could be related to the quality of the nanocrystals despite the

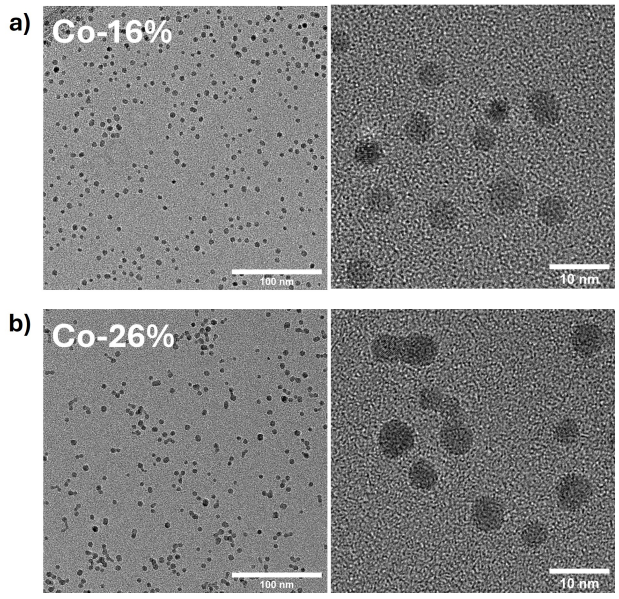

Figure 3.4: TEM images of cobalt-doped Ni_2P nanocrystals.

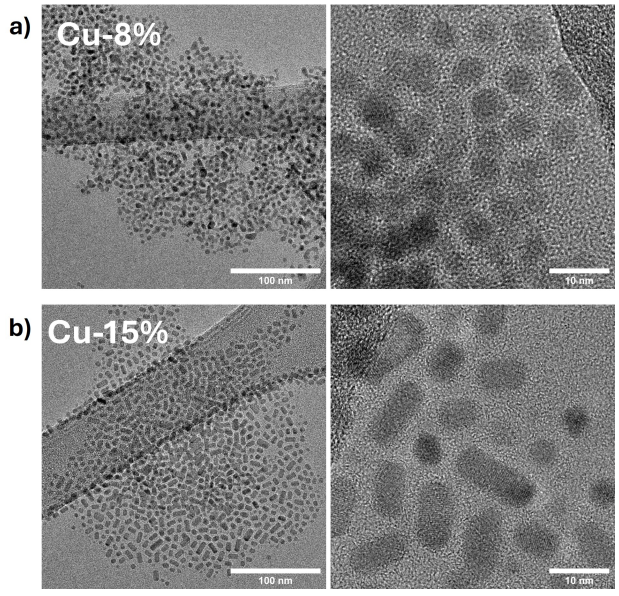

Figure 3.5: TEM images of copper-doped Ni_2P nanocrystals.

synthetic procedures being identical.

We also note that for the synthesis of the spherical cobalt-doped Ni_2P and copper-doped Ni_2P, we used a 1:1 ratio of oleylamine to 1-octadecene (instead of hexadecane), but the copper-doped particles that ended up with some rod-like morphologies used a 1:1 ratio of oleylamine to hexadecane. Hexadecane was used because it was easier to work up (1-octadecene polymerizes at temperatures near 300 °C and makes it difficult to remove), and we doubted that there would be a large impact on the reaction due to it being a simple, aliphatic molecule. However, future work should take care to use an appropriate a consistent solvent mixture. That being said, we hypothesize that it is more probable that the quality of the starting Ni_2P batch (i.e., crystallinity, morphology) affects the doped nanocrystal morphology, but solvent could also play a role.

In the future to ensure the yield similar particle morphologies, the same batch of starting nanocrystals should be used for all experiments. However, since the goal of this study was to evaluate the NO_3^- electroreduction behavior of these materials, we deposited the spherical cobalt-doped Ni_2P and polydisperse copper-doped Ni_2P on Vulcan carbon and after annealing, observed similar particle size and morphology. Therefore, we proceeded and used these materials to study the impacts of doping Ni_2P on NO_3^- electroreduction selectivity, ensuring that there was identical loading between these doped materials to make an accurate comparison between the reaction selectivities.

3.5.1 A brief aside: pushing the limits of cation exchange with Ni_2P nanocrystals

Given that previous doping reactions occurred with an approximate 1:1 substitution of Ni:Cu/Co, we were interested in seeing the limits of this post-synthetic cationic exchange method with Ni_2P, we added higher concentrations of MCl_2 precursors. To draw a clear comparison between the reaction selectivities of 26%-doped copper and cobalt Ni_2P, we added 0.26 equiv. of $CuCl_2$ with respect to nickel. However, elemental analysis revealed 36% doping into Ni_2P, which we attribute to a copper-rich particle (Table 3.A.1). Our proposal of a copper-rich surface is supported by the $\sim$1 nm growth in particle diameter. Furthermore, after analysis of the XRD data, the asymmetric peaks that begin to form are likely due to the formation of a hexagonal Cu_3P phase on the surface, which is supported by characterization after the materials have been annealed at 450 °C under 95:5 N_2:H_2. Post annealing, a clear hexagonal Cu_3P phase is present with the 36%-doped copper-doped

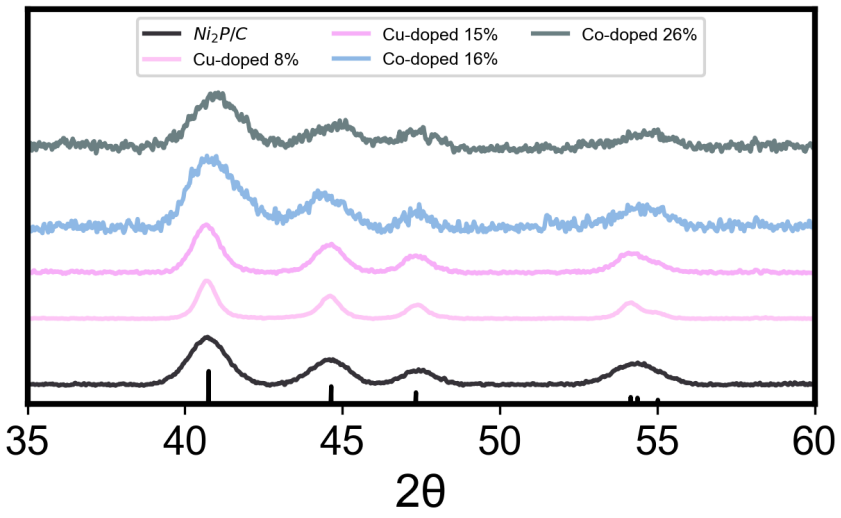

Figure 3.6: XRD data of copper and cobalt-doped Ni_2P catalyst inks.

Ni_2P/C (Fig. 3.C.4a). Copper's inability to incorporate as well as cobalt was unexpected; based on the relative atomic radii of the three metals (Ni $\approx$ Cu $<$ Co) we expected higher amounts of copper to incorporate into Ni_2P via cation exchange. However, the stable bimetallic hexagonal nickel cobalt phosphide phase and Co_2P have similar lattice parameters to that of Ni_2P's (a = 5.86, c = 3.37) with same symmetry ($\overline{P}62m$) while Cu_3P, has much larger lattice parameters (a = 6.95, c = 7.12) and different symmetry ($P6_3cm$). We hypothesize that upon incorporation of 0.26 equiv. of $CuCl_2$, it is preferential to form Cu_3P over cation exchange with nickel.

Similarly, after adding 0.84 equiv. of cobalt with respect to nickel), we were only able to obtain a slightly higher doping percentage (31%). This indicates that 31% doping is toward the upper limit of the amount of cobalt we can put onto these Ni_2P nanocrystals. Furthermore, Scherrer analysis reveals $\sim$1 nm of particle growth in 31% cobalt-doped Ni_2P, indicating that cobalt is unable to diffuse completely into the Ni_2P lattice and remains at the surface, or cannot incorporate at all at these concentrations (Fig. 3.C.4b, Table 3.C.1).

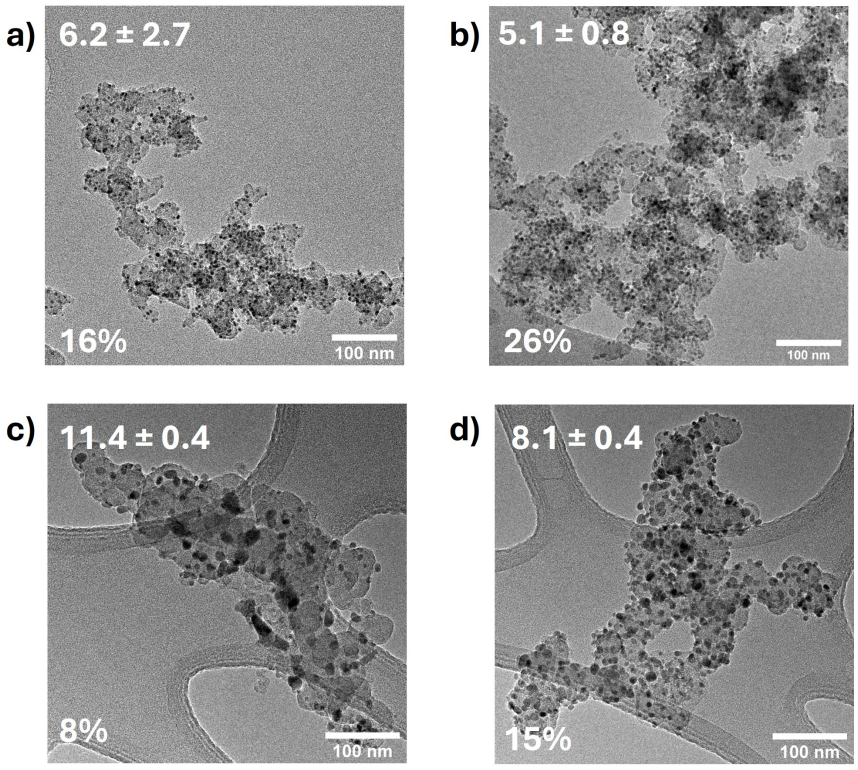

Figure 3.7: TEM images of the doped catalyst inks: a) NiCoP-16/C b) NiCoP-26/C c) NiCuP-8/C and d) NiCuP-15/C. Nanocrystal diameters are given in nm.

3.6 Doped catalyst ink preparation

We prepared our catalyst inks by depositing the doped nanocrystals onto Vulcan carbon and annealing them at 450 °C under 95:5 N_2:H_2 for 30 minutes. XRD data of the catalyst inks demonstrates the retention of the Ni_2P hexagonal crystal structure with only slight particle growth (Fig. 3.7, 3.6, Table 3.C.2). We also used X-ray photoelectron spectroscopy (XPS) to investigate the dopant incorporation post-annealing at high temperatures (Fig. 3.8. XPS data of the 8% copper-doped Ni_2P catalyst ink (NiCuP-8/C) reveals a single Cu $2p_{3/2}$ peak corresponding to Cu^0, which we attribute to complete copper incorporation into the Ni_2P lattice. With the higher 15% copper-doped Ni_2P catalyst ink (NiCuP-15/C), a feature corresponding to Cu^{2+} is also present, which we attribute to surface copper being more prone to oxidation, especially since the ligands were removed due to the

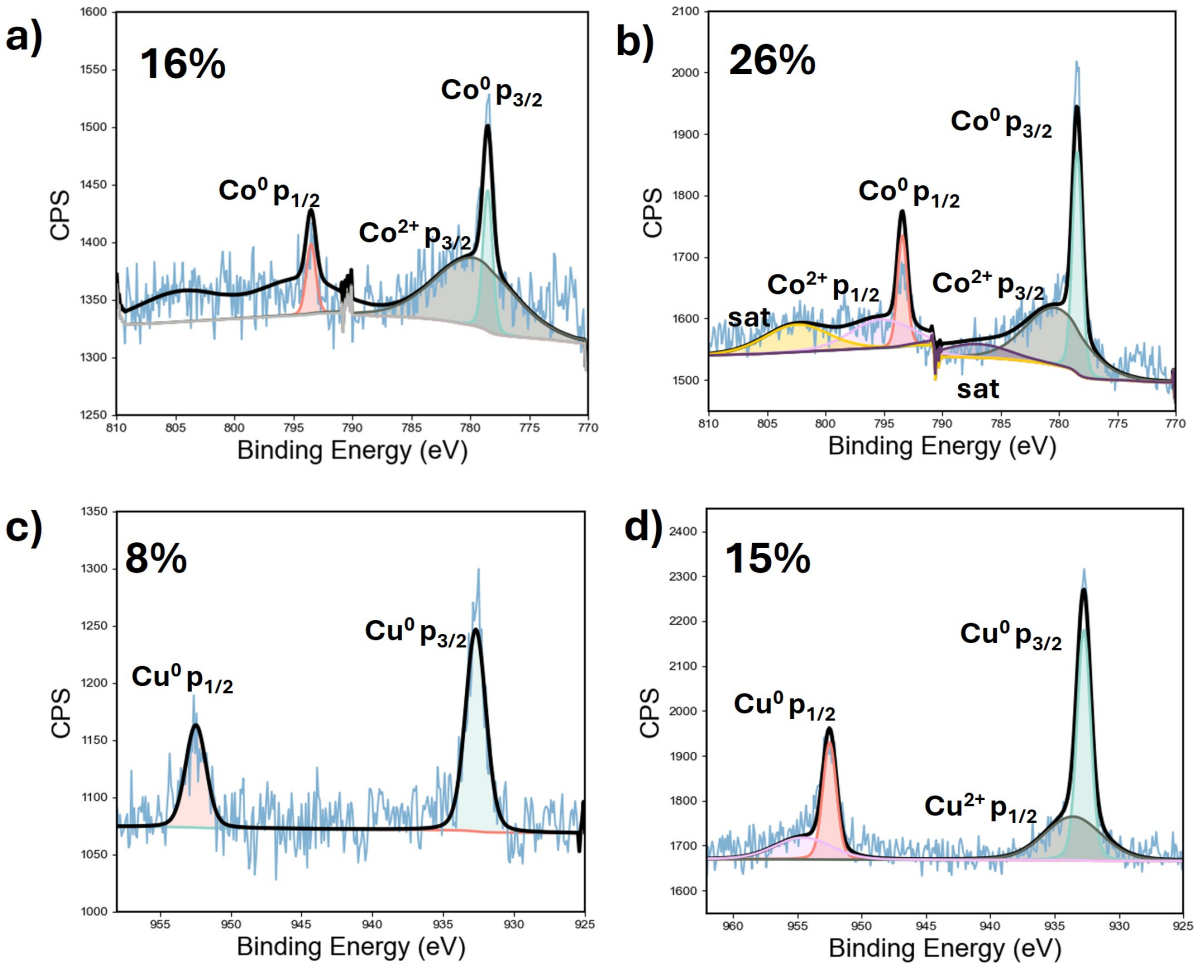

Figure 3.8: XPS of a) NiCoP-16/C, b) NiCoP-26/C, c) NiCuP-8/C, and d) NiCuP-15/C.

annealing treatment. [170] Similarly, XRD of the cobalt-doped Ni_2P catalyst inks (NiCoP-16/C, NiCoP-26/C) demonstrate a phase pure Ni_xCo_yP crystal structure with minimal particle growth (Fig. 3.7). XPS data suggests poorer incorporation of cobalt at similar doping concentrations in comparison to copper after annealing treatment, which is reasonable based on the atomic radii of the dopants (Co > Ni ≈ Cu). [171]

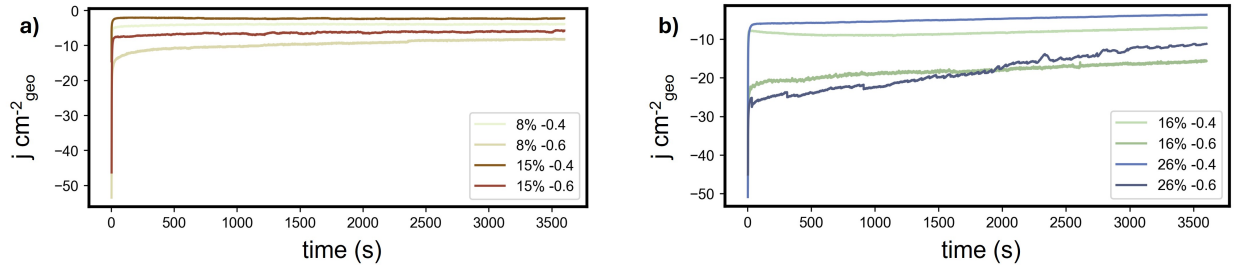

Figure 3.9: Chronoamperometry data of a) copper-doped and b) cobalt-doped Ni_2P/C at$-0.4\,V$ and $-0.6\,V$ vs. RHE.

3.7 NO_3^- electroreduction selectivity

As discussed previously, doping is widely used to synthetically tune catalysts by modulating adsorbate coverage and the resulting reaction selectivity. Notably, HER studies with doped Ni_2P nanocrystals showed a volcano-like trend in activity, where strongly binding (Co) versus weakly binding (Cu) metals at the catalyst surface both demonstrated higher overpotentials for HER. [108] We hypothesized that we could leverage the ability of cobalt and copper to tune ΔG_{H^*} and the resulting NO_3^- electroreduction selectivity between NO_2^-, NH_3, and H_2 from the competitive HER side reaction. To that end, we evaluated the NO_3^- electroreduction selectivity for these materials by conducting bulk electrolysis in aqueous conditions with a separated H-cell, 1:1 0.1 M KH_2PO_4:K_2HPO_4 buffer (pH 6.9), and a catalyst loading of 90 μg, exclusive of the Vulcan carbon support (Fig. 3.9, Chap. 2, Electrochemical Methods). We conducted bulk electrolysis at two potentials based on Ni_2P's selectivity without doping: $-0.4\,V$, where HER is almost entirely outcompeted by NO_3^- electroreduction, and $-0.6\,V$, where HER begins to outcompete NO_3^- electroreduction. The concentrations of NH_3 and NO_2^- were quantified with a well-precedented colorimetric assay method as discussed in 2.10.

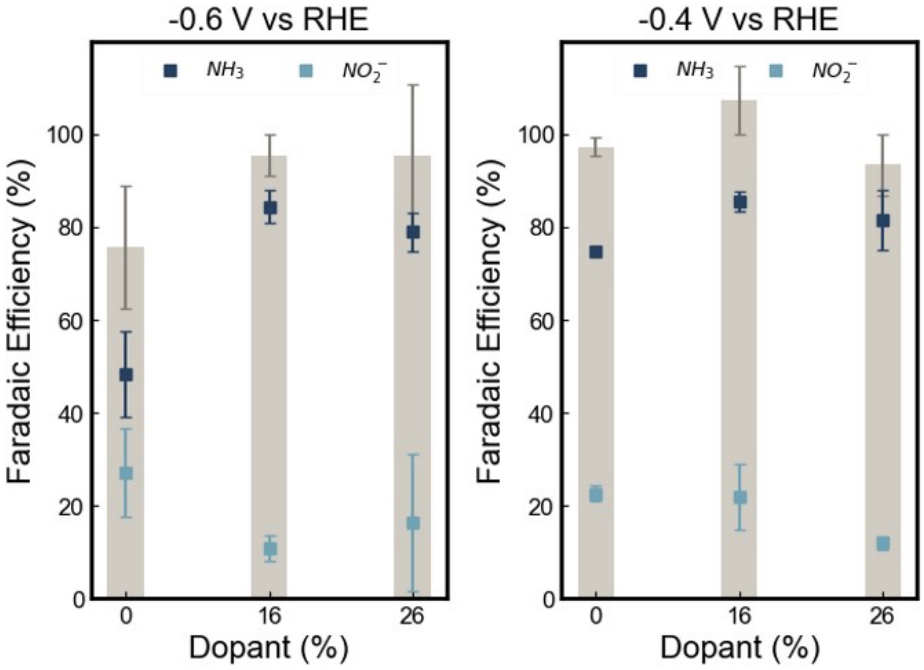

Figure 3.10: NO_3^- electroreduction selectivity of NiCoP-16/C and NiCoP-26/C at -0.4 and -0.6 V vs. RHE. Grey bars indicate total NO_3^- electroreduction selectivity. All measurements have error bars from three repeat experiments.

3.7.1 Cobalt-doped Ni_2P selectivity

After conducting bulk electrolysis with NiCoP-16/C and NiCoP-26/C at -0.4 V and -0.6 V vs. RHE, we observe a preference for NH_3 production over NO_2^- and H_2 (Fig. 3.10). In particular, at -0.6 V vs. RHE, where we begin to see HER dominate kinetically over NO_3^- electroreduction in the case of pure, undoped Ni_2P, we see the suppression of HER ($\leq$ 10% FE) and the drastic increase in NH_3 selectivity ($\geq$ 80% FE) and decrease in NO_2^- selectivity with cobalt incorporation. We hypothesize that this phenomenon is due to cobalt's ability to strongly bind H, which would allow the 8 e^- reduction of NO_3^-- to NH_3 to outcompete HER. This effect is less pronounced at -0.4 V; however, a mild increase in NH_3 selectivity and decrease in NO_2^- selectivity at the highest doping concentration aligns with this hypothesis. This finding is in agreement with previous work with cobalt-containing metal phosphide materials, which shows a preference for NH_3 over

NO_2^- formation. [91, 92, 126] Moreover, Fan and coworkers discuss the critical role of H* in NO_3^- electroreduction on cobalt phosphide materials and propose that the H* coverage needs to be controlled to tune reaction pathways between NO_x hydrogenation and H_2 formation. [172] We believe this concept is applicable to our system, where cobalt incorporation is tuning H* coverage to effectively suppress HER and promote NO_x* hydrogenation relative to the undoped Ni_2P/C material.

3.7.2 Copper-doped Ni_2P selectivity

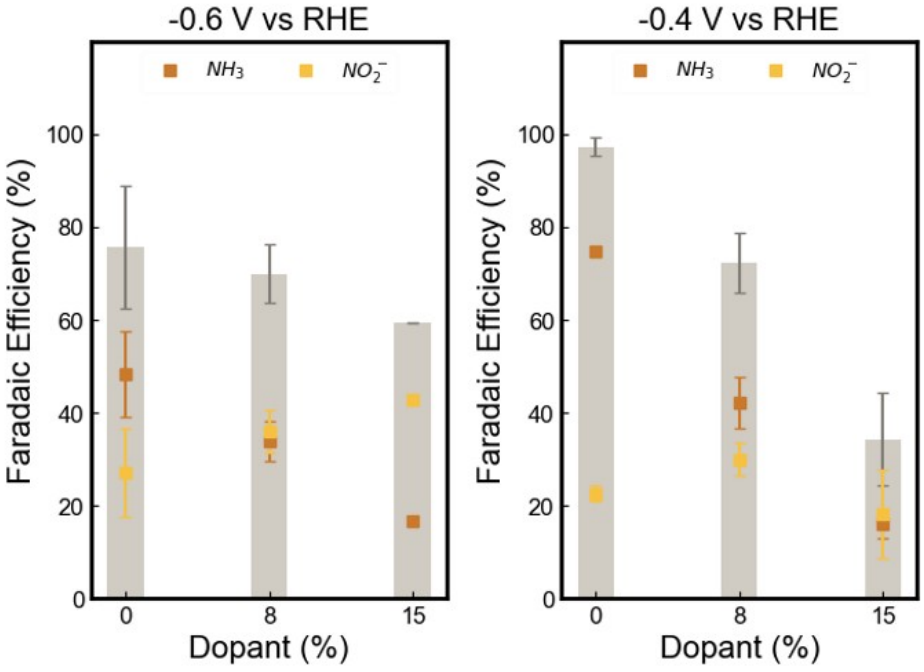

Figure 3.11: NO_3^- electroreduction selectivity of NiCuP-8/C and NiCuP-15/C at -0.4 V and -0.6 V vs. RHE. Grey bars indicate total NO_3^- reduction reaction selectivity. All measurements have error bars from three repeat experiments.

In contrast, there is a 4-fold reduction in NH_3 selectivity and an increase in H_2 selectivity from nearly 0% with pureNi_2P/C to ¿ 60% at -0.4 V as the copper concentration increases (Fig. 3.11). We attribute this to copper's weak hydrogen adsorption capability, where the introduction of

weakly-bound hydrogen causes the 8 e^- reduction of NO_3^- to to NH_3 to be unable to kinetically compete with HER. Notably, previous work with copper-based nanomaterials in phosphate buffered electrolytes also observed high HER activity, which could indicate a non-innocent role of the phosphate ions, i.e. adsorption to the catalyst and assisting in the dimerization of adsorbed H and ultimate H_2 production. [173] We also propose that the presence of weakly-bound hydrogens is also the origin of the steady increase in NO_2^- selectivity with copper concentration at $-0.6\,V$. By introducing weakly-bound hydrogen on the catalyst surface, hydrogenation of adsorbed NO_2^- to NH_3 is inhibited, which aligns with previous work demonstrating that copper catalysts effectively catalyze the reduction of NO_3^- to NO_2^-. [120]

3.7.3 A brief aside: more copper-doped Ni_2P reaction selectivity

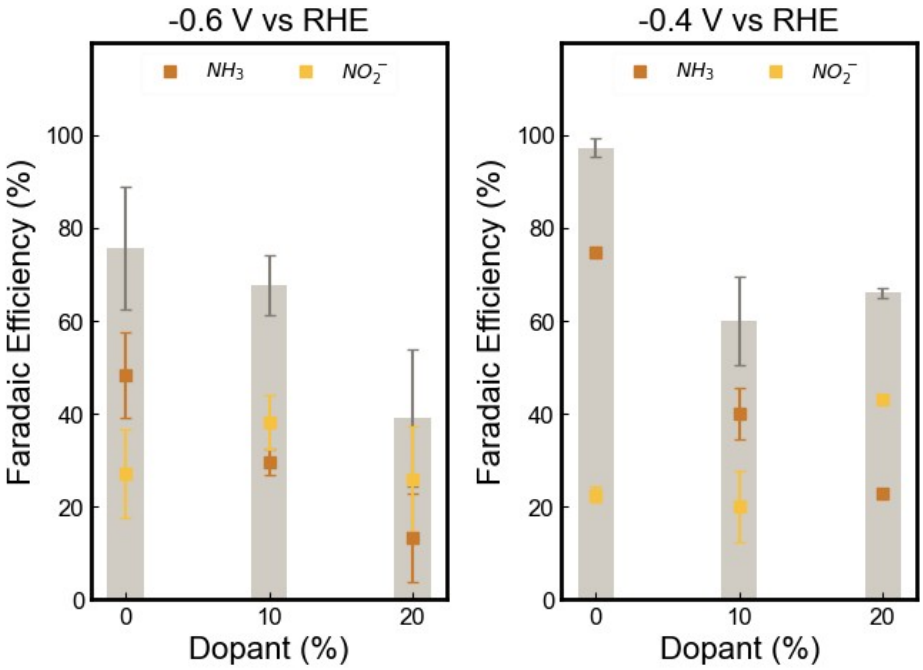

Figure 3.12: NO_3^- electroreduction selectivity of 10% and 20% doped Ni_2P/C at $-0.4\,V$ and $-0.6\,V$ vs. RHE. Grey bars indicate total NO_3^- electroreduction selectivity.

If we measure the reaction selectivity of the 10% and 20% copper-doped Ni_2P nanocrystals,

which have different catalyst loadings than the previously discussed copper and cobalt-doped Ni_2P/C materials, we observe analagous trends to the ones with the 8% and 15% samples: a significant increase in H_2 and decrease in NH_3 (Fig. 3.12). Although the catalyst loadings in these experiments are different than those of the previously discussed copper-doped Ni_2P, the selectivity trends are remarkably similar. If we recall from the previous section, we discussed the differences in particle morphologies between the copper- and cobalt-doped Ni_2P nanocrystals, which could impact the reaction selectivity. However, after being deposited on Vulcan carbon and annealed, the resulting particle morphologies of the copper-doped Ni_2P nanocrystals are similar, regardless of the morphologies of the starting batch of nanocrystals (Figs. 3.C.3, 3.7c & d), which enables us to make a viable comparison of the product selectivity of the four previously discussed samples. Ultimately, we believe that comparing doped materials with identical catalyst loadings is more scientifically rigorous and chose to compare cobalt and copper-doped Ni_2P nanocrystals with identical loadings. However, the consistency in the catalytic behavior of the 10% and 20% copper-doped Ni_2P batches, despite different loadings, fortifies our experimental findings.

3.8 Conclusions and outlook

Ultimately, the reaction selectivity with both copper and cobalt-doped Ni_2P nanocrystals demonstrates how Ni_2P's NO_3^- electroreduction (and HER) selectivity can be significantly modulated by tuning the H-affinity of surface via doping. We utilized two-step, cation exchange synthesis to prepare a series of doped $Ni_{2-x}M_xP$ (M = Cu, Co) nanocrystals. The hexagonal Ni_2P crystal structure was retained and demonstrated stability up to 450 °C. We evaluated the NO_3^- electroreduction selectivity of these materials and observed a direct impact of modulating H-affinity of the material on the reaction selectivity. Cobalt-doped materials show a stronger ability to produce NH_3 and are notably able to suppress HER even at -0.6 V vs. RHE; H_2 selectivity goes from $> 20\%$ to $< 5\%$ after cobalt doping. In contrast, copper-doped materials were less able to produce NH_3 and more prone to producing NO_2^- and H_2, which we attribute to more weakly-bound H present in comparison to the undoped Ni_2P surface. This work demonstrates the utility of using transition metal doping to tune the activity and selectivity of metal phosphide catalysts and sets the stage for developing cost-effective, selective catalysts for NO_3^- electroreduction and beyond.

SUPPLEMENTAL INFORMATION FOR CHAPTER 3

3.A Synthetic Details

3.A.1 Reagents

Technical grade oleylamine (70%, Sigma-Aldrich) was dried by stirring over CaH_2 overnight. The next day it was purified via vacuum distillation and then stored in the glove box. $NiCl_2$ (98% anhydrous, Strem Chemical), tris(diethylamino)phosphine (97%, Sigma-Aldrich), triphenylphosphine (99%, Sigma-Aldrich), $CuCl_2$ (anhydrous, $\geq$ 98%, Millipore-Sigma), $CoCl_2$ (anhydrous, $\geq$ 98%, Millipore-Sigma), and hexadecane (anhydrous $\geq$ 99%, Sigma-Aldrich) was used as received.

3.A.2 Reaction Conditions.

The amount of MCl_2 precursor was varied to achieve desired doping concentrations. Other than the amount of MCl_2, the same reaction conditions were used for all doping experiments. Dopant percent was calculated via ICP-OES with Equation 3.1, where all concentrations are in mM.

$$\text{Doping } \% = \frac{[M]}{[M] + [Ni]} \times 100 \tag{3.1}$$

Ni_2P (mmol)	Mass % Ni_2P nanocrystal	mmol $CuCl_2$ added	equiv Cu w.r.t Ni	Cu dopant % of final material
0.27	0.81	0.04	0.07	8
0.27	0.81	0.08	0.15	15
0.27	0.81	0.14	0.26	36

Table 3.A.1: Reaction conditions for the copper-doping of Ni_2P nanocrystals.

Ni_2P (mmol)	Mass % Ni_2P nanocrystal	mmol $CoCl_2$ added	equiv Co w.r.t Ni	Co dopant % of final material
0.21	0.81	0.06	0.15	16
0.21	0.81	0.13	0.29	26
0.21	0.81	0.34	0.84	31

Table 3.A.2: Reaction conditions for the cobalt-doping of Ni_2P nanocrystals.

3.B Deposition of Ni_2P onto Vulcan carbon

30 wt% of the nanocrystal (excluding ligand mass) was deposited onto Vulcan carbon XC-72. For the deposition, 100 mg of Vulcan carbon was dried in a 100 mL Schlenk flask at 100 °C overnight. Vulcan carbon was transferred into a glovebox and dispersed in 20 mL pentane then sonicated for 5 minutes. The carbon dispersion was stirred at 1500 rpm and a 5 mg/mL nanocrystal solution in chloroform was added dropwise. The mixture was then sonicated for 5 min and transferred back to a glovebox stirring at 1500 rpm overnight. The next day, 15 mL of acetonitrile was added slowly while the suspension was stirred at 800 rpm. The mixture was centrifuged at 7830 rpm for 10 min and the clear supernatant was decanted. The precipitate (Ni_2P/C) was re-dispersed in 10 mL isopropanol. The Ni_2P/C was annealed at 450 °C for 2 hours under 95:5 N_2:H_2 gas flow.

3.C Materials characterization

Material	**Diameter (nm)**
Ni_2P	4.3 ± 0.6
Ni_2P–Co (16%)	4.5 ± 0.4
Ni_2P–Co (26%)	4.9 ± 0.2
Ni_2P–Co (31%)	5.4 ± 0.2
Ni_2P–Cu (8%)	4.6 ± 0.2
Ni_2P–Cu (15%)	4.6 ± 0.4
Ni_2P–Cu (36%)	5.4 ± 0.3

Table 3.C.1: Particle diameters of the series of doped Ni_2P materials.

Material	**Diameter (nm)**
Ni_2P/C	6.5 ± 0.7
Ni_2P–Co/C (16%)	6.4 ± 0.7
Ni_2P–Co/C (26%)	6.2 ± 2.8
Ni_2P–Cu/C (8%)	11.4 ± 0.4
Ni_2P–Cu/C (15%)	5.1 ± 0.8

Table 3.C.2: Particle diameters of the series of doped Ni_2P/C catalyst inks.

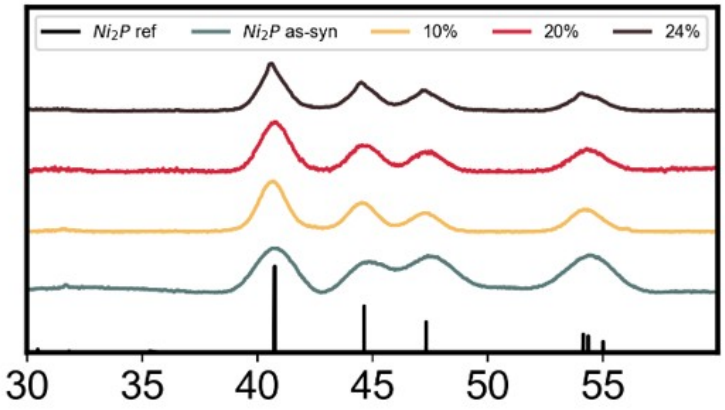

Figure 3.C.1: XRD data of copper-doped Ni_2P with a different starting batch of Ni_2P nanocrystals.

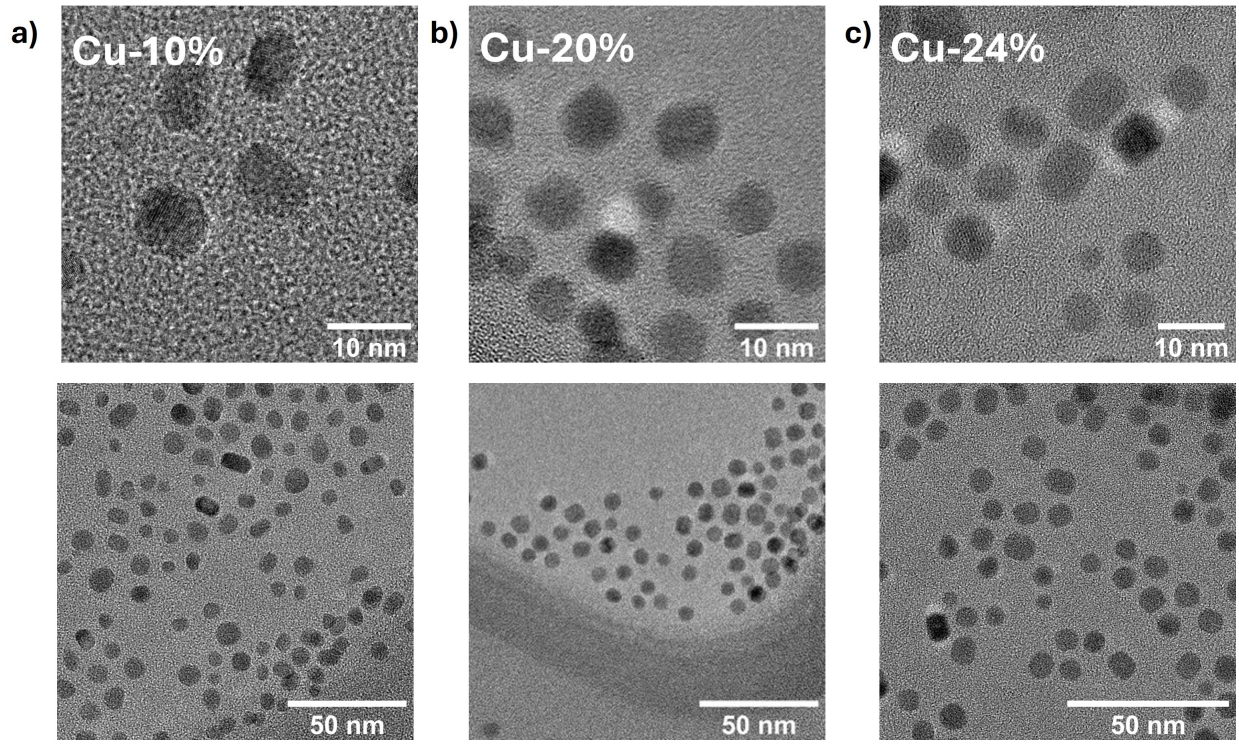

Figure 3.C.2: TEM images of copper-doped Ni_2P nanocrystals that used different starting batch of Ni_2P nanocrystals than the cobalt-doped Ni_2P.

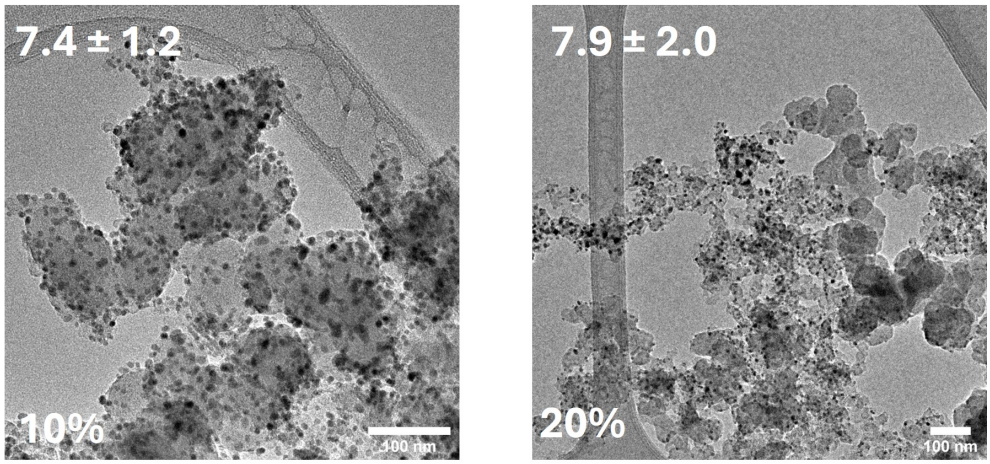

Figure 3.C.3: TEM images of copper-doped Ni_2P/C catalyst inks with a different starting batch of Ni_2P nanocrystals.

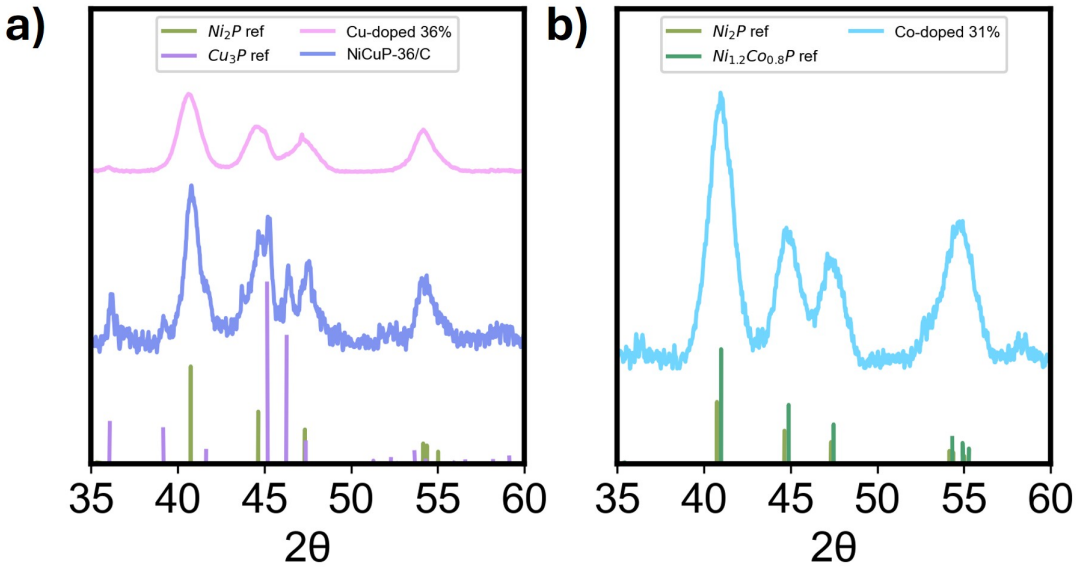

Figure 3.C.4: a) XRD of 36% copper-doped Ni_2P, where additional Cu_3P features grow in after the catalyst ink annealing process. b) 31% cobalt-doped Ni_2P.

3.D Product quantification

Identical product quantification procedures were used to the ones discussed in the Chapter 2 appendix.

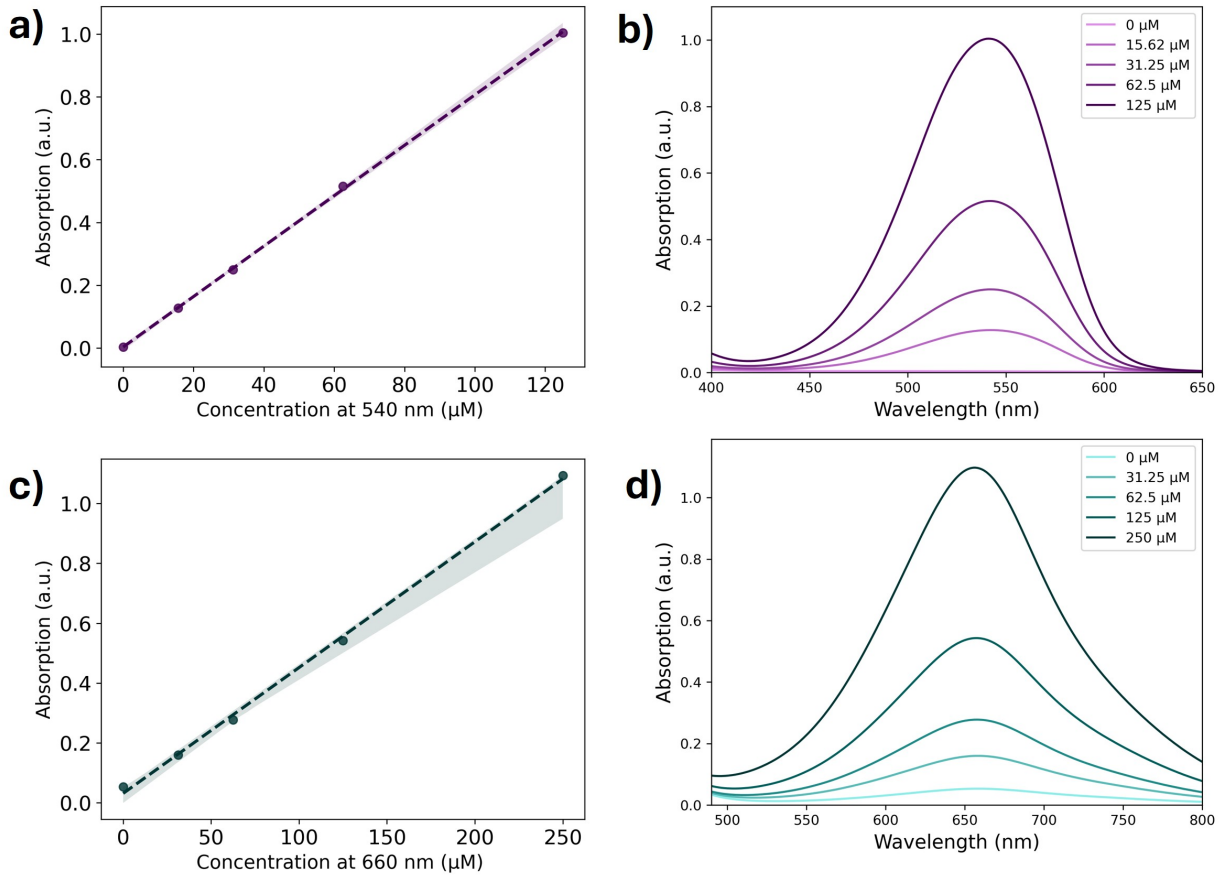

Figure 3.D.1: UV-visible absorption data and calibration curves for NO_2^- quantification (a, b) and NH_3 quantification (c, d)

Chapter 4
CONCLUSIONS AND OUTLOOK

4.1 Conclusions

This thesis is a thorough discussion of the utility of metal phosphides as catalysts for various electrochemical reactions. We discussed the complexity of a transition metal phosphide surface that arises from the various stoichiometries, facets, and surface sites, which makes it difficult to predict their catalytic abilities. This becomes apparent when looking at the range in DFT-calculated $Ni_2P(0001)$ and $CoP(0001)$ ΔG_{H^*} values and the inconsistent reports of TMP HOR activity. However, we note the capabilities of metal phosphides, particularly nickel phosphide, to perform reactions that involve thermal or electrocatalytic hydrogenation and postulate that these active site ensembles on Ni_2P play a critical role during these reactions.

In Chapter 2, we evaluated this hypothesis by studying the ability of Ni_2P nanocrystal to catalyze NO_3^- electroreduction. With a microkinetic analysis, we presented experimental evidence of a competitive adsorption between nitrogenous species and hydrogen, which solidifies the importance of active site ensembles in Ni_2P's NO_3^- electroreduction reaction mechanism. We use this as a foundation to rationalize the selectivity across a series of potentials and note the high NH_3 selectivity at low cathodic potentials.

In Chapter 3, we continued our study in Chapter 2 by using synthetic levers to tune the active site ensembles on Ni_2P nanocrystals. After considering what is known about hydrogen binding affinities on transition metals (i.e., d-band theory), we developed a two-step synthesis that involves cationic exchange with the host nickel cation, copper, and cobalt. Contrary to our intuition based on the relative atomic radii of the three transition metals, copper was less capable of incorporation into Ni_2P compared to cobalt. We conducted bulk electrolysis with these doped nanocrystals and found that, as we expected based on their relative H-binding affinities, cobalt-doped Ni_2P favored NH_3 formation and suppresses HER, while the introduction of weakly-bound H* on copper-doped Ni_2P increased H_2 selectivity.

4.2 Outlook

I would like to recall the two guiding principles for a heterogeneous catalyst from Paul Sabatier and Linus Pauling: [10, 11]

1) The adsorbent should neither be adsorbed too strongly nor too weakly.

2) The catalyst must bind the transition state more tightly than the substrate.

From my point of view, Pauling's principle remains true and neatly supports our proposition that the presence of strongly-bound hydrogens onNi_2P is the reason for high NH_3 selectivity in NO_3^- electroreduction. While the Sabatier principle is generally applied in the context of descriptors and a volcano plot, I have realized that it is also applicable in the context of more complex systems. On a transition metal phosphide surface, achieving the optimal coverage to selectively produce one product over another is achieved by the adsorbates having ideal adsorption energetics relative to one another: not too strong nor too weak. This may mean that an adsorbate *should* be bound "too strongly"—so that it can be utilized to make multi-electron products.

Needless to say, identifying what an "ideal" catalyst surface is difficult, especially with multi-elemental materials, whose mechanisms are often complex. We hope that our work in Chapter 2 will inspire more experimental mechanistic studies with metal phosphide materials with NO_3^- electroreduction and beyond. Additionally, the high NH_3 selectivity at low overpotentials is intriguing and raises the question whether we could investigate other nickel phosphide stoichiometries, or even conduct NO_3^- electroreduction with a series of solvents and electrolytes with varying pKas to tune NH_3 selectivity by explicitly controlling hydrogen concentration in the system.

Lastly, there is room for more investigation with the doping of Ni_2P nanocrystals via cation exchange. Understanding the limits of dopant incorporation, the extent of dopant incorporation into the host lattice, and how to maintain morphology are all questions that remain unanswered. While we did see catalytic trends with these materials based that aligned with what we would expect based on d-band theory, probing the H-affinity with these materials with techniques such as H_2-TPR and H_2-TPD would be informative to further these conclusions.

BIBLIOGRAPHY

[1] M. Elizabeth Mundy, David Ung, Nathan L. Lai, Evan P. Jahrman, Gerald T. Seidler, and Brandi M. Cossairt. Aminophosphines as Versatile Precursors for the Synthesis of Metal Phosphide Nanocrystals. *Chemistry of Materials*, 30(15):5373–5379, August 2018. Publisher: American Chemical Society.

[2] Ding-Yuan Kuo, Emily Nishiwaki, Ricardo A. Rivera-Maldonado, and Brandi M. Cossairt. The Role of Hydrogen Adsorption Site Diversity in Catalysis on Transition-Metal Phosphide Surfaces. *ACS Catalysis*, 13(1):287–295, January 2023. Publisher: American Chemical Society.

[3] Yong Yang, Mingchuan Luo, Weiyu Zhang, Yingjun Sun, Xu Chen, and Shaojun Guo. Metal Surface and Interface Energy Electrocatalysis: Fundamentals, Performance Engineering, and Opportunities. *Chem*, 4(9):2054–2083, September 2018. Publisher: Elsevier.

[4] Christopher J. Pickett and Jean Talarmin. Electrosynthesis of ammonia. *Nature*, 317(6038):652–653, October 1985. Publisher: Nature Publishing Group.

[5] Robert Schlögl. Heterogeneous Catalysis. *Angewandte Chemie International Edition*, 54(11):3465–3520, 2015. _eprint: https://onlinelibrary.wiley.com/doi/pdf/10.1002/anie.201410738.

[6] Arne Kätelhön, Raoul Meys, Sarah Deutz, Sangwon Suh, and André Bardow. Climate change mitigation potential of carbon capture and utilization in the chemical industry. *Proceedings of the National Academy of Sciences*, 116(23):11187–11194, June 2019. Publisher: Proceedings of the National Academy of Sciences.

[7] Matthew C. Leech and Kevin Lam. A practical guide to electrosynthesis. *Nature Reviews Chemistry*, 6(4):275–286, April 2022. Publisher: Nature Publishing Group.

[8] Yong Yuan and Aiwen Lei. Is electrosynthesis always green and advantageous compared to traditional methods? *Nature Communications*, 11(1):802, February 2020. Publisher: Nature Publishing Group.

[9] Charlotte Vogt and Bert M. Weckhuysen. The concept of active site in heterogeneous catalysis. *Nature Reviews Chemistry*, 6(2):89–111, February 2022. Publisher: Nature Publishing Group.

[10] Paul Sabatier and Jaun-Baptiste Senderenes. *Hydrogénation directe des oxydes du carbone en présence de divers métaux divisés*, volume 134. 1902.

[11] Linus Pauling. Interatomic Distances and Bond Character in the Oxygen Acids and Related Substances. *The Journal of Physical Chemistry*, 56(3):361–365, March 1952.

[12] David M. Koshy, Sindhu S. Nathan, Arun S. Asundi, Ahmed M. Abdellah, Samuel M. Dull, David A. Cullen, Drew Higgins, Zhenan Bao, Stacey F. Bent, and Thomas F. Jaramillo. Bridging Thermal Catalysis and Electrocatalysis: Catalyzing CO2 Conversion with Carbon-Based Materials. *Angewandte Chemie International Edition*, 60(32):17472–17480, 2021. _eprint: https://onlinelibrary.wiley.com/doi/pdf/10.1002/anie.202101326.

[13] Shuai Yuan, Yanding Li, Jiayu Peng, Ydna M. Questell-Santiago, Karthik Akkiraju, Livia Giordano, Daniel J. Zheng, Sujay Bagi, Yuriy Román-Leshkov, and Yang Shao-Horn. Conversion of Methane into Liquid Fuels—Bridging Thermal Catalysis with Electrocatalysis. *Advanced Energy Materials*, 10(40):2002154, 2020. _eprint: https://advanced.onlinelibrary.wiley.com/doi/pdf/10.1002/aenm.202002154.

[14] Kate M. Waldie, Kristen R. Flajslik, Elizabeth McLoughlin, Christopher E. D. Chidsey, and Robert M. Waymouth. Electrocatalytic Alcohol Oxidation with Ruthenium Transfer Hydrogenation Catalysts. *Journal of the American Chemical Society*, 139(2):738–748, January 2017. Publisher: American Chemical Society.

[15] Yifeng Shi, Zhiheng Lyu, Ming Zhao, Ruhui Chen, Quynh N. Nguyen, and Younan Xia. Noble-Metal Nanocrystals with Controlled Shapes for Catalytic and Electrocatalytic Applications. *Chemical Reviews*, 121(2):649–735, January 2021. Publisher: American Chemical Society.

[16] Yannick T. Guntern, Valery Okatenko, James Pankhurst, Seyedeh Behnaz Varandili, Pranit Iyengar, Cedric Koolen, Dragos Stoian, Jan Vavra, and Raffaella Buonsanti. Colloidal Nanocrystals as Electrocatalysts with Tunable Activity and Selectivity. *ACS Catalysis*, 11(3):1248–1295, February 2021. Publisher: American Chemical Society.

[17] Yuen Wu, Dingsheng Wang, and Yadong Li. Nanocrystals from solutions: catalysts. *Chemical Society Reviews*, 43(7):2112–2124, March 2014. Publisher: The Royal Society of Chemistry.

[18] Hemma Mistry, Ana Sofia Varela, Stefanie Kühl, Peter Strasser, and Beatriz Roldan Cuenya. Nanostructured electrocatalysts with tunable activity and selectivity. *Nature Reviews Materials*, 1(4):1–14, March 2016. Number: 4 Publisher: Nature Publishing Group.

[19] David Ung, Ian A. Murphy, and Brandi M. Cossairt. Designing nanoparticle interfaces for inner-sphere catalysis. *Dalton Transactions*, 49(16):4995–5005, 2020. Publisher: Royal Society of Chemistry.

[20] Ian A. Murphy, Peter S. Rice, Madison Monahan, Leo P. Zasada, Elisa M. Miller, Simone Raugei, and Brandi M. Cossairt. Covalent Functionalization of Nickel Phosphide Nanocrystals with Aryl-Diazonium Salts. *Chemistry of Materials*, 33(24):9652–9665, December 2021. Publisher: American Chemical Society.

[21] Stephanie L. Brock and Keerthi Senevirathne. Recent developments in synthetic approaches to transition metal phosphide nanoparticles for magnetic and catalytic applications. *Journal of Solid State Chemistry*, 181(7):1552–1559, July 2008.

[22] Keming Wu, Congcong Sun, Zhenni Wang, Qian Song, Xiaoxia Bai, Xin Yu, Qiang Li, Zheng Wang, Hui Zhang, Jian Zhang, Xin Tong, Yanping Liang, Ajit Khosla, and Zhenhuan Zhao. Surface Reconstruction on Uniform Cu Nanodisks Boosted Electrochemical Nitrate Reduction to Ammonia. *ACS Materials Letters*, 4(4):650–656, April 2022. Publisher: American Chemical Society.

[23] Yanmei Shi, Mengyang Li, Yifu Yu, and Bin Zhang. Recent advances in nanostructured transition metal phosphides: synthesis and energy-related applications. *Energy & Environmental Science*, 13(12):4564–4582, 2020. Publisher: Royal Society of Chemistry.

[24] Xiang Li, Mohong Lu, Anjie Wang, Chunshan Song, and Yongkang Hu. Promoting Effect of TiO2 on the Hydrodenitrogenation Performance of Nickel Phosphide. *The Journal of Physical Chemistry C*, 112(42):16584–16592, October 2008. Publisher: American Chemical Society.

[25] Richard H. Bowker, Boris Ilic, Bo A. Carrillo, Michael A. Reynolds, Brendan D. Murray, and Mark E. Bussell. Carbazole hydrodenitrogenation over nickel phosphide and Ni-rich bimetallic phosphide catalysts. *Applied Catalysis A: General*, 482:221–230, July 2014.

[26] Alba B. Vidal, José Luis Peña-Mena, Oscar Hurtado-Aular, Rafael Añez, and Aníbal Sierraalta. Unraveling the Structure and Surface Chemistry of the Phosphosulfide Phase Formed on Ni2P under Hydrodesulfurization Reaction Conditions: A DFT Study. *The Journal of Physical Chemistry C*, 126(33):14187–14200, August 2022. Publisher: American Chemical Society.

[27] Autumn W. Burns, Amy F. Gaudette, and Mark E. Bussell. Hydrodesulfurization properties of cobalt–nickel phosphide catalysts: Ni-rich materials are highly active. *Journal of Catalysis*, 260(2):262–269, December 2008.

[28] S. Ted Oyama and Yong-Kul Lee. The active site of nickel phosphide catalysts for the hydrodesulfurization of 4,6-DMDBT. *Journal of Catalysis*, 258(2):393–400, September 2008.

[29] Meng Sun, Huijuan Liu, Jiuhui Qu, and Jinghong Li. Earth-Rich Transition Metal Phosphide for Energy Conversion and Storage. *Advanced Energy Materials*, 6(13):1600087, 2016. _eprint: https://advanced.onlinelibrary.wiley.com/doi/pdf/10.1002/aenm.201600087.

[30] Zonghua Pu, Tingting Liu, Ibrahim Saana Amiinu, Ruilin Cheng, Pengyan Wang, Chengtian Zhang, Pengxia Ji, Weihua Hu, Jian Liu, and Shichun Mu. Transition-Metal Phosphides: Activity Origin, Energy-Related Electrocatalysis Applications, and Synthetic Strategies. *Advanced Functional Materials*, 30(45):2004009, 2020. _eprint: https://advanced.onlinelibrary.wiley.com/doi/pdf/10.1002/adfm.202004009.

[31] Jakob Kibsgaard, Charlie Tsai, Karen Chan, Jesse D. Benck, Jens K. Nørskov, Frank Abild-Pedersen, and Thomas F. Jaramillo. Designing an improved transition metal phosphide catalyst for hydrogen evolution using experimental and theoretical trends. *Energy & Environmental Science*, 8(10):3022–3029, October 2015. Publisher: The Royal Society of Chemistry.

[32] Eric J. Popczun, James R. McKone, Carlos G. Read, Adam J. Biacchi, Alex M. Wiltrout, Nathan S. Lewis, and Raymond E. Schaak. Nanostructured Nickel Phosphide as an Electrocatalyst for the Hydrogen Evolution Reaction. *Journal of the American Chemical Society*, 135(25):9267–9270, June 2013. Publisher: American Chemical Society.

[33] Yanmei Shi and Bin Zhang. Recent advances in transition metal phosphide nanomaterials: synthesis and applications in hydrogen evolution reaction. *Chemical Society Reviews*, 45(6):1529–1541, March 2016. Publisher: The Royal Society of Chemistry.

[34] Chen-Chen Weng, Jin-Tao Ren, and Zhong-Yong Yuan. Transition Metal Phosphide-Based Materials for Efficient Electrochemical Hydrogen Evolution: A Critical Review. *ChemSusChem*, 13(13):3357–3375, 2020. _eprint: https://onlinelibrary.wiley.com/doi/pdf/10.1002/cssc.202000416.

[35] Ping Liu and José A. Rodriguez. Catalysts for Hydrogen Evolution from the [NiFe] Hydrogenase to the Ni2P(001) Surface: The Importance of Ensemble Effect. *Journal of the American Chemical Society*, 127(42):14871–14878, October 2005. Publisher: American Chemical Society.

[36] Anders B. Laursen, Robert B. Wexler, Marianna J. Whitaker, Edward J. Izett, Karin U. D. Calvinho, Shinjae Hwang, Ross Rucker, Hao Wang, Jing Li, Eric Garfunkel, Martha Greenblatt, Andrew M. Rappe, and G. Charles Dismukes. Climbing the Volcano of Electrocatalytic Activity while Avoiding Catalyst Corrosion: Ni3P, a Hydrogen Evolution Electrocatalyst Stable in Both Acid and Alkali. *ACS Catalysis*, 8(5):4408–4419, May 2018. Publisher: American Chemical Society.

[37] Wolfgang Jeitschko, Aloys J. Foecker, Dirk Paschke, Martin V. Dewalsky, Ch. B. H. Evers, Bernd Künnen, Arne Lang, Gunter Kotzyba, Ute Ch. Rodewald, and Manfred H. Möller. Crystal Structure and Properties of Some Filled and Unfilled Skutterudites: GdFe4P12, SmFe4P12, NdFe4As12, Eu0.54Co4Sb12, Fe0.5Ni0.5P3, CoP3, and NiP3. *Zeitschrift für anorganische und allgemeine Chemie*, 626(5):1112–1120, 2000. _eprint: https://onlinelibrary.wiley.com/doi/pdf/10.1002/%28SICI%291521-3749%28200005%29626%3A5%3C1112%3A%3AAID-ZAAC1112%3E3.0.CO%3B2-E.

[38] Haiyan Zhao, S. Ted Oyama, Hans-Joachim Freund, Radosław Włodarczyk, and Marek Sierka. Nature of active sites in Ni2P hydrotreating catalysts as probed by iron substitution. *Applied Catalysis B: Environmental*, 164:204–216, March 2015.

[39] Chenyang Li, Hao Gao, Wan Wan, and Tim Mueller. Mechanisms for hydrogen evolution on transition metal phosphide catalysts and a comparison to Pt(111). *Physical Chemistry Chemical Physics*, 21(44):24489–24498, November 2019. Publisher: The Royal Society of Chemistry.

[40] Guoxiang Hu, Qing Tang, and De-en Jiang. CoP for hydrogen evolution: implications from hydrogen adsorption. *Physical Chemistry Chemical Physics*, 18(34):23864–23871, 2016. Publisher: Royal Society of Chemistry.

[41] Martin H. Hansen, Lucas-Alexandre Stern, Ligang Feng, Jan Rossmeisl, and Xile Hu. Widely available active sites on Ni 2 P for electrochemical hydrogen evolution – insights from first principles calculations. *Physical Chemistry Chemical Physics*, 17(16):10823–10829, 2015. Publisher: Royal Society of Chemistry.

[42] Mónica García-Diéguez, David D. Hibbitts, and Enrique Iglesia. Hydrogen Chemisorption Isotherms on Platinum Particles at Catalytic Temperatures: Langmuir and Two-Dimensional Gas Models Revisited. *The Journal of Physical Chemistry C*, 123(13):8447–8462, April 2019. Publisher: American Chemical Society.

[43] Manuel J. Kolb, Anna L. Garden, Cansin Badan, José A. Garrido Torres, Egill Skúlason, Ludo B. F. Juurlink, Hannes Jónsson, and Marc T. M. Koper. Elucidation of temperature-programmed desorption of high-coverage hydrogen on Pt(211), Pt(221), Pt(533) and Pt(553) based on density functional theory calculations. *Physical Chemistry Chemical Physics*, 21(31):17142–17151, 2019. Publisher: Royal Society of Chemistry.

[44] Olga A. Yakovina and Alexander S. Lisitsyn. Probing the H2-Induced Restructuring of Pt Nanoclusters by H2-TPD. *Langmuir*, 32(46):12013–12021, November 2016. Publisher: American Chemical Society.

[45] J. K. Nørskov, T. Bligaard, A. Logadottir, J. R. Kitchin, J. G. Chen, S. Pandelov, and U. Stimming. Trends in the Exchange Current for Hydrogen Evolution. *Journal of The Electrochemical Society*, 152(3):J23, January 2005. Publisher: IOP Publishing.

[46] B. Hammer, L. B. Hansen, and J. K. Nørskov. Improved adsorption energetics within density-functional theory using revised Perdew-Burke-Ernzerhof functionals. *Physical Review B*, 59(11):7413–7421, March 1999. Publisher: American Physical Society.

[47] Wassilios Papawassiliou, José P. Carvalho, Nikolaos Panopoulos, Yasser Al Wahedi, Vijay Kumar Shankarayya Wadi, Xinnan Lu, Kyriaki Polychronopoulou, Jin Bae Lee, Sanggil Lee, Chang Yeon Kim, Hae Jin Kim, Marios Katsiotis, Vasileios Tzitzios, Marina Karagianni, Michael Fardis, Georgios Papavassiliou, and Andrew J. Pell. Crystal and electronic facet analysis of ultrafine Ni2P particles by solid-state NMR nanocrystallography. *Nature Communications*, 12(1):4334, July 2021. Publisher: Nature Publishing Group.

[48] Robert B. Wexler, John Mark P. Martirez, and Andrew M. Rappe. Active Role of Phosphorus in the Hydrogen Evolving Activity of Nickel Phosphide (0001) Surfaces. *ACS Catalysis*, 7(11):7718–7725, November 2017. Publisher: American Chemical Society.

[49] Russell W. Cross and Nelson Y. Dzade. First-Principles Mechanistic Insights into the Hydrogen Evolution Reaction on Ni2P Electrocatalyst in Alkaline Medium. *Catalysts*, 10(3):307, March 2020. Number: 3 Publisher: Multidisciplinary Digital Publishing Institute.

[50] Mikko Hakala and Kari Laasonen. Hydrogen adsorption trends on Al-doped Ni2P surfaces for optimal catalyst design. *Physical Chemistry Chemical Physics*, 20(20):13785–13791, May 2018. Publisher: The Royal Society of Chemistry.

[51] Ji-Sue Moon, Jue-Hyuk Jang, Eung-Gun Kim, Young-Hoon Chung, Sung Jong Yoo, and Yong-Kul Lee. The nature of active sites of Ni2P electrocatalyst for hydrogen evolution reaction. *Journal of Catalysis*, 326:92–99, June 2015.

[52] Don-Hyung Ha, Binghong Han, Marcel Risch, Livia Giordano, Koffi P. C. Yao, Pinar Karayaylali, and Yang Shao-Horn. Activity and stability of cobalt phosphides for hydrogen evolution upon water splitting. *Nano Energy*, 29:37–45, November 2016.

[53] Xiaofei Cao, Yuan Tan, Huaan Zheng, Jun Hu, Xi Chen, and Zhong Chen. Effect of cobalt phosphide (CoP) vacancies on its hydrogen evolution activity via water splitting: a theoretical study. *Physical Chemistry Chemical Physics*, 24(7):4644–4652, February 2022. Publisher: The Royal Society of Chemistry.

[54] Shuang Cao, Yong Chen, Hui Wang, Jie Chen, Xinghua Shi, Hongmei Li, Ping Cheng, Xinfeng Liu, Min Liu, and Lingyu Piao. Ultrasmall CoP Nanoparticles as Efficient Cocatalysts for Photocatalytic Formic Acid Dehydrogenation. *Joule*, 2(3):549–557, March 2018. Publisher: Elsevier.

[55] Yue Xin, Shuhui Li, Yayang Qian, Wenkun Zhu, Haibo Yuan, Pengyan Jiang, Ruihan Guo, and Liangbing Wang. High-Entropy Alloys as a Platform for Catalysis: Progress, Challenges, and Opportunities. *ACS Catalysis*, 10(19):11280–11306, October 2020. Publisher: American Chemical Society.

[56] A. Infantes-Molina, E. Gralberg, J. A. Cecilia, Elisabetta Finocchio, and E. Rodríguez-Castellón. Nickel and cobalt phosphides as effective catalysts for oxygen removal of dibenzofuran: role of contact time, hydrogen pressure and hydrogen/feed molar ratio. *Catalysis Science & Technology*, 5(6):3403–3415, May 2015. Publisher: The Royal Society of Chemistry.

[57] Kelun Li, Rijie Wang, and Jixiang Chen. Hydrodeoxygenation of Anisole over Silica-Supported Ni2P, MoP, and NiMoP Catalysts. *Energy & Fuels*, 25(3):854–863, March 2011. Publisher: American Chemical Society.

[58] Jixiang Chen, Lingmin Sun, Rijie Wang, and Jiyan Zhang. Hydrodechlorination of Chlorobenzene Over Ni2P/SiO2 Catalysts: Influence of Ni2P Loading. *Catalysis Letters*, 133(3):346–353, December 2009. Company: Springer Distributor: Springer Institution: Springer Label: Springer Number: 3 Publisher: Springer US.

[59] Maya Kiskinova and D. Wayne Goodman. Modification of chemisorption properties by electronegative adatoms: H2 and CO on chlorided, sulfided, and phosphided Ni(100). *Surface Science*, 108(1):64–76, June 1981.

[60] Wenchao Sheng, Adam P. Bivens, MyatNoeZin Myint, Zhongbin Zhuang, Robert V. Forest, Qianrong Fang, Jingguang G. Chen, and Yushan Yan. Non-precious metal electrocatalysts with high activity for hydrogen oxidation reaction in alkaline electrolytes. *Energy & Environmental Science*, 7(5):1719–1724, April 2014. Publisher: The Royal Society of Chemistry.

[61] Jixiang Chen, Shaojun Zhou, Donghui Ci, Jianxiang Zhang, Rijie Wang, and Jiyan Zhang. Influence of Supports on Structure and Performance of Nickel Phosphide Catalysts for Hydrodechlorination of Chlorobenzene. *Industrial & Engineering Chemistry Research*, 48(8):3812–3819, April 2009. Publisher: American Chemical Society.

[62] Xuguang Liu, Jixiang Chen, and Jiyan Zhang. Hydrodechlorination of Chlorobenzene over Silica-Supported Nickel Phosphide Catalysts. *Industrial & Engineering Chemistry Research*, 47(15):5362–5368, August 2008. Publisher: American Chemical Society.

[63] J. A. Cecilia, A. Infantes-Molina, E. Rodríguez-Castellón, and A. Jiménez-López. Gas phase catalytic hydrodechlorination of chlorobenzene over cobalt phosphide catalysts with different P contents. *Journal of Hazardous Materials*, 260:167–175, September 2013.

[64] Jie Zheng, Wenchao Sheng, Zhongbin Zhuang, Bingjun Xu, and Yushan Yan. Universal dependence of hydrogen oxidation and evolution reaction activity of platinum-group metals on pH and hydrogen binding energy. *Science Advances*, 2(3):e1501602, March 2016. Publisher: American Association for the Advancement of Science.

[65] Alireza Zolfaghari, Martine Chayer, and Gregory Jerkiewicz. Energetics of the Underpotential Deposition of Hydrogen on Platinum Electrodes: I. Absence of Coadsorbed Species. *Journal of The Electrochemical Society*, 144(9):3034, September 1997. Publisher: IOP Publishing.

[66] N. M. Marković, T. J. Schmidt, B. N. Grgur, H. A. Gasteiger, R. J. Behm, and P. N. Ross. Effect of Temperature on Surface Processes at the Pt(111)Liquid Interface: Hydrogen Adsorption, Oxide Formation, and CO Oxidation. *The Journal of Physical Chemistry B*, 103(40):8568–8577, October 1999. Publisher: American Chemical Society.

[67] Wenchao Sheng, Zhongbin Zhuang, Minrui Gao, Jie Zheng, Jingguang G. Chen, and Yushan Yan. Correlating hydrogen oxidation and evolution activity on platinum at different pH with measured hydrogen binding energy. *Nature Communications*, 6(1):5848, January 2015. Publisher: Nature Publishing Group.

[68] Merfat M. Alsabban, Mathan Kumar Eswaran, Karthik Peramaiah, Wandi Wahyudi, Xiulin Yang, Vinoth Ramalingam, Mohamed. N. Hedhili, Xiaohe Miao, Udo Schwingenschlögl, Lain-Jong Li, Vincent Tung, and Kuo-Wei Huang. Unusual Activity of Rationally Designed Cobalt Phosphide/Oxide Heterostructure Composite for Hydrogen Production in Alkaline Medium. *ACS Nano*, 16(3):3906–3916, March 2022. Publisher: American Chemical Society.

[69] Murielle F. Delley, Zishan Wu, M. Elizabeth Mundy, David Ung, Brandi M. Cossairt, Hailiang Wang, and James M. Mayer. Hydrogen on Cobalt Phosphide. *Journal of the American Chemical Society*, 141(38):15390–15402, September 2019. Publisher: American Chemical Society.

[70] Rishi G. Agarwal, Scott C. Coste, Benjamin D. Groff, Abigail M. Heuer, Hyunho Noh, Giovanny A. Parada, Catherine F. Wise, Eva M. Nichols, Jeffrey J. Warren, and James M. Mayer. Free Energies of Proton-Coupled Electron Transfer Reagents and Their Applications. *Chemical Reviews*, December 2021. Publisher: American Chemical Society.

[71] Eric J. Popczun, Carlos G. Read, Christopher W. Roske, Nathan S. Lewis, and Raymond E. Schaak. Highly Active Electrocatalysis of the Hydrogen Evolution Reaction by Cobalt Phosphide Nanoparticles. *Angewandte Chemie International Edition*, 53(21):5427–5430, 2014. _eprint: https://onlinelibrary.wiley.com/doi/pdf/10.1002/anie.201402646.

[72] Elayaraja Muthuswamy, Galbokka H. Layan Savithra, and Stephanie L. Brock. Synthetic Levers Enabling Independent Control of Phase, Size, and Morphology in Nickel Phosphide Nanoparticles. *ACS Nano*, 5(3):2402–2411, March 2011. Publisher: American Chemical Society.

[73] Andres Parra-Puerto, Kai Ling Ng, Kieran Fahy, Angela E. Goode, Mary P. Ryan, and Anthony Kucernak. Supported Transition Metal Phosphides: Activity Survey for HER, ORR, OER, and Corrosion Resistance in Acid and Alkaline Electrolytes. *ACS Catalysis*, 9(12):11515–11529, December 2019. Publisher: American Chemical Society.

[74] Anthony R. J. Kucernak, K. F. Fahy, and V. N. Naranammalpuram Sundaram. Facile synthesis of palladium phosphide electrocatalysts and their activity for the hydrogen oxidation, hydrogen evolutions, oxygen reduction and formic acid oxidation reactions. *Catalysis Today*, 262:48–56, March 2016.

[75] Fulin Yang, Xi Bao, Dan Gong, Lixin Su, Gongzhen Cheng, Shengli Chen, and Wei Luo. Rhodium Phosphide: A New Type of Hydrogen Oxidation Reaction Catalyst with Non-Linear Correlated Catalytic Response to pH. *ChemElectroChem*, 6(7):1990–1995, 2019. _eprint: https://onlinelibrary.wiley.com/doi/pdf/10.1002/celc.201900129.

[76] Lin Wei, Da-Jiang Liu, Bryan A. Rosales, James W. Evans, and Javier Vela. Mild and Selective Hydrogenation of Nitrate to Ammonia in the Absence of Noble Metals. *ACS Catalysis*, 10(6):3618–3628, March 2020. Publisher: American Chemical Society.

[77] Qi Zhang, Matthew Bown, Laura Pastor-Pérez, Melis S. Duyar, and Tomas R. Reina. CO2 Conversion via Reverse Water Gas Shift Reaction Using Fully Selective Mo–P Multicomponent Catalysts. *Industrial & Engineering Chemistry Research*, 61(34):12857–12865, August 2022. Publisher: American Chemical Society.

[78] Sha Cui, Xiaosheng Wang, Luhui Wang, and Xianmin Zheng. Enhanced selectivity of the CO 2 reverse water–gas reaction over a Ni 2 P/CeO 2 catalyst. *Dalton Transactions*, 50(17):5978–5987, 2021. Publisher: Royal Society of Chemistry.

[79] Miriam González-Castaño, Estelle le Saché, Cameron Berry, Laura Pastor-Pérez, Harvey Arellano-García, Qiang Wang, and Tomás R. Reina. Nickel Phosphide Catalysts as Efficient Systems for CO2 Upgrading via Dry Reforming of Methane. *Catalysts*, 11(4):446, April 2021. Number: 4 Publisher: Multidisciplinary Digital Publishing Institute.

[80] Zhiwei Yao, Fubing Luan, Yue Sun, Baojiang Jiang, Jia Song, and Haiyan Wang. Molybdenum phosphide as a novel and stable catalyst for dry reforming of methane. *Catalysis Science & Technology*, 6(22):7996–8004, 2016. Publisher: Royal Society of Chemistry.

[81] Melis S. Duyar, Charlie Tsai, Jonathan L. Snider, Joseph A. Singh, Alessandro Gallo, Jong Suk Yoo, Andrew J. Medford, Frank Abild-Pedersen, Felix Studt, Jakob Kibsgaard, Stacey F. Bent, Jens K. Nørskov, and Thomas F. Jaramillo. A Highly Active Molybdenum Phosphide Catalyst for Methanol Synthesis from CO and CO2. *Angewandte Chemie International Edition*, 57(46):15045–15050, 2018. _eprint: https://onlinelibrary.wiley.com/doi/pdf/10.1002/anie.201806583.

[82] Feiyang Geng, Yolanda Bonita, Varsha Jain, Matthew Magiera, Neeraj Rai, and Jason C. Hicks. Bimetallic Ru–Mo Phosphide Catalysts for the Hydrogenation of CO2 to Methanol. *Industrial & Engineering Chemistry Research*, 59(15):6931–6943, April 2020. Publisher: American Chemical Society.

[83] Hiroya Ishikawa, Min Sheng, Ayako Nakata, Kiyotaka Nakajima, Seiji Yamazoe, Jun Yamasaki, Sho Yamaguchi, Tomoo Mizugaki, and Takato Mitsudome. Air-Stable and Reusable Cobalt Phosphide Nanoalloy Catalyst for Selective Hydrogenation of Furfural Derivatives. *ACS Catalysis*, 11(2):750–757, January 2021. Publisher: American Chemical Society.

[84] Min Sheng, Shu Fujita, Sho Yamaguchi, Jun Yamasaki, Kiyotaka Nakajima, Seiji Yamazoe, Tomoo Mizugaki, and Takato Mitsudome. Single-Crystal Cobalt Phosphide Nanorods as a High-Performance Catalyst for Reductive Amination of Carbonyl Compounds. *JACS Au*, 1(4):501–507, April 2021. Publisher: American Chemical Society.

[85] Takato Mitsudome, Min Sheng, Ayako Nakata, Jun Yamasaki, Tomoo Mizugaki, and Koichiro Jitsukawa. A cobalt phosphide catalyst for the hydrogenation of nitriles. *Chemical Science*, 11(26):6682–6689, July 2020. Publisher: The Royal Society of Chemistry.

[86] Ping Liu, José A. Rodriguez, Takeshi Asakura, João Gomes, and Kenichi Nakamura. Desulfurization Reactions on Ni2P(001) and -Mo2C(001) Surfaces: Complex Role of P and C Sites. *The Journal of Physical Chemistry B*, 109(10):4575–4583, March 2005. Publisher: American Chemical Society.

[87] Karin U. D. Calvinho, Anders B. Laursen, Kyra M. K. Yap, Timothy A. Goetjen, Shinjae Hwang, Nagarajan Murali, Bryan Mejia-Sosa, Alexander Lubarski, Krishani M. Teeluck, Eugene S. Hall, Eric Garfunkel, Martha Greenblatt, and G. Charles Dismukes. Selective CO2 reduction to C3 and C4 oxyhydrocarbons on nickel phosphides at overpotentials as low as 10 mV. *Energy & Environmental Science*, 11(9):2550–2559, September 2018. Publisher: The Royal Society of Chemistry.

[88] Lu Lu, Weiwei Guo, Chunjun Chen, Qinggong Zhu, Jun Ma, Haihong Wu, Dexin Yang, Guanying Yang, Xiaofu Sun, and Buxing Han. Synthesis of Sn 4 P 3 /reduced graphene oxide nanocomposites as highly efficient electrocatalysts for CO 2 reduction. *Green Chemistry*, 22(20):6804–6808, 2020. Publisher: Royal Society of Chemistry.

[89] Lei Ji, Lei Li, Xuqiang Ji, Ya Zhang, Shiyong Mou, Tongwei Wu, Qian Liu, Baihai Li, Xiaojuan Zhu, Yonglan Luo, Xifeng Shi, Abdullah M. Asiri, and Xuping Sun. Highly Selective Electrochemical Reduction of CO2 to Alcohols on an FeP Nanoarray. *Angewandte Chemie International Edition*, 59(2):758–762, 2020. _eprint: https://onlinelibrary.wiley.com/doi/pdf/10.1002/anie.201912836.

[90] Karin U. D. Calvinho, Abdulaziz W. Alherz, Kyra M. K. Yap, Anders B. Laursen, Shinjae Hwang, Zachary J. L. Bare, Zachary Clifford, Charles B. Musgrave, and G. Charles Dismukes. Surface Hydrides on Fe2P Electrocatalyst Reduce CO2 at Low Overpotential: Steering Selectivity to Ethylene Glycol. *Journal of the American Chemical Society*, 143(50):21275–21285, December 2021. Publisher: American Chemical Society.

[91] Shenghua Ye, Zhida Chen, Guikai Zhang, Wenda Chen, Chao Peng, Xiuyuan Yang, Lirong Zheng, Yongliang Li, Xiangzhong Ren, Huiqun Cao, Dongfeng Xue, Jieshan Qiu, Qianling Zhang, and Jianhong Liu. Elucidating the activity, mechanism and application of selective electrosynthesis of ammonia from nitrate on cobalt phosphide. *Energy & Environmental Science*, 15(2):760–770, 2022. Publisher: Royal Society of Chemistry.

[92] Qing-Ling Hong, Jia Zhou, Quan-Guo Zhai, Yu-Cheng Jiang, Man-Cheng Hu, Xue Xiao, Shu-Ni Li, and Yu Chen. Cobalt phosphide nanorings towards efficient electrocatalytic nitrate reduction to ammonia. *Chemical Communications*, 57(88):11621–11624, 2021. Publisher: Royal Society of Chemistry.

[93] Yang-Fan Xu, Paul N. Duchesne, Lu Wang, Alexandra Tavasoli, Abdinoor A. Jelle, Meikun Xia, Jin-Feng Liao, Dai-Bin Kuang, and Geoffrey A. Ozin. High-performance light-driven heterogeneous CO2 catalysis with near-unity selectivity on metal phosphides. *Nature Communications*, 11(1):5149, October 2020. Number: 1 Publisher: Nature Publishing Group.

[94] Xiandi Zhang, Jia Yan, Fangyuan Zheng, Jiong Zhao, and Lawrence Yoon Suk Lee. Designing charge transfer route at the interface between WP nanoparticle and g-C3N4 for highly enhanced photocatalytic CO2 reduction reaction. *Applied Catalysis B: Environmental*, 286:119879, June 2021.

[95] Jun-ying Tang, Dong Yang, Wei-guo Zhou, Rui-tang Guo, Wei-guo Pan, and Chun-ying Huang. Noble-metal-free molybdenum phosphide co-catalyst loaded graphitic carbon nitride for efficient photocatalysis under simulated irradiation. *Journal of Catalysis*, 370:79–87, February 2019.

[96] Diana C. Phillips, Stephanie J. Sawhill, Randy Self, and Mark E. Bussell. Synthesis, Characterization, and Hydrodesulfurization Properties of Silica-Supported Molybdenum Phosphide Catalysts. *Journal of Catalysis*, 207(2):266–273, April 2002.

[97] Utsab Guharoy, Tomas Ramirez Reina, Sai Gu, and Qiong Cai. Mechanistic Insights into Selective CO2 Conversion via RWGS on Transition Metal Phosphides: A DFT Study. *The Journal of Physical Chemistry C*, 123(37):22918–22931, September 2019. Publisher: American Chemical Society.

[98] Q. Zhang, L. Pastor-Pérez, J. J. Villora-Pico, M. Joyce, A. Sepúlveda-Escribano, M. S. Duyar, and T. R. Reina. Ni-Phosphide catalysts as versatile systems for gas-phase CO2 conversion: Impact of the support and evidences of structure-sensitivity. *Fuel*, 323:124301, September 2022.

[99] Sayan Banerjee, Arvin Kakekhani, Robert B. Wexler, and Andrew M. Rappe. Mechanistic Insights into CO2 Electroreduction on Ni2P: Understanding Its Selectivity toward Multicarbon Products. *ACS Catalysis*, 11(18):11706–11715, September 2021. Publisher: American Chemical Society.

[100] Debbie Baker, Trevor Brown, Nicholas Cook, Steve Cowley, Stephen Crolius, Chris Llewellyn Smith, Josh Makepeace, Cédric Philibert, Agustin Valera-Medina, Ian Wilkinson, and Tom Wood. Ammonia: zero-carbon fertiliser, fuel and energy storage. pages 1–40, 2020.

[101] Nicolas Gruber and James N. Galloway. An Earth-system perspective of the global nitrogen cycle. *Nature*, 451(7176):293–296, January 2008. Number: 7176 Publisher: Nature Publishing Group.

[102] Yachao Zeng, Cameron Priest, Guofeng Wang, and Gang Wu. Restoring the Nitrogen Cycle by Electrochemical Reduction of Nitrate: Progress and Prospects. *Small Methods*, 4(12):2000672, 2020. _eprint: https://onlinelibrary.wiley.com/doi/pdf/10.1002/smtd.202000672.

[103] Phebe H. van Langevelde, Ioannis Katsounaros, and Marc T. M. Koper. Electrocatalytic Nitrate Reduction for Sustainable Ammonia Production. *Joule*, 5(2):290–294, February 2021. Publisher: Elsevier.

[104] Hao Huang, Karthik Peramaiah, and Kuo-Wei Huang. Rethinking nitrate reduction: redirecting electrochemical efforts from ammonia to nitrogen for realistic environmental impacts. *Energy & Environmental Science*, 17(8):2682–2685, April 2024. Publisher: The Royal Society of Chemistry.

[105] Emily Nishiwaki, Peter S. Rice, Ding-Yuan Kuo, Florence Y. Dou, Anthony Pyka, Bryce Reid, Hao A. Nguyen, Eric M. Stuve, Simone Raugei, and Brandi M. Cossairt. Ni 2 P active site ensembles tune electrocatalytic nitrate reduction selectivity. *Chemical Communications*, 60(54):6941–6944, 2024. Publisher: Royal Society of Chemistry.

[106] Boyang Liu, Xiaocheng Lan, Qin Zhong, and Tiefeng Wang. Metal Phosphide: An Atypical Catalytic Site. *ACS Catalysis*, 14(2):757–775, January 2024. Publisher: American Chemical Society.

[107] Bora Seo, Du San Baek, Young Jin Sa, and Sang Hoon Joo. Shape effects of nickel phosphide nanocrystals on hydrogen evolution reaction. *CrystEngComm*, 18(32):6083–6089, 2016. Publisher: Royal Society of Chemistry.

[108] Courtney A. Downes, Kurt M. Van Allsburg, Sean A. Tacey, Kinga A. Unocic, Frederick G. Baddour, Daniel A. Ruddy, Nicole J. LiBretto, Max M. O'Connor, Carrie A. Farberow, Joshua A. Schaidle, and Susan E. Habas. Controlled Synthesis of Transition Metal Phosphide Nanoparticles to Establish Composition-Dependent Trends in Electrocatalytic Activity. *Chemistry of Materials*, 34(14):6255–6267, July 2022. Publisher: American Chemical Society.

[109] Melis S. Duyar, Alessandro Gallo, Samuel K. Regli, Jonathan L. Snider, Joseph A. Singh, Eduardo Valle, Joshua McEnaney, Stacey F. Bent, Magnus Rønning, and Thomas F. Jaramillo. Understanding Selectivity in CO2 Hydrogenation to Methanol for MoP Nanoparticle Catalysts Using In Situ Techniques. *Catalysts*, 11(1):143, January 2021. Number: 1 Publisher: Multidisciplinary Digital Publishing Institute.

[110] Courtney A. Downes, Nicole J. Libretto, Anne E. Harman-Ware, Renee M. Happs, Daniel A. Ruddy, Frederick G. Baddour, Jack R. Ferrell III, Susan E. Habas, and Joshua A. Schaidle. Electrocatalytic CO2 Reduction over Cu3P Nanoparticles Generated via a Molecular Precursor Route. *ACS Applied Energy Materials*, 3(11):10435–10446, November 2020. Publisher: American Chemical Society.

[111] Jie Li, Guangming Zhan, Jianhua Yang, Fengjiao Quan, Chengliang Mao, Yang Liu, Bo Wang, Fengcai Lei, Lejing Li, Alice W. M. Chan, Liangpang Xu, Yanbiao Shi, Yi Du, Weichang Hao, Po Keung Wong, Jianfang Wang, Shi-Xue Dou, Lizhi Zhang, and Jimmy C. Yu. Efficient Ammonia Electrosynthesis from Nitrate on Strained Ruthenium Nanoclusters. *Journal of the American Chemical Society*, 142(15):7036–7046, April 2020. Publisher: American Chemical Society.

[112] Ting Chen, Hongjiao Li, Houyi Ma, and Marc T. M. Koper. Surface Modification of Pt(100) for Electrocatalytic Nitrate Reduction to Dinitrogen in Alkaline Solution. *Langmuir*, 31(10):3277–3281, March 2015. Publisher: American Chemical Society.

[113] Kai Chen, Jiaqi Xiang, Yali Guo, Xijun Liu, Xingang Li, and Ke Chu. Pd1Cu Single-Atom Alloys for High-Current-Density and Durable NO-to-NH3 Electroreduction. *Nano Letters*, 24(2):541–548, January 2024. Publisher: American Chemical Society.

[114] Qikun Hu, Ke Yang, Ouwen Peng, Minzhang Li, Lu Ma, Songpeng Huang, Yonghua Du, Zong-Xiang Xu, Qing Wang, Zhongxin Chen, Ming Yang, and Kian Ping Loh. Ammonia Electrosynthesis from Nitrate Using a Ruthenium–Copper Cocatalyst System: A Full Concentration Range Study. *Journal of the American Chemical Society*, 146(1):668–676, January 2024. Publisher: American Chemical Society.

[115] Jia-Qi Chen, Xu-Xu Ye, Da Zhou, and Yan-Xia Chen. Roles of Copper in Nitrate Reduction at Copper-Modified Ru/C Catalysts. *The Journal of Physical Chemistry C*, 127(6):2918–2928, February 2023. Publisher: American Chemical Society.

[116] Haibo Yin, Feng Dong, Haiwei Su, Zechao Zhuang, Yunlong Wang, Dingsheng Wang, Yue Peng, and Junhua Li. Unraveling the Activity Trends and Design Principles of Single-Atom Catalysts for Nitrate Electrocatalytic Reduction. *ACS Nano*, 17(24):25614–25624, December 2023. Publisher: American Chemical Society.

[117] Haibo Yin, Feng Dong, Yunlong Wang, Haiwei Su, Xiansheng Li, Yue Peng, Haohong Duan, and Junhua Li. Understanding the Activity Trends in Electrocatalytic Nitrate Reduction to Ammonia on Cu Catalysts. *Nano Letters*, 23(24):11899–11906, December 2023. Publisher: American Chemical Society.

[118] Eamonn Murphy, Yuanchao Liu, Ivana Matanovic, Martina Rüscher, Ying Huang, Alvin Ly, Shengyuan Guo, Wenjie Zang, Xingxu Yan, Andrea Martini, Janis Timoshenko, Beatriz Roldán Cuenya, Iryna V. Zenyuk, Xiaoqing Pan, Erik D. Spoerke, and Plamen Atanassov. Elucidating electrochemical nitrate and nitrite reduction over atomically-dispersed transition metal sites. *Nature Communications*, 14(1):4554, July 2023. Number: 1 Publisher: Nature Publishing Group.

[119] Jin-Xun Liu, Danielle Richards, Nirala Singh, and Bryan R. Goldsmith. Activity and Selectivity Trends in Electrocatalytic Nitrate Reduction on Transition Metals. *ACS Catalysis*, 9(8):7052–7064, August 2019. Publisher: American Chemical Society.

[120] Tao Hu, Changhong Wang, Mengting Wang, Chang Ming Li, and Chunxian Guo. Theoretical Insights into Superior Nitrate Reduction to Ammonia Performance of Copper Catalysts. *ACS Catalysis*, 11(23):14417–14427, December 2021. Publisher: American Chemical Society.

[121] Xingmei Lu, Haoqiang Song, Jinmeng Cai, and Siyu Lu. Recent development of electrochemical nitrate reduction to ammonia: A mini review. *Electrochemistry Communications*, 129:107094, August 2021.

[122] Jiaqi Ni, Jing Yan, Fuhua Li, Haifeng Qi, Qingzhu Xu, Chenliang Su, Like Sun, Hongli Sun, Jie Ding, and Bin Liu. Atomic CoP Catalytic Pair Drives Efficient Electrochemical Nitrate Reduction to Ammonia. *Advanced Energy Materials*, n/a(n/a):2400065, March 2024. _eprint: https://onlinelibrary.wiley.com/doi/pdf/10.1002/aenm.202400065.

[123] Qian Liu, Yiting Lin, Shuang Gu, Ziqiang Cheng, Lisi Xie, Shengjun Sun, Longcheng Zhang, Yongsong Luo, Abdulmohsen Ali Alshehri, Mohamed S. Hamdy, Qingquan Kong, Jiahong Wang, and Xuping Sun. Enhanced N2-to-NH3 conversion efficiency on Cu3P nanoribbon electrocatalyst. *Nano Research*, 15(8):7134–7138, August 2022.

[124] Guohui Wang, Ying Zhang, Kai Chen, Yali Guo, and Ke Chu. PdP2 Nanoparticles on Reduced Graphene Oxide: A Catalyst for the Electrocatalytic Reduction of Nitrate to Ammonia. *Inorganic Chemistry*, April 2023. Publisher: American Chemical Society.

[125] Qiufang Yao, Jiabin Chen, Shaoze Xiao, Yalei Zhang, and Xuefei Zhou. Selective Electrocatalytic Reduction of Nitrate to Ammonia with Nickel Phosphide. *ACS Applied Materials & Interfaces*, 13(26):30458–30467, July 2021. Publisher: American Chemical Society.

[126] Yi Jia, Yi-Gang Ji, Qi Xue, Fu-Min Li, Guang-Tao Zhao, Pu-Jun Jin, Shu-Ni Li, and Yu Chen. Efficient Nitrate-to-Ammonia Electroreduction at Cobalt Phosphide Nanoshuttles. *ACS Applied Materials & Interfaces*, 13(38):45521–45527, September 2021. Publisher: American Chemical Society.

[127] Rong Zhang, Ying Guo, Shaoce Zhang, Dong Chen, Yuwei Zhao, Zhaodong Huang, Longtao Ma, Pei Li, Qi Yang, Guojin Liang, and Chunyi Zhi. Efficient Ammonia Electrosynthesis and Energy Conversion through a Zn-Nitrate Battery by Iron Doping Engineered Nickel Phosphide Catalyst. *Advanced Energy Materials*, 12(13):2103872, 2022. _eprint: https://onlinelibrary.wiley.com/doi/pdf/10.1002/aenm.202103872.

[128] Siyue Huo, Shuqin Yang, Qianqian Niu, Zimo Song, Fan Yang, and Laizhou Song. Fabrication of Porous Configurated Ni2P/Ni Foam Catalyst and its Boosted Properties for pH-universal Hydrogen Evolution Reaction and Efficient Nitrate Reduction. *ChemCatChem*, 12(18):4600–4610, 2020. _eprint: https://onlinelibrary.wiley.com/doi/pdf/10.1002/cctc.202000426.

[129] Lulu Wen, Yiqiang Sun, Chao Zhang, Jie Yu, Xinyang Li, Xianjun Lyu, Weiping Cai, and Yue Li. Cu-Doped CoP Nanorod Arrays: Efficient and Durable Hydrogen Evolution Reaction Electrocatalysts at All pH Values. *ACS Applied Energy Materials*, 1(8):3835–3842, August 2018. Publisher: American Chemical Society.

[130] Frederick G. Baddour, Emily J. Roberts, Anh T. To, Lu Wang, Susan E. Habas, Daniel A. Ruddy, Nicholas M. Bedford, Joshua Wright, Connor P. Nash, Joshua A. Schaidle, Richard L. Brutchey, and Noah Malmstadt. An Exceptionally Mild and Scalable Solution-Phase Synthesis of Molybdenum Carbide Nanoparticles for Thermocatalytic CO2 Hydrogenation. *Journal of the American Chemical Society*, 142(2):1010–1019, January 2020. Publisher: American Chemical Society.

[131] O. Quinn Carvalho, Rylee Marks, Hoan K. K. Nguyen, Molly E. Vitale-Sullivan, Selena C. Martinez, Líney Árnadóttir, and Kelsey A. Stoerzinger. Role of Electronic Structure on Nitrate Reduction to Ammonium: A Periodic Journey. *Journal of the American Chemical Society*, 144(32):14809–14818, August 2022. Publisher: American Chemical Society.

[132] Ali Hussain Motagamwala and James A. Dumesic. Microkinetic Modeling: A Tool for Rational Catalyst Design. *Chemical Reviews*, 121(2):1049–1076, January 2021. Publisher: American Chemical Society.

[133] Nirala Singh, Udishnu Sanyal, Griffin Ruehl, Kelsey A. Stoerzinger, Oliver Y. Gutiérrez, Donald M. Camaioni, John L. Fulton, Johannes A. Lercher, and Charles T. Campbell. Aqueous phase catalytic and electrocatalytic hydrogenation of phenol and benzaldehyde over platinum group metals. *Journal of Catalysis*, 382:372–384, February 2020.

[134] Zixuan Wang, Danielle Richards, and Nirala Singh. Recent discoveries in the reaction mechanism of heterogeneous electrocatalytic nitrate reduction. *Catalysis Science & Technology*, 11(3):705–725, 2021. Publisher: Royal Society of Chemistry.

[135] Yue Cao, Shengbo Yuan, Linghu Meng, Yingying Wang, Yan Hai, Senda Su, Wenming Ding, Zhenyu Liu, Xiaoman Li, and Min Luo. Recent Advances in Electrocatalytic Nitrate Reduction to Ammonia: Mechanism Insight and Catalyst Design. *ACS Sustainable Chemistry & Engineering*, 11(21):7965–7985, May 2023. Publisher: American Chemical Society.

[136] Kaiwen Yang, Shu-He Han, Chuanqi Cheng, Chengying Guo, Tieliang Li, and Yifu Yu. Unveiling the Reaction Mechanism of Nitrate Reduction to Ammonia Over Cobalt-Based Electrocatalysts. *Journal of the American Chemical Society*, April 2024. Publisher: American Chemical Society.

[137] Yuecheng Xiong, Yunhao Wang, Jingwen Zhou, Fu Liu, Fengkun Hao, and Zhanxi Fan. Electrochemical Nitrate Reduction: Ammonia Synthesis and the Beyond. *Advanced Materials*, n/a(n/a):2304021, June 2023. _eprint: https://onlinelibrary.wiley.com/doi/pdf/10.1002/adma.202304021.

[138] Haiyang Yuan, Ningning Sun, Jianfu Chen, Jiamin Jin, Haifeng Wang, and Peijun Hu. Insight into the NH3-Assisted Selective Catalytic Reduction of NO on -MnO2(110): Reaction Mechanism, Activity Descriptor, and Evolution from a Pristine State to a Steady State. *ACS Catalysis*, 8(10):9269–9279, October 2018. Publisher: American Chemical Society.

[139] Peter S. Rice, Zhi-Pan Liu, and P. Hu. Hydrogen Coupling on Platinum Using Artificial Neural Network Potentials and DFT. *The Journal of Physical Chemistry Letters*, 12(43):10637–10645, November 2021. Publisher: American Chemical Society.

[140] Peter S. Rice, Yu Mao, Chenxi Guo, and P. Hu. Interconversion of hydrated protons at the interface between liquid water and platinum. *Physical Chemistry Chemical Physics*, 21(11):5932–5940, March 2019. Publisher: The Royal Society of Chemistry.

[141] Önder Metin, Vismadeb Mazumder, Saim Özkar, and Shouheng Sun. Monodisperse Nickel Nanoparticles and Their Catalysis in Hydrolytic Dehydrogenation of Ammonia Borane. *Journal of the American Chemical Society*, 132(5):1468–1469, February 2010. Publisher: American Chemical Society.

[142] Liane M. Moreau, Don-Hyung Ha, Clive R. Bealing, Haitao Zhang, Richard G. Hennig, and Richard D. Robinson. Unintended Phosphorus Doping of Nickel Nanoparticles during Synthesis with TOP: A Discovery through Structural Analysis. *Nano Letters*, 12(9):4530–4539, September 2012. Publisher: American Chemical Society.

[143] Sophie Carenco, Cédric Boissière, Lionel Nicole, Clément Sanchez, Pascal Le Floch, and Nicolas Mézailles. Controlled Design of Size-Tunable Monodisperse Nickel Nanoparticles. *Chemistry of Materials*, 22(4):1340–1349, February 2010. Publisher: American Chemical Society.

[144] Navpreet Kamboj and Ramendra Sundar Dey. Electrochemically grown highly crystalline single-phase Ni3P superstructure accelerating ionic diffusion in rechargeable Ni–Zn battery. *Journal of Power Sources*, 512:230527, November 2021.

[145] Min Li, Yunyun Luo, Chen Jia, Qiankun Zhang, Guoxi Luo, Libo Zhao, Rabah Boukherroub, and Zhuangde Jiang. Facile Synthesis of Bimetal Nickel Cobalt Phosphate Nanostructures for High-Performance Hybrid Supercapacitors. *Journal of Alloys and Compounds*, 893:162340, February 2022.

[146] Yuhang Wang, Aoni Xu, Ziyun Wang, Linsong Huang, Jun Li, Fengwang Li, Joshua Wicks, Mingchuan Luo, Dae-Hyun Nam, Chih-Shan Tan, Yu Ding, Jiawen Wu, Yanwei Lum, Cao-Thang Dinh, David Sinton, Gengfeng Zheng, and Edward H. Sargent. Enhanced Nitrate-to-Ammonia Activity on Copper–Nickel Alloys via Tuning of Intermediate Adsorption. *Journal of the American Chemical Society*, 142(12):5702–5708, March 2020. Publisher: American Chemical Society.

[147] Yong Zhu, Jianfang Chen, Dongxing Yuan, Zhi Yang, Xiaolai Shi, Hongliang Li, Haiyan Jin, and Lihua Ran. Development of analytical methods for ammonium determination in seawater over the last two decades. *TrAC Trends in Analytical Chemistry*, 119:115627, October 2019.

[148] Daniela Giustarini, Ranieri Rossi, Aldo Milzani, and Isabella Dalle-Donne. Nitrite and Nitrate Measurement by Griess Reagent in Human Plasma: Evaluation of Interferences and Standardization. In *Methods in Enzymology*, volume 440 of *Nitric Oxide, Part F*, pages 361–380. Academic Press, January 2008.

[149] Taehyun Kwon, Taekyung Kim, Yunchang Son, and Kwangyeol Lee. Dopants in the Design of Noble Metal Nanoparticle Electrocatalysts and their Effect on Surface Energy and Coordination Chemistry at the Nanocrystal Surface. *Advanced Energy Materials*, 11(22):2100265, 2021. _eprint: https://advanced.onlinelibrary.wiley.com/doi/pdf/10.1002/aenm.202100265.

[150] Samuel I. Mutinda, Tharanga N. Batugedara, Benjamin Brown, Olugbenga Adeniran, Zhen-Fei Liu, and Stephanie L. Brock. Rh2P Activity at a Fraction of the Cost? Co2–xRhxP Nanoparticles as Electrocatalysts for the Hydrogen Evolution Reaction in Acidic Media. *ACS Applied Energy Materials*, 4(1):946–955, January 2021. Publisher: American Chemical Society.

[151] Samuel I. Mutinda, Da Li, Jacob Kay, and Stephanie L. Brock. Synthesis and characterization of Co2xRhxP nanoparticles and their catalytic activity towards the oxygen evolution reaction. *Journal of Materials Chemistry A*, 6(25):12142–12152, June 2018. Publisher: The Royal Society of Chemistry.

[152] Fatemeh Aghabozorgi, S. Sameera Perera, and Stephanie L. Brock. Ni2–xMnxP Nanoparticles as Earth-Abundant Precatalysts for Electrochemical Water Oxidation. *Chemistry of Materials*, 36(5):2461–2472, March 2024. Publisher: American Chemical Society.

[153] Qing-Ling Hong, Ze-Nong Zhang, Xiao-Hui Wang, Shi-Bin Yin, Feng Shi, Shu-Ni Li, and Yu Chen. Iron-Doped Cobalt Phosphide Nanohoops for Electroreduction of Nitrate to Ammonia. *Inorganic Chemistry*, 61(36):14397–14402, September 2022. Publisher: American Chemical Society.

[154] Shahid Khan, Sajid Mahmood, Mahmood ul Haq, Amjad Ali, Sufaid Shah, Ghulam Abbas Ashraf, and Qinqin Liu. Fe–CuP nanocubes for nitrate-to-ammonia conversion. *New Journal of Chemistry*, 48(15):6933–6942, 2024. Publisher: Royal Society of Chemistry.

[155] B. Hammer and J.K. Nørskov. Theoretical surface science and catalysis—calculations and concepts. In *Advances in Catalysis*, volume 45, pages 71–129. Elsevier, 2000.

[156] Ichigaku Takigawa, Ken-ichi Shimizu, Koji Tsuda, and Satoru Takakusagi. Machine-learning prediction of the d-band center for metals and bimetals. *RSC Advances*, 6(58):52587–52595, May 2016. Publisher: The Royal Society of Chemistry.

[157] Satadeep Bhattacharjee, Umesh V. Waghmare, and Seung-Cheol Lee. An improved d-band model of the catalytic activity of magnetic transition metal surfaces. *Scientific Reports*, 6(1):35916, November 2016. Publisher: Nature Publishing Group.

[158] Shilong Jiao, Xianwei Fu, and Hongwen Huang. Descriptors for the Evaluation of Electrocatalytic Reactions: d-Band Theory and Beyond. *Advanced Functional Materials*, 32(4):2107651, 2022. _eprint: https://advanced.onlinelibrary.wiley.com/doi/pdf/10.1002/adfm.202107651.

[159] Eishiro Toyoda, Ryosuke Jinnouchi, Tatsuya Hatanaka, Yu Morimoto, Kei Mitsuhara, Anton Visikovskiy, and Yoshiaki Kido. The d-Band Structure of Pt Nanoclusters Correlated with the Catalytic Activity for an Oxygen Reduction Reaction. *The Journal of Physical Chemistry C*, 115(43):21236–21240, November 2011. Publisher: American Chemical Society.

[160] Basil Raju Karimadom, Alina Sermiagin, Dan Meyerstein, Tomer Zidki, Amir Mizrahi, Ronen Bar-Ziv, and Haya Kornweitz. Hydrogen adsorption on various transition metal (111) surfaces in water: a DFT forecast. *Physical Chemistry Chemical Physics*, 26(9):7647–7657, 2024. Publisher: Royal Society of Chemistry.

[161] Tao Ling, Mietek Jaroniec, and Shi-Zhang Qiao. Recent Progress in Engineering the Atomic and Electronic Structure of Electrocatalysts via Cation Exchange Reactions. *Advanced Materials*, 32(46):2001866, 2020. _eprint: https://advanced.onlinelibrary.wiley.com/doi/pdf/10.1002/adma.202001866.

[162] Luca De Trizio and Liberato Manna. Forging Colloidal Nanostructures via Cation Exchange Reactions. *Chemical Reviews*, 116(18):10852–10887, September 2016. Publisher: American Chemical Society.

[163] Dong Hee Son, Steven M. Hughes, Yadong Yin, and A. Paul Alivisatos. Cation Exchange Reactions in Ionic Nanocrystals. *Science*, 306(5698):1009–1012, November 2004. Publisher: American Association for the Advancement of Science.

[164] Brandon J. Beberwyck and A. Paul Alivisatos. Ion Exchange Synthesis of III–V Nanocrystals. *Journal of the American Chemical Society*, 134(49):19977–19980, December 2012. Publisher: American Chemical Society.

[165] Karol Miszta, Graziella Gariano, Rosaria Brescia, Sergio Marras, Francesco De Donato, Sandeep Ghosh, Luca De Trizio, and Liberato Manna. Selective Cation Exchange in the Core Region of Cu2–xSe/Cu2–xS Core/Shell Nanocrystals. *Journal of the American Chemical Society*, 137(38):12195–12198, September 2015. Publisher: American Chemical Society.

[166] Luca De Trizio, Roberto Gaspari, Giovanni Bertoni, Ilka Kriegel, Luca Moretti, Francesco Scotognella, Lorenzo Maserati, Yang Zhang, Gabriele C. Messina, Mirko Prato, Sergio Marras, Andrea Cavalli, and Liberato Manna. Cu3-xP Nanocrystals as a Material Platform for Near-Infrared Plasmonics and Cation Exchange Reactions. *Chemistry of Materials*, 27(3):1120–1128, February 2015. Publisher: American Chemical Society.

[167] Tepora Su'a, Mikaylah N. Poli, and Stephanie L. Brock. Homogeneous Nanoparticles of Multimetallic Phosphides via Precursor Tuning: Ternary and Quaternary M2P Phases (M

= Fe, Co, Ni). *ACS Nanoscience Au*, 2(6):503–519, December 2022. Publisher: American Chemical Society.

[168] Susan E. Habas, Frederick G. Baddour, Daniel A. Ruddy, Connor P. Nash, Jun Wang, Ming Pan, Jesse E. Hensley, and Joshua A. Schaidle. A Facile Molecular Precursor Route to Metal Phosphide Nanoparticles and Their Evaluation as Hydrodeoxygenation Catalysts. *Chemistry of Materials*, 27(22):7580–7592, November 2015. Publisher: American Chemical Society.

[169] D. Ruchira Liyanage, Da Li, Quintin B. Cheek, Habib Baydoun, and Stephanie L. Brock. Synthesis and oxygen evolution reaction (OER) catalytic performance of Ni2xRuxP nanocrystals: enhancing activity by dilution of the noble metal. *Journal of Materials Chemistry A*, 5(33):17609–17618, August 2017. Publisher: The Royal Society of Chemistry.

[170] Mark C. Biesinger, Leo W. M. Lau, Andrea R. Gerson, and Roger St. C. Smart. Resolving surface chemical states in XPS analysis of first row transition metals, oxides and hydroxides: Sc, Ti, V, Cu and Zn. *Applied Surface Science*, 257(3):887–898, November 2010.

[171] J. C Dupin, D Gonbeau, H Benqlilou-Moudden, Ph Vinatier, and A Levasseur. XPS analysis of new lithium cobalt oxide thin-films before and after lithium deintercalation. *Thin Solid Films*, 384(1):23–32, March 2001.

[172] Kui Fan, Wenfu Xie, Jinze Li, Yining Sun, Pengcheng Xu, Yang Tang, Zhenhua Li, and Mingfei Shao. Active hydrogen boosts electrochemical nitrate reduction to ammonia. *Nature Communications*, 13(1):7958, December 2022. Publisher: Nature Publishing Group.

[173] Jialei Du, Jianying Wang, Lvlv Ji, Xiaoxiang Xu, and Zuofeng Chen. A Highly Active and Robust Copper-Based Electrocatalyst toward Hydrogen Evolution Reaction with Low Overpotential in Neutral Solution. *ACS Applied Materials & Interfaces*, 8(44):30205–30211, November 2016. Publisher: American Chemical Society.